



Universidade Federal  
de Campina Grande



*Modelagem geológica e petrofísica da zona de dano da Falha Malta na  
Bacia Rio do Peixe, NE do Brasil*

*Autora:*

*Maria Eduarda da Silva*

*Orientador:*

*Francisco César Costa Nogueira*

*Segundo-orientador:*

*Yoe Alain Reyes Perez*

*Campina Grande – Paraíba*

*Abril de 2022*

*Maria Eduarda da Silva*

*Modelagem geológica e petrofísica da zona de dano da Falha Malta na  
Bacia Rio do Peixe, NE do Brasil.*

Dissertação de Mestrado apresentada em  
22/04/2022 à Universidade Federal de  
Campina Grande como requisito do  
Programa de Pós-graduação Exploração  
Petrolífera e Mineral para obtenção do grau  
de Mestre em Exploração Petrolífera e  
Mineral.

*Orientador:*

*Francisco César Costa Nogueira*

*Segundo-orientador:*

*Yoe Alain Reyes Perez*

*Campina Grande – Paraíba*

*Abril de 2022*

S586m Silva, Maria Eduarda da.  
Modelagem geológica e petrofísica da zona de dano da Falha Malta na  
Bacia Rio do Peixe, NE do Brasil / Maria Eduarda da Silva. – Campina  
Grande, 2022.  
122 f. : il. color.

Dissertação (Mestrado em Exploração Petrolífera e Mineral) –  
Universidade Federal de Campina Grande, Centro de Tecnologia e  
Recursos Naturais, 2022.

"Orientação: Prof. Dr. Francisco César Costa Nogueira; Coorientação:  
Prof. Dr. Yoe Alain Reyes Péres".

Referências.

1. Bacia Rio do Peixe. 2. Falhas de Borda Rifte. 3. Zonas de Falha.  
4. Zonas de Dano. 5. Bandas de Deformação. 6. Fácies de Falha.  
7. Modelagem Geológica 3D. 8. Reservatórios Siliciclásticos. 9. Petrel.  
I. Nogueira, Francisco César Costa. II. Péres, Yoe Alain Reyes. III.  
Título.

CDU 556.51(812/813)(043)



MINISTÉRIO DA EDUCAÇÃO

**UNIVERSIDADE FEDERAL DE CAMPINA GRANDE**

POS-GRADUACAO EXP. PETROLIFERA E MINERACAO

Rua Aprigio Veloso, 882, - Bairro Universitario, Campina Grande/PB, CEP 58429-900

## **FOLHA DE ASSINATURA PARA TESES E DISSERTAÇÕES**

**Maria Eduarda da Silva**

**MODELAGEM GEOLÓGICA E  
PETROFÍSICA DE ZONAS DE  
DANO DA FALHA MALTA NA  
BACIA RIO DO PEIXE, NE DO  
BRASIL**

Dissertação apresentada ao Programa de Pós-Graduação em exploração petrolífera e mineral - PPGEPM-UFCG como pré-requisito para obtenção do título de Mestre em exploração petrolífera e mineral.

Aprovada em: 22/04/2022

Prof. Dr. Francisco César Costa Nogueira - Orientador - UFCG

Prof. Dr. David Lino Vasconcelos - Examinador Interno - UFCG

Prof. Dr. Tiago Siqueira de Miranda - Examinador Externo - UFPE



Documento assinado eletronicamente por **David Lino Vasconcelos, Usuário Externo**, em 25/04/2022, às 12:26, conforme horário oficial de Brasília, com fundamento no art. 8º, caput, da [Portaria SEI nº 002, de 25 de outubro de 2018](#).

---



Documento assinado eletronicamente por **FRANCISCO CEZAR COSTA NOGUEIRA, PROFESSOR**, em 12/05/2022, às 16:45, conforme horário oficial de Brasília, com fundamento no art. 8º, caput, da [Portaria SEI nº 002, de 25 de outubro de 2018](#).

---



Documento assinado eletronicamente por **Tiago Siqueira de Miranda, Usuário Externo**, em 07/06/2022, às 11:07, conforme horário oficial de Brasília, com fundamento no art. 8º, caput, da [Portaria SEI nº 002, de 25 de outubro de 2018](#).

---



A autenticidade deste documento pode ser conferida no site <https://sei.ufcg.edu.br/autenticidade>, informando o código verificador **2318788** e o código CRC **086DD5E3**.

---

*“Se eu vi mais longe, foi por estar sobre ombros de gigantes.”*

**Isaac Newton**

A minha mãe Claudia e ao meu Pai Bruno (*in memoriam*) e a todos aqueles que contribuíram para minha educação.

## **Agradecimentos**

Meus sinceros agradecimentos a Deus da mesma forma que faço em todas as manhãs e noites: “Obrigada Deus por mais um dia e que eu tenha todos que o senhor me permitir”.

Aos meus pais, Claudia Adriana Silva e Bruno Henrique da Silva (*In memoriam*) agradeço por serem meus melhores amigos, nunca medirem esforços para a realização do melhor para mim, por toda minha educação, enfim... todas as palavras são incapazes de expressar meu amor por vocês e admiração por ser quem são ou foram! Te amo Mãe! Te amo pai!

Claro que a pessoa que tornou o meu sonho de ter uma/um irmã/irmão o pesadelo mais legal da vida teria um parágrafo só para ela! Anna Beatriz, te amo! Obrigada por sempre nos fazer sorrir mesmo quando os dias foram os mais difíceis! Bia, sem dúvidas você é um presente!

Aos meus familiares e amigos do melhor e maior São João do mundo (Caruaru) e do segundo maior também (Campina Grande), obrigada!

Aos meus orientadores, Francisco César e Yoe Alain, obrigada por toda a confiança durante os dias de trabalho, por todos os conhecimentos compartilhados e por todas as oportunidades proporcionadas. Apesar de não estar no papel David Vasconcelos você também foi meu orientador e estendo a você todos os agradecimentos acima!

Aos colegas, Rômulo Stohler, Júlio Sanglard, Jorge André, Bruno Carvalho e aos Profs. Francisco Hilário e Fabrizio Balsamo agradeço por todos os conhecimentos compartilhados e por sempre estarem dispostos a me ajudar!

Obrigada aos membros do LAPEP por compartilharmos tantas vivências, conhecimentos, amizade, companheirismo e pelos muitos copos de café! Vocês reforçam todos os dias que nós somos melhor juntos!

Por fim, agradeço ao convênio Petrobras/UFCG TC 5850.0109438.18.9, coordenado pelo Prof. Francisco César Costa Nogueira, pelo financiamento das atividades desenvolvidas nesta dissertação, assim como concessão de bolsa de estudos e a empresa Schlumberger pelo fornecimento de licenças do software Petrel®.



## Resumo

As espessuras das zonas de dano e o contraste de permeabilidade entre bandas de deformação e os espaços interbanda (rocha hospedeira) presente nessas zonas impactam o fluxo de fluido em arenitos porosos afetados por zonas de falhas. Neste estudo, nós modelamos a extensão das zonas de dano no *hangingwall* de uma falha de borda da BRP (Falha Malta) e a distribuição da intensidade de bandas de deformação, usando modelagem de fácies de falha. Nós usamos dados de frequência acumulada de bandas de deformação para delimitar e modelar os limites dos subdomínios da zona de dano e a frequência para caracterizar as fácies de falha. Em seguida, nós integramos os dados de permeabilidade, coletados nas bandas de deformação e espaços interbanda (rocha hospedeira), para modelar essas propriedades de acordo com as zonas de dano e fácies de falha. Nossos resultados permitiram caracterizar o controle da deformação na distribuição da permeabilidade de arenitos porosos afetados por falhas. A intensidade de deformação (BD/m) mostrou-se importante para a análise de permeabilidade. Para os subdomínios das zonas de dano mais deformados ou com predomínio de fácies de falha com altas intensidades de bandas de deformação, as bandas de deformação e espaços interbanda mostram reduções de permeabilidade semelhantes de até 3 ordens de magnitude comparadas as rochas não deformadas, onde ocorrem fácies de baixa deformação ou sem deformação. Este estudo realizado na Falha de Malta fornece novas perspectivas sobre a permeabilidade das bandas de deformação e espaços interbanda em diferentes subdomínios das zonas de dano e fácies de falha. Assim, essa pesquisa viabiliza a modelagem de permeabilidades equivalentes ao longo de zonas de dano, que tem implicações para reservatórios siliciclásticos afetados por zonas de falha, onde bandas de deformação são as estruturas rúpteis dominantes.

**Palavras-Chaves:** *Bacia Rio do Peixe; Falhas de Borda Rifte; Zonas de Falha; Zonas de Dano; Bandas de Deformação; Fácies de Falha; Modelagem Geológica 3D; Reservatórios Siliciclásticos; Petrel.*

### Abstract

The damage zone width and the permeability contrast between deformation bands and the interband spaces (host rock) impact the fluid flow in porous sandstones affected by fault zones. In this study, we model the damage zone extension in the hangingwall of a BRP (Malta Fault) bounding–fault and the distribution of deformation band intensity (DB/m), using fault facies modeling. We use from deformation band cumulative frequency data to delimit and model the damage zone subdomain boundaries and the frequency to characterize fault facies. Then, we integrated the permeability data, collected in the deformation bands and interband spaces (host rock), to model these properties conditioned to the damage zones and fault facies. Our results allowed us to characterize the deformation control in the permeability distribution of porous sandstones affected by faults. The deformation intensity (DB/m) proved to be important for the permeability analysis. For the subdomains of the most deformed damage zones or with a predominance of fault facies with high deformation band intensity, deformation bands and interband spaces show similar permeability reductions of up to 3 orders of magnitude compared to undeformed rocks, which occur low deformation or no deformation facies. This study carried out on the Malta Fault provides new insights into the deformation band permeability and interband spaces in different damage zone subdomains and fault facies. Thus, this research enables the modeling of equivalent permeabilities along damage zones, which has implications for siliciclastic reservoirs affected by fault zones, where deformation bands are the dominant brittle structures.

**Keywords:** *Rio do Peixe Basin; rift bounding-fault; Fault zones; Damage zones; Deformation bands Fault Facies; 3D Geological modeling; Siliciclastic reservoirs; Petrel.*

**Sumário****Sumário**

Agradecimentos .....	iii
Resumo .....	iv
Abstract.....	v
Sumário.....	vi
Lista de Figuras .....	viii
Lista de Tabelas .....	xv
<i>Capítulo. 1</i> .....	1
1. Introdução.....	2
1.1. Apresentação .....	2
1.2. Justificativa e Objetivos .....	3
1.3. Localização da Área de Estudo .....	5
<i>Capítulo. 2</i> .....	11
2. Contexto Geológico.....	12
2.1 Bacia Rio do Peixe .....	12
2.2. Zonas de Falha da Bacia Rio do Peixe .....	14
<i>Capítulo. 3</i> .....	20
3. Fundamentação Teórica.....	21
3.1. Zonas de Falha.....	21
3.1.1. Arquitetura, Elementos e Componentes das Zonas de Falha .....	21
3.2. Zonas de Falha em Arenitos Porosos .....	28
3.2.1. Bandas de Deformação.....	28
3.2.2. Propriedades Petrofísicas das Bandas de Deformação, Espaços Interbanda e Núcleo de falhas.....	31
3.3. Modelagem Geológica de Zonas de Falha .....	34
3.3.1. Modelagem de Fácies de Falha .....	37
<i>Capítulo. 4</i> .....	40
Abstract.....	41
Keywords:.....	42
1. Introduction .....	42
2. Geological Setting .....	47
3. Methods .....	50
PPGEPM – UFCG .....	vi

---

3.1. <i>Measurements of deformation features</i> .....	50
3.3. <i>Fault facies analysis and modeling</i> .....	54
3.4. <i>Permeability modeling</i> .....	56
4. Results .....	60
4.1. <i>Main fault and its damage zone</i> .....	60
4.3. <i>Fault facies analysis and modeling</i> .....	67
4.4. <i>Permeability analysis</i> .....	71
4.4.1. <i>Damage zones permeability analysis and modeling</i> .....	71
4.4.2. <i>Fault facies permeability analysis and modeling</i> .....	77
5. Discussion.....	81
5.1. <i>Characterization and modeling of damage zones and fault facies</i> .....	81
5.2. <i>Permeability and its connections with different deformational aspects in porous sandstones</i> .....	86
5.3. <i>Implications for CO<sub>2</sub> and petroleum reservoirs characterizations</i> .....	91
6. Conclusions .....	93
References .....	95
<i>Capítulo. 5</i> .....	108
5. <i>Conclusões e Sugestões para Trabalhos Futuros</i> .....	109
Referencias .....	112

## Lista de Figuras

**Fig. 1.1.** Mapa da localização da área de estudo (Bacia Rio do Peixe) no continente Sul-Americano e das principais bacias sedimentares (regiões amarelas) e zonas de cisalhamento (linhas pretas) no Nordeste do Brasil. As bacias sedimentares e zonas de cisalhamento foram baseadas em Matos (1992) e Brito Neves et al. (2000), respectivamente. Legenda – Zonas de Cisalhamento: ZCPE – Pernambuco; ZCP – Patos e ZCPA – Portalegre. BRP: Bacia Rio do Peixe. (Imagem obtidas a partir do GeoMapApp)

**Fig. 2.1.** Mapa geológico da BRP com as localizações dos afloramentos estudados: (1) Zona de falha e (2) as rochas não deformadas. As principais estruturas e unidades geológicas são baseadas em Sénant e Popoff (1991), Françaolin et al. (1994), Medeiros et al. (2005), Vasconcelos et al. (2021) e Ramos et al. (2022). Legendas – Zonas de Cisalhamento: ZCM – Malta; ZCPA - Portalegre; ZCRP – Rio Piranhas. Falhas: FM - Malta; FPA - Portalegre; FRP - Rio Piranhas; FSS - Sítio Sagui; FLF - Lagoa do Forno. Bacias e sub-bacias: BI - Icozinho; SBBF - Brejo das Freiras; SBS - Sousa; SBP – Pombal. DMA – Dorsal Mesoatlântica.

**Fig. 2.2.** Carta estratigráfica (adaptada a partir de Silva (2014) e Rapozo et al. (2021)) e perfil estrutural-estratigráfico da Bacia Rio do Peixe (adaptado de Vasconcelos et al. (2021)) com as formações do Grupo Rio do Peixe depositadas no Cretáceo Inferior e do Grupo Santa Helena depositadas no Devoniano Inferior. Legendas: AN – Antenor Navarro; S – Sousa; RP – Rio Piranhas; T – Triunfo; P – Pilões.

**Figura. 2.3.** Zonas de falha simples da BRP (A) sem e (B) com interpretação das bandas de deformação (linhas vermelhas contínuas). Zona de Falha complexa da BRP (C) sem e (D) com interpretação das bandas de deformação (linhas pretas contínuas). Detalhes das zonas de dano (*hangingwall*) da Falha Malta (E) com e (F) sem a interpretação das bandas de deformação.

Detalhes das zonas de dano (*hangingwall*) da Falha Portalegre (G) com e (F) sem a interpretação das bandas de deformação. Legendas: CL – Cluster de bandas de deformação; FW – *Footwall*; HW – *Hangingwall*.

**Fig. 3.1.** (A) Modelo de uma Zona de Falha Normal com seus principais elementos divididos conforme Caine et al. (1996) em núcleo da falha, zonas de dano e protólito. Em adição, tem-se os principais parâmetros geométricos das zonas. Os traços pretos nas zonas de dano são uma ilustração das estruturas subsidiárias (BD, juntas e/ou falhas) e sua distribuição. (B) Gráfico da frequência acumulada de estruturas de acordo com o modelo conceitual apresentado na Fig. 3.1A mostrando o comportamento dessa curva nos diferentes subdomínios das zonas de dano (zona de dano interna e externa, zona transicional e protólito). Observam-se flutuações das frequências na presença de falhas pequenas e com a interação entre zonas de dano (F1 e F2). (C) Curva da frequência das estruturas subsidiárias (F) com a distância do núcleo da falha (d) de acordo com o modelo da Fig. 3.1A. E os diferentes ajustes para o decaimento de F com relação a d, sendo os principais o logarítmico (Schueller et al., 2013) e os de lei da potência e linear (Celestino et al., 2020).

**Fig. 3.2.** Relação crescente entre rejeito real de falhas (A) e espessura do núcleo da Falha e (B) espessuras das zonas de dano. (Dados obtidos a partir de Alaei e Torabi, (2017) e Torabi et al. (2019, 2020))

**Fig. 3.3.** Ilustração e fotos de campo de bandas de deformação do tipo (A) *single*; (B) *Clusters* e (C) superfícies de deslizamento na Bacia Rio do Peixe. A foto de campo da Fig. 3.3C foi retirada de Nogueira et al. (2021).

**Fig. 3.4.** Principais tipos de bandas de deformação baseados em mecanismos deformacionais: (A) Bandas de desagregação; (B) Bandas filossilicáticas; (C) Bandas cataclásticas; e (D) Bandas de dissolução e cimentação. (Adaptada a partir de Fossen et al. (2007)).

**Fig. 3.5.** Modelos geológicos (Grid) que consideram as zonas de falhas como (A) superfícies e (B) como volumes.

**Fig. 3.6.** *Workflows* (A) convencional e (B) adaptado para a modelagem de reservatórios com zonas de falha (adaptado a partir de Syversveen et al. 2006.)

**Fig. 3.7.** *Workflow* usado por Qu et al. (2015) ilustrando o grid da zona de falha em (A) um corte transversal com a falha traçada, em (B) e (C) a base e o topo da zona de falha e em (D) somente o refinamento do grid nessa zona (retirado de Qu et al. 2015).

**Fig. 3.8.** Aplicação do algoritmo de Qu et al. (2015) para o refinamento de grids em diversos tipos de zona de falha (ZF). (A) falha curva, (B) rampa de revezamento, (C) e (D) intersecção entre falhas, (E) falhas inclinadas e (F) falhas com *hangingwall drag-fold* (retirado de Qu et al. 2015).

**Fig. 4.1.** (A) Model of a normal fault zone with its main elements subdivided according to Caine et al. (1996) in fault core, damage zones, and protolith. In the damage zone, the black lines represent the deformation bands, which tend to be more frequent near the fault core. Minor faults, represented here by segments in red, can also develop in the damage zone. The interband space (the adjacent region between two deformation bands) is also represented, as well as how the intensity of deformation bands (IDB) in a length T (DB/m) is calculated (more details are presented in the methods section). The accumulated thickness of deformation bands ( $t_{DB}$ ) and interband spaces ( $t_{IDB}$ ) is detailed. (B) Graph of deformation bands cumulative frequency and deformation band frequency (FDB) along of the footwall damage zone (A-A') used for

delimitation of the damage zone subdomains (Inner and outer damage zones and transitional zone) and damage zone width (DZW). Adapted from Berg and Skar (2005), Choi et al. (2016), and Torabi et al. (2020a).

**Fig. 4.2.** The geological map of the RPB with the outcrop locations representing the fault zone (outcrop 1) and the undeformed rocks (outcrop 2). The main structures and geologic units are based on Sénant and Popoff (1991), Medeiros et al. (2005), and Vasconcelos et al. (2021). Key – Shear Zones: PSZ – Patos; PASZ – Portalegre. Faults: MF – Malta; PAF – Portalegre; RPF – Rio Piranha; SSF – Sítio Sagui; LFF – Lagoa do Forno. Basin and sub-basins: IB – Icozinho; BFSB – Brejo das Freiras; SSB – Sousa; PSB – Pombal.

**Fig. 4.3.** (A) Detail of the undeformed sedimentary unit in outcrop 2 with its sedimentary facies represented by the Cg, CFS, and MS. The yellow circles are the point location of permeability measurements. (B) Unmanned Aerial Vehicle image from outcrop 1. The continuous black lines are the scanlines A, B, and C on the fault hanging wall. The solid white line represents the outcrop geological profile (Fig. 4.5A). The red squares are the points of permeability measurements.

**Fig. 4.4.** (A) Simplified workflow used in this study. (B) Digital model of outcrop 1, and location of the deformation band intensity data acquired along scanlines A, B, and C. Vertical exaggeration of 1.5x. (C) Spatial Relationship Classes between the facies  $H_{DB}$  (High deformation band intensity),  $M_{DB}$  (Medium deformation band intensity),  $L_{DB}$  (Low deformation band intensity), and  $N_{DB}$  (No deformation bands) (adapted from Qu and Tveranger, 2016).

**Fig. 4.5.** (A) Geological profile of the Malta Fault Zone segment (outcrop 1) and deformation band distribution and orientation in each architectural element. The Malta Fault Core comprises (B) breccia, (C) cataclasite, and gouge. Deformation bands arranged in the hanging wall damage



zone (D) in fine sandstones of the inner damage zone, (E) thicker in the outer damage zone, (F) widely spaced in the transitional zone, and (G) rarely occurring in protolith.

**Fig. 4.6.** Outcrop 1 pictures in the Malta Fault hanging wall damage zone, of (A) Antithetic minor normal faults in the inner/outer damage zones, synthetic minor normal faults in the (B) outer damage zone and (C) in the transitional zone, and (D) a detail of the protolith lithology, with no deformation bands. For more details on pictures localizations, see Fig. 4.5A.

**Fig. 4.7.** Frequency distribution and the deformation band cumulative frequency with respect to distance from the fault core on the hanging wall of the Malta Fault segment (outcrop 1 in Fig. 2). (A) Scanline A. (B) Scanline B. (C) Scanline C. Scanline A shows only the original data, whereas scanlines B and C exhibit the original and corrected data. The corrected data consist of the correction proposed by Choi et al. (2016) and the same gradient/width for the inner damage zone, coming from scanline A. Key: i.z = inner damage zone; o.z. = outer damage zone; t.z. = transitional zone.

**Fig. 4.8.** The damage zone model and the fault core integrated into the digital terrain model from the UAV image. (A) Top view with the scanlines location and (B) side view of the damage zone model. The model exhibits a vertical exaggeration of 1.5. (C) Stereogram orientations of deformation bands in each damage zone (inner and outer), transitional zone, and protolith.

**Fig. 4.9.** (A) Distribution of the deformation band intensities, at every meter along the scanlines A, B, and C, regarding the fault facies  $H_{DB}$ ,  $M_{DB}$ ,  $L_{DB}$ , and  $N_{DB}$ , and logarithmic decay (correlation) of deformation band intensity with the distance from fault core to fault facies  $H_{DB}$ ,  $M_{DB}$  and  $L_{DB}$  (red, orange, and yellow dots, respectively). (B) Fault facies ( $H_{DB}$ ,  $M_{DB}$ ,  $L_{DB}$ , and  $N_{DB}$ ) proportions according to scanlines data in the inner and outer damage zones, transitional

zone, and protolith. (C) Percentage transitions between fault facies analyzing all groups 0, 1, and 2 and analyzing (D) the groups 1 and 2.

**Fig. 4.10.** Fault facies distribution model in the Malta Fault segment (outcrop 1 in Fig. 4.2) with minor faults observed in the field. (B) Continuous model of the deformation band intensity obtained through the fault facies model (Fig. 4.10A) and logarithmic decay correlation of the deformation band intensity with the distance from the fault core (Fig. 4.9A). The models are shown with a vertical exaggeration of 1.5x. Key: i.z = inner damage zone; o.z. = outer damage zone; t.z. = transitional zone.

**Fig. 4.11.** (A) Horizontal (measured) and vertical (estimated from the relationship obtained by Shedid (2019) permeabilities profiles of undeformed rocks (outcrop 2 in Fig. 4.2). Details of the measurement points along conglomerates, medium sandstones, and fine to coarse sandstones are available in Fig. 4.3B (points 1 to 12). The solid red line shows the average permeability value by lithology. (B) Permeability diagram in the deformation bands and interband spaces for the inner and outer damage zone, transitional zone, and protolith along the Malta Fault segment (outcrop 2 in Fig. 4.1). The black lines within the box represent the median value. The black lines on the top and bottom are the maximum and minimum values, respectively. Permeability distribution reductions, in orders of magnitude, with the distance from the fault core of (C) the deformation bands and (D) interband spaces for each zone (inner and outer damage zone, transitional zone, and protolith) of the Malta Fault segment (outcrop 1 in Fig. 4.1) compared to undeformed rocks (coarse to fine sandstones in Fig. 4.11A).

**Fig. 4.12.** 3D models, conditioned to the damage zone model, of the (A) deformation band permeability ( $K_{DB}$ ), (B) interband spaces permeability ( $K_{IDB}$ ), and equivalent permeabilities (C) perpendicular,  $K_{EQ(x)}$ , and (D) parallel,  $K_{EQ(y)}$ , to the main fault. (E) Graph of equivalent permeability perpendicular ( $K_{EQ(x)}$ ) versus parallel ( $K_{EQ(y)}$ ) to the main fault modeled according

to the damage zone subdomains model (data from the  $K_{EQ(x)}$  and  $K_{EQ(y)}$  models, in Figs 12C, D). The models exhibit a vertical exaggeration of 1.5x. Key: i.z = inner damage zone; o.z. = outer damage zone; t.z. = transitional zone.

**Fig. 4.13.** (A) Permeability graph of the deformation bands and interband spaces for facies  $H_{DB}$ ,  $M_{DB}$ ,  $L_{DB}$ , and  $N_{DB}$ . The black lines within the box mean the median value. The black lines on the top and bottom mean the maximum and minimum values, respectively. Permeability reduction distribution, in orders of magnitude, in the (B) deformation bands and (C) interband spaces for the facies  $H_{DB}$ ,  $M_{DB}$ , and  $L_{DB}$  compared to facies  $N_{DB}$ , with the distance from the fault core.

**Fig. 4.14.** 3D models, conditioned to the fault facies model (Fig. 4.10), of the (A) deformation band permeability ( $K_{DB}$ ), (B) interband spaces permeability ( $K_{IDB}$ ), and equivalent permeabilities (C) perpendicular,  $K_{EQ(x)}$ , and (D) parallel,  $K_{EQ(y)}$ , to the main fault. (E) Graph of equivalent permeability perpendicular ( $K_{EQ(x)}$ ) versus parallel ( $K_{EQ(y)}$ ) to the main fault modeled according to the fault facies (data from the  $K_{EQ(x)}$  and  $K_{EQ(y)}$  models, in Fig. 4.14C, D). The models exhibit a vertical exaggeration of 1.5x. Key: i.z = inner damage zone; o.z. = outer damage zone; t.z. = transitional zone.

**Fig. 4.15.** (A) Conceptual model of the fault zone, with the main architectural elements, the footwall and hanging wall damage zones, and the fault core. In the hanging wall damage zone, the distribution of deformation bands and their configurations (anastomosed pattern) are illustrated, as well as the permeability tensor, parallel and perpendicular to the main fault, from A to A' throughout this zone. (B) logarithmic decay of the deformation bands frequency from the fault core towards the protolith, and exponential increase permeability (C) of the interband spaces and (D) deformation bands.

**Lista de Tabelas**

**Table 1.** Variogram parameters for modeling fault facies and equivalent permeabilities.

**Table 2.** General Characteristics of scanlines.

**Table 3.** Deformation band thickness in different subdomains of damage zones.

**Table 4.** Continuity of the fault facies (x-direction) in the inner and outer damage zones, transition zone, and protolith from scanline data.

**Table 5.** Distribution of equivalent permeability in the cells of the  $K_{EQ(x)}$  and  $K_{EQ(y)}$  models conditioned to the fault facies (FF) and damage zone subdomains (DZS) models.

# *Capítulo. 1*

## *Introdução*

## **1. Introdução**

### **1.1. Apresentação**

A presente dissertação descreve os resultados da pesquisa de mestrado da discente Maria Eduarda da Silva, sob orientação do Prof. Dr. Francisco César Costa Nogueira e coorientação do Prof. Dr. Yoe Alain Reyes Perez. Essa dissertação é requisito obrigatório a obtenção do título de mestre junto ao Programa de Pós-Graduação em Exploração Petrolífera e Mineral (PPGEPM) da Universidade Federal de Campina Grande (UFCG). No que se refere ao conteúdo científico desta dissertação de mestrado, buscou-se caracterizar, parametrizar e modelar as propriedades deformacionais (intensidade de deformação ou estruturas/m) e petrofísicas (permeabilidades direcionais) na Falha Malta, onde ocorre uma das principais zonas de falha da Bacia Rio do Peixe (BRP) (NE do Brasil).

Esta pesquisa de mestrado esteve vinculada ao projeto de Pesquisa e Desenvolvimento (P&D) "Bandas de deformação Rio do Peixe (DEBRIP): análise multiescalar e geração de banco de dados geofísico, geológico, modelagem e simulação numérica". O DEBRIP é um projeto da UFCG coordenado pelo Prof. Dr. Francisco César Costa Nogueira, em parceria e com financiamento da Petrobras, oferecendo esse projeto suporte técnico e financeiro a todas as atividades desta dissertação e bolsa-auxílio. Esta dissertação também conta com apoio da Schlumberger, que fornece licenças estudantis dos softwares de modelagem e simulação de reservatórios Petrel<sup>TM</sup> e Eclipse<sup>TM</sup> ao Laboratório de Exploração Petrolífera (LAPEP) da UFCG.

Em relação a forma, esta dissertação foi estruturada em cinco capítulos. O Capítulo 1 (Introdução) descreve a justificativa da pesquisa, seus objetivos, e localiza a área de estudo. Ainda neste capítulo, apresenta-se os financiadores e orientadores desta pesquisa. No capítulo

2 (Contexto Geológico), são apresentadas as principais características estratigráficas e tectônicas da BRP, bem como, das zonas de falha desta bacia. No Capítulo 3 (Fundamentação Teórica), tem-se um apanhado dos principais conceitos, estudos e técnicas para caracterização e modelagem geológica de zonas de falha. No Capítulo 4, são apresentados os resultados, de forma integrada a metodologia e discussões, por meio de um artigo científico publicado pela autora desta dissertação e colaboradores na revista *Marine and Petroleum Geology*. Por fim, no Capítulo 5 são apresentadas as conclusões e sugestões de trabalhos futuros.

## 1.2. Justificativa e Objetivos

Diversos estudos têm endereçado a importância de se compreender melhor as zonas de falhas constituídas por arenitos porosos onde as bandas de deformação (BD) podem ser os elementos dominantes (e.g., Fossen et al., 2007; Schueller et al., 2013; Awdal et al., 2020). Essa importância é caracterizada pelas BD serem estruturas tabulares com mm ou cm de espessura cujas propriedades petrofísicas (e.g., Antonellini e Aydin, 1994; Sorkhabi e Hasegawa, 2005; Fossen et al., 2007; Torabi e Fossen, 2009; Torabi et al., 2013; Ballas et al., 2015) e mecânicas são distintas com relação as rochas hospedeiras (e.g., Pontes et al., 2019; Del Sole et al., 2020; Oliveira et al., 2022). Assim, as BD tendem a exercer mudanças nas propriedades de fluxo de fluidos em meios porosos, tais como aumento da tortuosidade no meio poroso, que levam a impactos na recuperação de hidrocarbonetos e na capacidade de estocagem de CO<sub>2</sub> (e.g., Rotevatn et al., 2009; Rotevatn e Fossen, 2011; Fachri et al., 2011, 2013a, 2013b, 2016; Torabi et al., 2015; Romano et al., 2020; Awdal et al., 2020).

Considerando o impacto das BD nas propriedades de reservatórios, diversos estudos têm mostrado a importância de entender a arquitetura das zonas de falha (e.g., Caine et al., 1996; Torabi et al., 2019, 2020), bem como, o padrão de distribuição das estruturas presente nessas zonas (e.g., Berg e Skar, 2005; Braathen et al., 2009; Schueller et al., 2013; Choi et al., 2016;

Bistacchi et al., 2020; Martinelli et al., 2020). Em adição, cada vez mais tem-se também buscado representar as distribuições das propriedades petrofísicas e mecânicas das zonas de falha em modelos geocelulares 3D de reservatório (e.g., Qu e Tveranger, 2016; Awdal et al., 2020).

Visto as limitações da escala sísmica, diversos desafios ainda envolvem o estudo das zonas de falha com BD em escala de reservatório. Por exemplo, a distribuição das BD e/ou fraturas presentes nas zonas de falha, assim como a variação de suas propriedades estão posicionadas na escala sub-sísmica de investigação (Maerten et al., 2006; Botter et al., 2016; Fossen et al., 2017). Assim, o estudo em escala de afloramento vem se mostrando essencial para: (1) delimitação dos contornos das zonas de falhas que compreendem as BD, denominados de zonas de dano, incluindo a delimitação de subdomínios dessas últimas, conforme aspectos deformacionais (Berg e Skar, 2005; Choi et al., 2016; Torabi et al., 2020); (2) obtenção de relações entre os parâmetros geométricos das zonas de falha, visando a delimitação dos contornos dessas zonas em subsuperfície (e.g., Schueller et al., 2013; Choi et al., 2016; Alaei e Torabi, 2017; Ma et al., 2019; Torabi et al., 2020); (3) desenvolvimento de técnicas que permitam a caracterização e modelagem da distribuição dos principais elementos das zonas de falha em escala de reservatórios e suas propriedades petrofísicas, por exemplo usando o conceito de fácies de falha (corpos rochosos cujas propriedades são derivadas da deformação promovida pela ação tectônica) (e.g., Braathen et al., 2009; Fachri et al., 2011, 2013a, 2013b; Qu e Tveranger, 2016; Qu et al., 2017; Botter et al., 2017; Botter e Champion, 2019).

Por outro lado, poucos estudos têm endereçado sobre: (1) a distribuição da intensidade de BD (BD/m) nos diferentes subdomínios de zonas de dano de falhas de borda de bacias sedimentares (e.g., Araujo et al., 2018); (2) as permeabilidades das BD ( $K_{BD}$ ) e dos espaços interbanda ( $K_{IBD}$ ) (espaço entre duas bandas adjacentes ou rocha hospedeira), nos diferentes



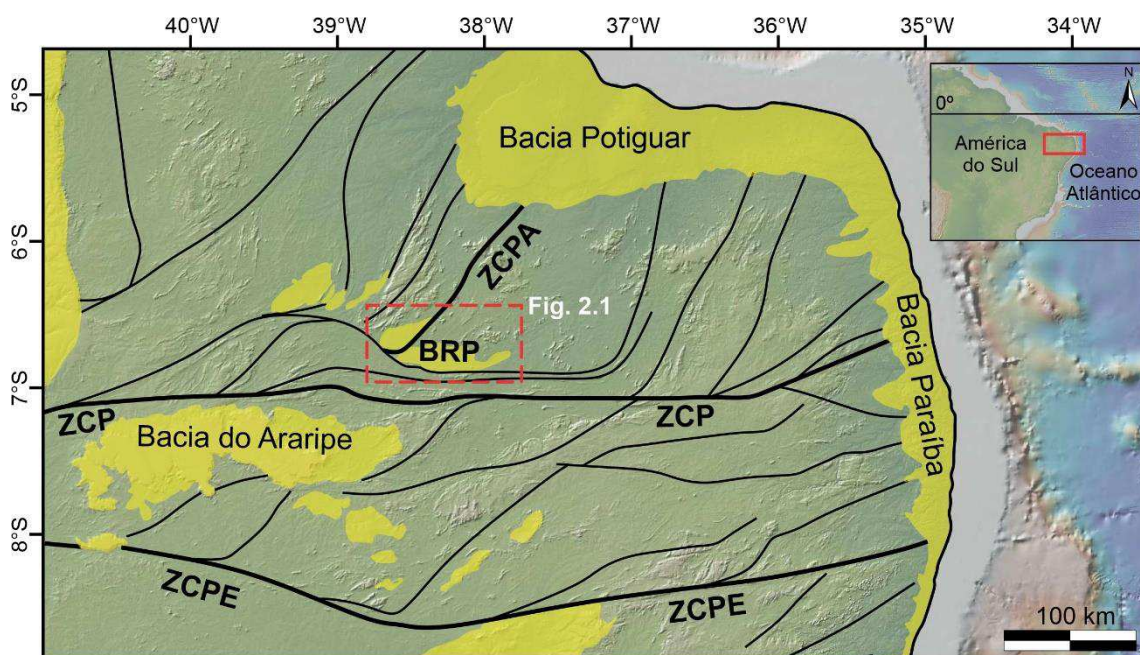
subdomínios internos as zonas de dano (regiões que concentram as bandas de deformação) e em diferentes fácies de falha (e.g., Sorkhabi e Hasegawa, 2005; Pizzati et al., 2020); (3) a importância da quantificação da  $K_{IBD}$  para o cálculo de permeabilidade equivalente; (4) qual a relação entre o padrão de distribuição de bandas de deformação e as propriedades petrofísicas; (5) e ainda sobre como incorporar à modelagem geológica esses diferentes padrões de distribuição de estruturas ou BD. Assim, esta dissertação tem como objetivos gerais entender como a intensidade de bandas de deformação se distribui ao longo de diferentes subdomínios das zonas de dano no *hangingwall* de uma falha de borda (*rift fault*) da BRP, e qual o impacto dessa intensidade na permeabilidade das bandas de deformação e nos espaços interbanda dessas zonas de dano, assim como, para modelagem da permeabilidade equivalente.

De forma complementar, são objetivos específicos desta pesquisa:

- Identificar em afloramento os elementos da Zona de Falha Malta e seus componentes;
- Caracterizar em afloramento os parâmetros deformacionais (intensidade de deformação ou BD/m, espaçamento de BD) e petrofísicos (porosidade) da zona de falha estudada;
- Delimitar e modelar os contornos das zona de falha em escala de afloramento;
- Delimitar e modelar os subdomínios das zonas de dano usando técnicas baseada nas distribuições das estruturas em afloramento;
- Modelar a distribuição de bandas de deformação nas zonas de dano da falha estudada usando o conceito de fácies de falha;
- Modelar as  $K_{BD}$  e  $K_{IBD}$  condicionadas as zonas de dano e fácies de falha, assim como quantificar as permeabilidades equivalentes ao longo desses modelos;
- Fazer uso de técnicas *upscaling* para modelagem.

### 1.3. Localização da Área de Estudo

De acordo com o contexto apresentado neste capítulo, a BRP (Fig. 1.1) mostrou-se uma excelente área de estudo, pela presença de extensos afloramentos que englobam zonas de falhas, a partir dos quais é possível caracterizar a arquitetura dessas zonas, seus elementos e propriedades estruturais e petrofísicas. A BRP está localizada no Nordeste brasileiro (Fig. 1.1), compondo o conjunto de bacia interiores formadas pela reativação rúptil de zonas de cisalhamento do embasamento Pré-cambriano durante a separação dos continentes Sul-Americano e Africano (Matos, 1992; Françolin et al., 1994; Nogueira et al., 2015; Ramos et al., 2022). Essa bacia é delimitada pelas longitudes  $37^{\circ}48'43''\text{W}$  e  $38^{\circ}42'40''\text{W}$  e latitudes  $6^{\circ}29'25''\text{S}$  e  $6^{\circ}50'58''\text{S}$  (Fig. 1.1) ocupando uma área de aproximadamente  $1265\text{ Km}^2$ .



**Fig. 1.1.** Mapa da localização da área de estudo (Bacia Rio do Peixe) no continente Sul-Americano e das principais bacias sedimentares (regiões amarelas) e zonas de cisalhamento (linhas pretas) no Nordeste do Brasil. As bacias sedimentares e zonas de cisalhamento foram baseadas em Matos (1992) e Brito Neves et al. (2000), respectivamente. Legenda – Zonas de Cisalhamento: ZCPE – Pernambuco; ZCP – Patos e ZCPA – Portalegre. BRP: Bacia Rio do Peixe. (Imagem obtidas a partir do GeoMapApp).

# *Capítulo. 2*

## *Contexto Geológico*

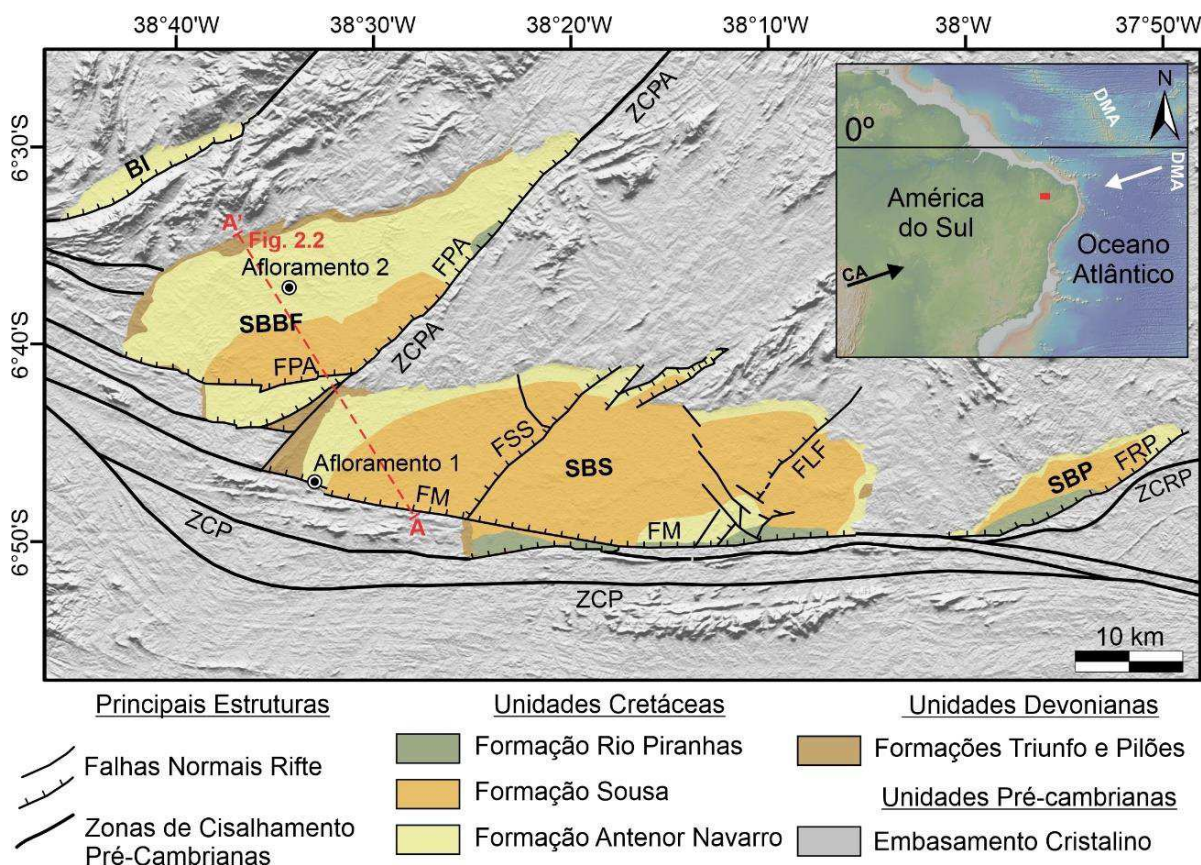
## 2. Contexto Geológico

### 2.1 Bacia Rio do Peixe

A BRP faz parte do conjunto de bacias intracontinentais, de pequeno e médio tamanho, localizado no nordeste do Brasil (Fig. 2.1). Essa bacia sedimentar foi formada durante a separação dos continentes sul-americano e africano, ou fragmentação do Pangeia no Cretáceo Inferior (145 e 130 Ma), sob um regime tectônico extensional de orientação NW–SE a NNW–SSE que desencadeou um processo regional de rifteamento (Sénant e Popoff, 1991; Matos, 1992; Françaolin et al., 1994; de Castro et al., 2007; Nogueira et al., 2015). O desenvolvimento do rifte na BRP foi controlado pela reativação rúptil das zonas de cisalhamento Malta (E-W), Portalegre (NE-SW) e Rio Piranhas (NE-SW) (Fig. 2.1) (Sénant e Popoff, 1991; Françaolin et al., 1994; de Castro et al., 2007; Nogueira et al., 2015; Vasconcelos et al., 2021; Ramos et al., 2022). Essas zonas de cisalhamento atuaram como zonas de fraqueza controlando a localização das falhas de borda ou delimitadoras da BRP (Falhas Portalegre (FPA), Malta (FM) e Rio Piranhas (FRP) na Fig. 2.1). No entanto, a geometria dessas falhas de borda não foram controladas pela foliação milonítica mas sim pelo contraste entre as unidades tectonometamórficas separadas pelas zonas de cisalhamento dúctil (Ramos et al., 2022). Por outro lado, essas falhas de borda também controlaram os principais depocentros da BRP, resultando no desenvolvimento de três sub-bacias ou semi-grabens: (1) Brejo das Freiras (SBBF); (2) Sousa (SBS), e (3) Pombal (SBP) (Fig. 2.1) (Sénant e Popoff, 1991; Françaolin et al., 1994; de Castro et al., 2007).

Posteriormente, ocorreu na BRP a mudança da tensão compressiva máxima ( $\sigma_1$ ) da vertical para a horizontal, de direção WSW–ENE associada ao campo de tensões compressivas opostas da Dorsal Mesoatlântica (DMA na Fig. 2.1) e da Cordilheira dos Andes (CA na Fig.

2.1), que levou a inversão tectônica dessa bacia entre o Cretáceo Superior (ca. 80 Ma) até os dias atuais (Nogueira et al., 2015; Vasconcelos et al., 2021).



**Fig. 2.1.** Mapa geológico da BRP com as localizações dos afloramentos estudados: (1) Zona de falha e (2) as rochas não deformadas. As principais estruturas e unidades geológicas são baseadas em Sénant e Popoff (1991), Françaolin et al. (1994), Medeiros et al. (2005), Vasconcelos et al. (2021) e Ramos et al. (2022). Legendas – Zonas de Cisalhamento: ZCM – Malta; ZCPA - Portalegre; ZCRP – Rio Piranhas. Falhas: FM - Malta; FPA - Portalegre; FRP - Rio Piranhas; FSS - Sítio Sagui; FLF - Lagoa do Forno. Bacias e sub-bacias: BI - Icozinho; SBBF - Brejo das Freiras; SBS - Sousa; SBP – Pombal. DMA – Dorsal Mesoatlântica.

O preenchimento sedimentar da BRP compreende rochas do Grupo Rio do Peixe (Cretáceo Inferior) dispendo-se em inconformidade sobre as rochas do Grupo Santa Helena (Devoniano Inferior) (Fig. 2.2A), que se sobrepõem às rochas do embasamento cristalino Pré-

Cambriano (Fig. 2.2.B) (Carvalho et al., 2013; Silva et al., 2014). Referindo-se as unidades estratigráficas, da base ao topo, na BRP (Fig. 2.2) essas são as seguintes: (1) Formação Pilões (Devoniano Inferior), predominantemente composta por siltitos e folhelhos, associados a ambientes deposicionais deltaico e fluvial-deltaico; (2) Formação Triunfo (Devoniano Inferior), constituída principalmente por arenitos e conglomerados fluvial-deltaicos de brancos a cinza; (3) Formação Antenor Navarro (Cretáceo Inferior) composta por arenitos finos a conglomeráticos e conglomerados fluviais; (4) Formação Sousa, dominada por depósitos lacustres, que compreendem intercalações de folhelhos e siltitos; e (5) Formação Rio Piranhas (Cretáceo Inferior), composta principalmente por conglomerados, com feldspatos e fragmentos líticos, associados a leques aluviais.

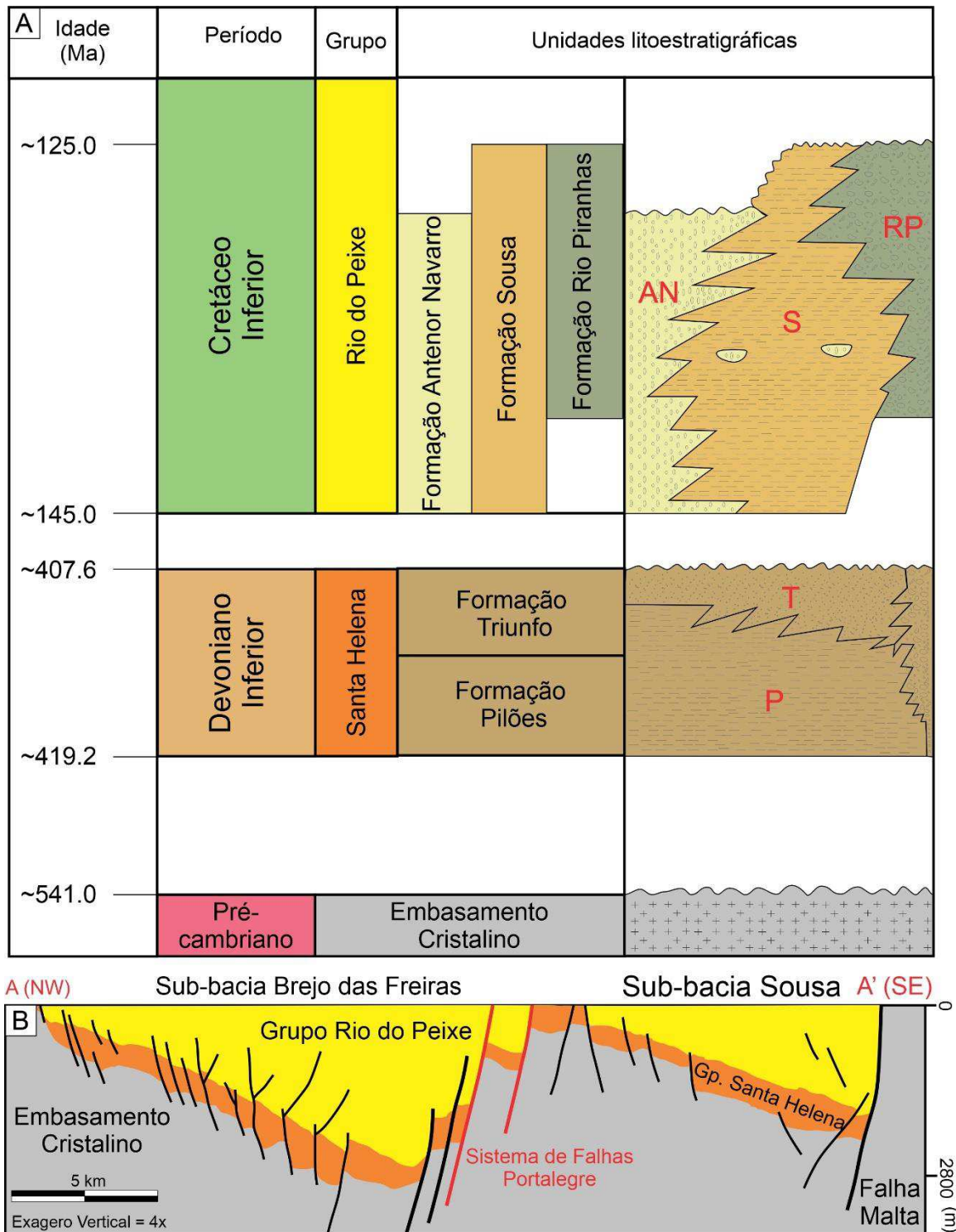
O Grupo Santa Helena foi formado num contexto pré-rifte em que pouco se conhece se sua origem é associada a origem mecânica (uma possível fase rifte no Devoniano) ou termal (uma fase *sag* no Devoniano) (Silva et al., 2014; Vasconcelos et al., 2021). Portanto, as unidades que compõem esse grupo necessitam ainda de mais estudos, inclusive a cerca de um melhor refinamento da idade utilizando-se de uma maior distribuição de análises palinológicas (Roesner et al., 2011). Após a deposição dessas unidades descritas como de idade Devoniana, um longo hiato de deposição ocorreu até o rifteamento Cretáceo responsável pela deposição das unidades do Grupo Rio do Peixe (Carvalho et al., 2013).

## **2.2. Zonas de Falha da Bacia Rio do Peixe**

Aspectos estruturais, composicionais, petrofísicos e geomecânicos das zonas de falha da BRP vem sendo amplamente estudados (e.g., Araujo et al., 2018; Maciel et al., 2018; Nicchio et al., 2018; Pontes et al., 2019; de Souza et al., 2021; Nogueira et al., 2021; Torabi et al., 2021; Oliveira et al., 2022; Silva et al., 2022; Souza et al., 2022). Diversos estudos mostraram que os elementos deformacionais predominantemente desenvolvidos nos arenitos finos a



conglomeráticos da Formação Antenor Navarro associados as principais zonas de falha da BRP (FPA e FM na Fig. 2.1) foram BD cataclásticas (Fig. 2.3) (Sénant e Popoff, 1991; Nogueira et al., 2015; Araujo et al., 2018; Nicchio et al., 2018; de Souza et al., 2021; Nogueira et al., 2021).



**Fig. 2.2.** (A) Carta estratigráfica (adaptada a partir de Silva (2014) e Rapozo et al. (2021)) e (B) perfil estrutural-estratigráfico da Bacia Rio do Peixe (adaptado de Vasconcelos et al. (2021)) com as formações do Grupo Rio do Peixe depositadas no Cretáceo Inferior e do Grupo Santa Helena depositadas no Devoniano Inferior. Legendas: AN – Antenor Navarro; S – Sousa; RP – Rio Piranhas; T – Triunfo; P – Pilões.

Com relação aos aspectos estruturais e composicionais das zonas de falha da BRP, Nicchio et al. (2018) propuseram que as BD cataclásticas se desenvolveram nos arenitos e conglomerados arcóseos da Formação Antenor Navarro em cinco estágios evolutivos, iniciados a partir da rotação de grãos, cominuição das bordas desses e cataclase moderada, evoluindo até a formação de estruturas semelhantes às do tipo S-C-C' (regime dúctil). Nicchio et al. (2018) também observaram que essas estruturas semelhantes às S-C-C' são compostas pelo alinhamento de fragmentos de feldspato ao longo de superfícies de deslizamento, associados a processos completamente mecânicos, sem a associação de argilas. Em adição, Maciel et al. (2018) relataram que (e.g., zona de falha ilustrada na Fig. 2.3A, B) a autigênese de argilas foi inibida, devido a barreira que as BD cataclásticas impuseram a percolação de fluidos meteóricos nessas zonas, e a redução de espaço (cataclase dos grãos). De Souza et al. (2021) apresentaram um modelo evolutivo multiescalar para as BD numa zona de falha na BRP (Fig. 2.3A, B), onde o processo intenso de cataclase associado a essas zonas é favorecido inicialmente pela clivagem de feldspatos e formação de *microcracks* que coalescem e evoluem para planos intermediários e posteriormente para a cominuição dos grãos.

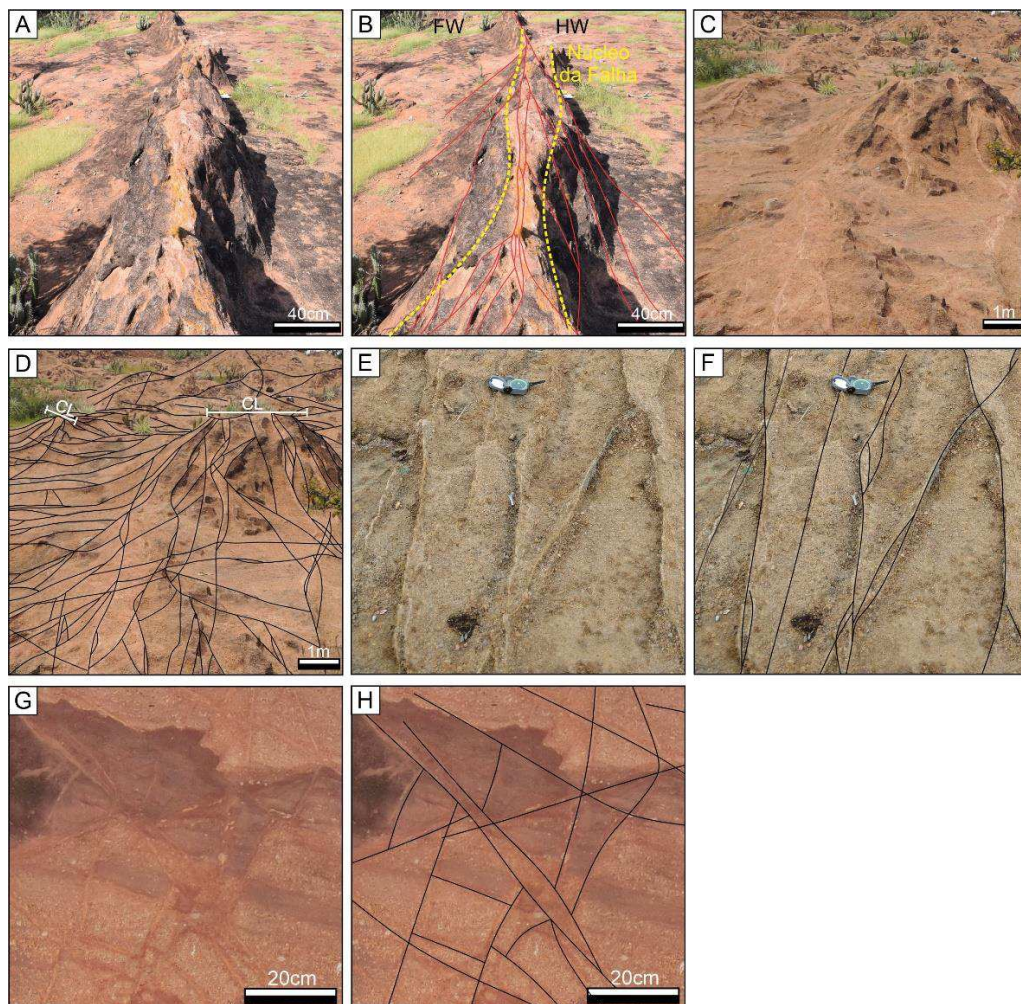
No que se refere aos aspectos estruturais, petrofísicos e/ou mecânicos: (1) Araujo et al. (2018) mostraram que as bandas de deformação na BRP seguem a cinemática e orientação das falhas de borda (Falhas Malta e Portalegre), apresentam decaimento logarítmico da frequência de BD com a distância do núcleo dessas falhas e variam em espessura a depender do tamanho



de grão dos arenitos/conglomerados; (2) Pontes et al. (2019) relataram a presença de zonas de falha simples (Fig. 2.3A, B, E, F) e complexas (Fig. 2.3C, D, G, H) na BRP, associadas a moderada deformação e a intensa deformação com repetição de núcleos ou Clusters (CL na Fig. 2.3D), respectivamente; (3) Pontes et al. (2019) também observaram a maior resistência a compressão uniaxial (UCS – *uniaxial compressive strength*) e os menores valores de porosidade estão associados as zonas de falhas complexas (Fig. 2.3C, D, G, H), onde nessas zonas os valores de UCS são até quatro vezes maiores que os das rochas não deformadas; (4) Nogueira et al. (2021) associaram a forte redução da porosidade e permeabilidade nessas zonas de falha complexas (Fig. 2.3C, D, G, H) a geração de matriz cataclástica associada a diferentes intensidades de catacláse nas BD; (5) Torabi et al. (2021) mostraram que um processo de *hard linkage* (zona de falha da Fig. 2.3A, B) influencia a variação da espessura do núcleo e frequência de BD em uma zona de falha, de modo que quanto maior a espessura desse núcleo menores os valores de permeabilidade e porosidade e maiores os limites da pressão capilar; e (6) Oliveira et al. (2022) observaram que a estratigrafia mecânica influencia as características geométricas das BD tais como *dip*, espessura e intensidade de deformação (BD/m), onde por exemplo, quanto maior a porosidade, menores os valores de UCS, e maiores as intensidades de BD.

Em adição, outros trabalhos foram desenvolvidos na zonas de falha da BRP a fim de propor workflows para modelagem dessas zonas e entender a influência das bandas de deformação no fluxo de fluidos (e.g., Stohler, 2021; Souza et al., 2022). Por exemplo, Stohler (2021) observou através de simulações de fluxo de fluidos que a incorporação das zonas de dano na modelagem é importante visto a influência dessas nas propriedades de reservatórios óleo, tais quais: saturação de água, pressão de poros e produção de hidrocarbonetos. Assim, a partir do workflow gerado por Stohler (2021) para modelagem das zonas de falha a partir de dados da BRP, que considera a variação na intensidade das bandas de deformação ao longo

dessas zonas bem como sua obliquidade, seria possível aumentar a previsibilidade do comportamento de reservatórios associados a essas zonas. Por outro lado, Souza et al. (2022) observaram a partir da caracterização petrofísica, modelagem 2D de uma zona de falha da BRP e simulações de fluxo de fluidos que: (1) As bandas de deformação atuam como barreiras parciais ao fluxo de fluidos; (2) a pressão no espaço interbandas (entre duas bandas adjacentes) pode ser reduzida entre 10% e 40% a depender do sentido de fluxo; e (3) o comportamento das bandas de deformação como barreiras parciais está diretamente associado ao contraste de permeabilidade entre as bandas de deformação e o meio interbanda.



**Figura. 2.3.** Zonas de falha simples da BRP (A) sem e (B) com interpretação das bandas de deformação (linhas vermelhas contínuas). Zona de Falha complexa da BRP (C) sem e (D) com

interpretação das bandas de deformação (linhas pretas contínuas). Detalhes das zonas de dano (*hangingwall*) da Falha Malta (**E**) com e (**F**) sem a interpretação das bandas de deformação. Detalhes das zonas de dano (*hangingwall*) da Falha Portalegre (**G**) com e (**H**) sem a interpretação das bandas de deformação. Legendas: CL – Cluster de bandas de deformação; FW – *Footwall*; HW – *Hangingwall*.

# *Capítulo. 3*

## *Fundamentação Teórica*

### 3. Fundamentação Teórica

#### 3.1. Zonas de Falha

Falhas geológicas por vezes são consideradas como superfícies ou descontinuidades (Manzocchi et al., 1999; Tveranger et al., 2004; Shipton et al., 2005). No entanto, essas falhas são volumes ou zonas deformadas, de até km de largura (e.g., Ma et al., 2019), onde as propriedades das rochas são heterogêneas (Caine et al., 1996; Faulkner et al., 2010; Torabi et al., 2013; Balsamo et al., 2019; Pizzati et al., 2020). Devido a heterogeneidade das propriedades ao longo dessas zonas de falha e suas implicações para aquíferos, reservatórios de petróleo e de armazenamento de CO<sub>2</sub> (Medeiros et al., 2010; Torabi et al., 2015; Wilson et al., 2019), diversos estudos vêm buscando entender: (1) sua arquitetura/elementos (e.g., Berg e Skar, 2005; Choi et al., 2016; Torabi et al., 2019, 2020) e a distribuição dos seus componentes (rochas e/ou estruturas) (e.g., Schueller et al., 2013; Soliva et al., 2016; Bistacchi et al., 2020); e (2) as suas propriedades petrofísicas (e.g., Torabi et al., 2013; Ballas et al., 2015; Romano et al., 2020; Pizzati et al., 2020).

##### 3.1.1. Arquitetura, Elementos e Componentes das Zonas de Falha

Caine et al. (1996) delimitaram as zonas de falhas como sendo constituídas por três elementos principais, sendo esses o (1) núcleo da falha, as (2) zonas de dano (Fig. 3.1A) envoltas por rochas pouco ou não deformadas denominadas de (3) protólito (Fig. 3.1A). O núcleo de falha é o volume que concentra maior deformação e rejeito (Fig. 3.1A), sendo composto por rochas de falha, tais como, brechas, cataclasitos, *gouges*, rochas modificadas quimicamente, superfícies de deslizamento, dentre outros tipos de rochas e estruturas (Caine et al., 1996; Micarelli et al., 2003; Wibberley et al., 2007; Braathen et al., 2009; Childs et al., 2009; Torabi et al., 2019 e suas referências). Por outro lado, as zonas de dano (Fig. 3.1A) são

menos deformadas e predominantemente constituídas por estruturas subsidiárias, por exemplo, juntas e ou BD, estando também presentes falhas de pequeno rejeito e comprimento (falhas secundárias) nessas zonas (veja as falhas F1, F2 e Falhas Secundárias na Fig. 3.1.A) (Faulkner et al., 2010; Torabi e Berg, 2011; Choi et al., 2016 e suas referências; Torabi et al., 2020). O protólito é o elemento onde as estruturas subsidiárias não ocorreram ou ocorrem em menor frequência, não estando essas diretamente relacionadas ao processo de formação da zona de falha, mas com estruturas preexistentes (provenientes da sedimentação) (Choi et al., 2016; Torabi et al., 2020 e suas referências).

A arquitetura das zonas de falha tem sido cada vez mais estudada a partir de relações entre parâmetros geométricos, tais como rejeito real e vertical das falhas (RR e RV na Fig. 3.1A), comprimento das falhas (CF na Fig. 3.1A), espessura do núcleo (EN na Fig. 3.1A) e das zonas de dano (EZD na Fig. 3.1B) (e.g., Torabi e Berg, 2011; Choi et al., 2016; Alaei e Torabi., 2017; Fossen et al., 2017; Araujo et al., 2018; Torabi et al., 2019, 2020; Ma et al., 2019; Celestino et al., 2020). Relações positivas foram observadas entre o rejeito máximo das falhas (D) e o comprimento dessas (L) (relação D/L), dadas por uma lei da potência do tipo  $D = \gamma L^n$  (e.g., Clark e Cox, 1996), onde  $\gamma$  está relacionado as propriedades mecânicas das rochas e  $n$  é um fator de escala (Torabi e Berg, 2011). Além disso, as relações D/L tendem a ser maior em falhas do tipo *strike-slip* em comparação as falhas normais e reversas, e em falhas pequenas e grandes, comparadas as falhas médias (Torabi e Berg, 2011). No entanto, apesar das relações D/L serem maiores nas falhas pequenas, as BD, que são os principais elementos das zonas de dano em rochas porosas, têm baixas relações D/L (Fossen et al., 2007). Essas baixas relações D/L das BD estão relacionadas a limitação da propagação vertical dessas estruturas em camadas pouco porosas, fazendo com que a maior propagação dessas seja na horizontal (Fossen et al., 2007, 2017 e suas referências).





**Fig. 3.1.** (A) Modelo de uma Zona de Falha Normal com seus principais elementos divididos conforme Caine et al. (1996) em núcleo da falha, zonas de dano e protólito. Em adição, tem-se os principais parâmetros geométricos das zonas. Os traços pretos nas zonas de dano são uma ilustração das estruturas subsidiárias (BD, juntas e/ou falhas) e sua distribuição. (B) Gráfico da frequência acumulada de estruturas de acordo com o modelo conceitual apresentado na Fig. 3.1A mostrando o comportamento dessa curva nos diferentes subdomínios das zonas de dano (zona de dano interna e externa, zona transicional e protólito). Observam-se flutuações das frequências na presença de falhas pequenas e com a interação entre zonas de dano (F1 e F2). (C) Curva da frequência das estruturas subsidiárias (F) com a distância do núcleo da falha (d) de acordo com o modelo da Fig. 3.1A. E os diferentes ajustes para o decaimento de F com relação a d, sendo os principais o logarítmico (Schueller et al., 2013) e os de lei da potência e linear (Celestino et al., 2020).

As relações D/L também podem ser variáveis numa zona de falha ao longo do estágio evolutivo dessas zonas ou ‘falhamento’. Por exemplo, Jackson e Rotevatn (2013) observaram em uma zona de falha normal que falhas linkadas de mesma cinemática dentro do sistema de falha analisado cresceram rapidamente em comprimento, e só posteriormente em profundidade (rejeito), enquanto falhas isoladas do mesmo sistema cresceram em comprimento, a partir de incrementos em rejeito. Observações semelhantes foram feitas em um sistema de falhas do campo de óleo Wangxuzhuang na China por Liao et al. (2020a). As zonas de falha, desse campo apresentaram altas relações D/L, associadas a zonas de dano espessas (acima de 200 m), as quais os autores sugeriram ser a relação D/L de um segundo estágio de falhamento, com aumento de D sem incremento em L.

Similarmente as relações D/L, as relações entre o rejeito (D) e a espessura do núcleo das falhas (T) (EN na Fig. 3.1A) também seguem uma lei de potência, dada por  $T = aD^n$ , onde  $a$  é



uma constante de proporcionalidade e  $n$  é um expoente (constante) (e.g., Evans et al., 1990; Shipton et al., 2006; Torabi et al., 2019a). As relações T/D são positivas (Fig. 3.2A), sendo que diversos fatores podem interferir nessas, dentre os quais tem-se a geometria das falhas, os tipos de rochas de falha no núcleo, a litologia, interações ou lincagens entre falhas etc. (Fig. 3.2A) (Shipton et al., 2006; Torabi et al., 2019). As leis de potência para T e D tem variações com a escala das falhas analisadas, sendo que falhas com pequenos rejeitos de até 1 m mostram leis de potência com alto gradiente, decrescendo o gradiente acima desse ponto (Torabi e Berg, 2011). Por exemplo, Torabi et al. (2019) atribuíram isso a uma maior localização da deformação em falhas associados a muitos ciclos de deformação, onde *fault lenses* podem ser retrabalhados e originarem *gouges*, os quais não aumentam de forma expressiva o tamanho do núcleo, ou seja, ele torna-se mais localizado.

Diversos estudos também têm endereçado relações positivas entre rejeito real/vertical (D) com a espessura das zonas de dano (Fig. 3.2B) (EZD na Fig. 3.1) (e.g., Choi et al., 2016; Alaei e Torabi, 2017; Araujo et al., 2018; Ma et al., 2019; Torabi et al., 2020; Celestino et al., 2020). As relações EZD *versus* D normalmente se dão por lei de potência ( $EZD = aD^n$ ), com expoentes e coeficientes variando de acordo com a localidade analisada (e.g., Araujo et al., 2018; Celestino et al., 2020), tipos de estruturas presentes nas zonas de dano (BD ou fraturas e juntas) (e.g., Choi et al., 2016) e com a escala das falhas (e.g., Torabi et al., 2020). A construção das relações EZD/D vem se dando especialmente devido a técnicas de caracterização das zonas de dano em afloramento (e.g., Berg e Skar, 2005; Schueller et al., 2013; Bistacchi et al., 2020), visto a limitação da resolução sísmica para identificação da variação das propriedades dessas zonas (Maerten et al., 2006; Botter et al., 2016). Apesar disso, alguns estudos mais recentes já vêm observando a arquitetura dessas zonas a partir do uso de atributos sísmicos (e.g., Iacopini et al., 2016; Alaei e Torabi, 2017; Ma et al., 2019; Liao et al., 2020a, b).

No que se refere as técnicas de caracterização das zonas de dano em afloramento, existem três técnicas consolidadas para a delimitação dos contornos ou espessura dessas zonas. A primeira dessas técnicas utiliza a frequência acumulada de estruturas (BD ou fraturas) (Fig. 3.1B) com a distância do núcleo da falha para delimitação de subdomínios das zonas de dano e sua espessura (Berg e Skar, 2005). Berg e Skar (2005) observaram a partir de dados da Falha de Moab (SE de Utah) que a curva de frequência acumulada de estruturas apresenta diferentes gradientes (Fig. 3.1B), onde de acordo com esses autores: (1) o alto gradiente desta curva está associado a uma zona de dano interna (zdi. na Fig. 3.1B) de alta deformação; (2) um gradiente não-linear ou de menor gradiente delimita as extensões de uma zona de dano externa (zde na Fig. 3.1B); (3) a curva com baixo gradiente está associada a uma zona transicional (zt na Fig. 3.1B); (4) e a curva constante associada ao protólito (Fig. 3.1B). Segundo esses mesmos autores, a espessura da zona de dano seria delimitada pelas intercepções das curvas/gradientes da zona transicional e protólito.

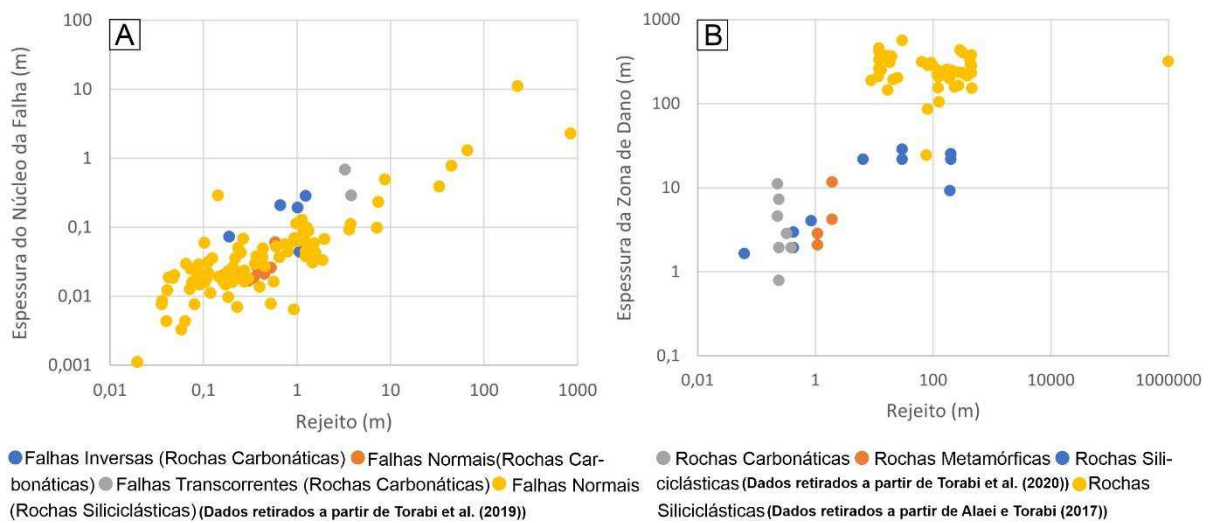
Em seguida, a metodologia proposta por Berg e Skar (2005) foi adaptada a fim de permitir a delimitação dos contornos dessas zonas mesmo quando se tem *gaps* ou ausência de dados ao longo das linhas de varredura/*scanline* que fornecem os dados das curvas de frequência acumulada. Assim, Choi et al. (2016) propuseram uma correção usando os gradientes das regiões anterior e posterior aos *gaps*, para tornar a delimitação dos contornos possível. Em adição, esses autores também observaram quais os reflexos das falhas secundárias (FS na Fig. 3.1) nessas curvas de frequência acumulada, onde eles notaram que os gradientes são levemente alterados (flutuações na curva) quando as falhas ocorrem nas zonas de dano (Fig. 3.1A). Observações semelhantes foram feitas por Soliva et al. (2016), no entanto nos gráficos de frequência com a distância da falha (Fig. 3.1C), de modo que esses observaram que a presença de falhas nas zonas de dano está associada a um padrão polimodal ou com repetição

de ‘picos’ nessas curvas. No entanto, outros fatores também podem levar a essas flutuações ou padrão polimodal, como por exemplo, ‘clusterização’, mudança nas propriedades mecânicas das camadas, ou até interação das zonas de dano de diferentes falhas (e.g., F1 e F2 na Fig. 3.1A).

A segunda técnica foi analisada em zonas de danos composta de BD por Schueller et al. (2013). Essa metodologia baseia-se na distribuição espacial das estruturas, frequência (F) *versus* distância do núcleo da falha (d). Esses autores sugeriram a partir de dados de 106 afloramentos que as BD seguem um decaimento logarítmico ( $F = \log A + C \log(d)$ , onde C = Cte. e  $\log A =$  Frequência máxima de estruturas) (ver Fig. 3.1C) da frequência com a distância do núcleo. Assim, a partir da frequência *background* do protólito é possível determinar a espessura dessas zonas pela intercessão da curva com o eixo *x* ou *d* (EZD na Fig. 3.1C). No entanto, alguns outros ajustes de curvas já foram reportados para o decaimento da frequência com a distância do núcleo, como por exemplo ajustes lineares e de lei da potência (Fig. 3.1C).

A última técnica é baseada em testes estatísticos que possibilitam a compreensão da configuração de distribuição espacial das estruturas nas zonas de dano (Fig. 3.1A) (Bistacchi et al., 2020). O principal parâmetro analisado é o espaçamento das estruturas, e as funções de espaçamento cumulativo (*CSF – Cumulative Spacing Function*) e a derivada dos espaçamentos cumulativos (*CSD – Cumulative Spacing Derivative*).

Todas essas técnicas vêm possibilitando as construções de relações (EZD/D) mais confiáveis (Torabi et al., 2020) para a modelagem de zonas de falha em escala de reservatório (Fachri et al., 2016; Qu e Tveranger, 2016). Em adição, a delimitação dos contornos é especialmente importante, pois ela condiciona a caracterização e modelagem das propriedades petrofísicas dessas zonas (Fachri et al., 2011).



**Fig. 3.2.** Relação crescente entre rejeito real de falhas (A) e espessura do núcleo da falha e (B) espessuras das zonas de dano. (Dados obtidos a partir de Alaei e Torabi, (2017) e Torabi et al. (2019, 2020))

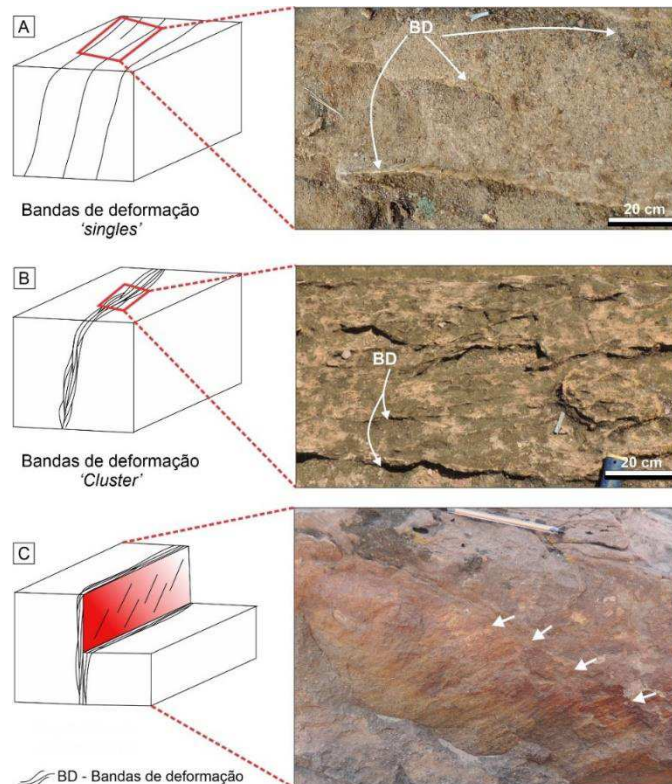
### 3.2. Zonas de Falha em Arenitos Porosos

O núcleo de falhas associadas a grandes rejeitos (>100 m) tendem a ser mais localizados que aquelas com rejeitos menores (Torabi et al., 2019). No entanto, grandes rejeitos estão associados a zonas de dano espessas (Schueller et al., 2013; Alaei e Torabi, 2017; Ma et al., 2019). Assim, diversos estudos têm buscado compreender além da delimitação dos contornos das zonas de dano (e.g., Schueller et al., 2013; Choi et al., 2016; Bistacchi et al., 2020; Liao et al., 2020a,b), as propriedades petrofísicas das zonas de dano, notadamente aquelas afetadas por BD cataclásticas, estruturas com grande contraste dessas propriedades em relação as rochas hospedeiras (e.g., Antonellini e Aydin, 1994; Torabi e Fossen, 2009; Ballas et al., 2015; Pizzatti et al., 2020; Nogueira et al., 2021).

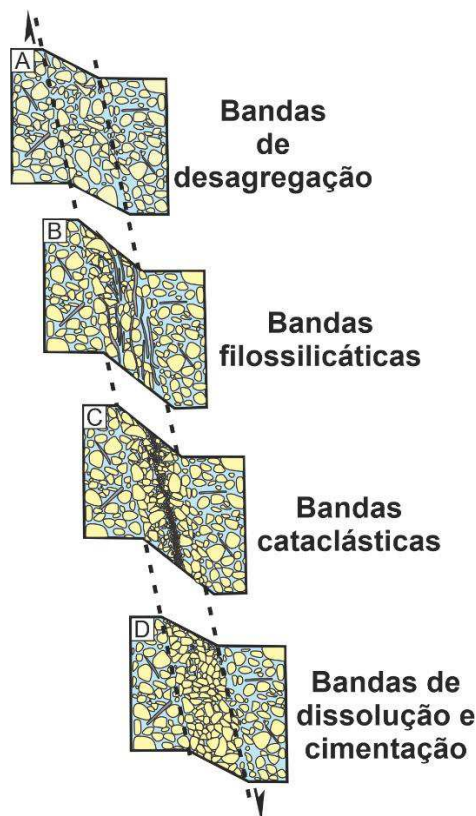
#### 3.2.1. Bandas de Deformação

As BD são as principais estruturas deformacionais desenvolvidas nas zonas de dano constituídas por rochas porosas (Porosidade > 15%) (Tondi, et al., 2006; Fossen et al., 2007;

Fachri et al., 2011; Rotevatn et al., 2016; Cavailhes e Rotevatn, 2018; Barão et al., 2020). As BD são estruturas tabulares de mm a cm de espessura (Fig. 3.3A, B) (Fossen et al., 2007), que se apresentam como estruturas únicas ‘*singles*’ (Fig. 3.3A) ou em conjuntos ‘*clusters*’ (Fig. 3.3B). Essas BD podem evoluir para superfícies de deslizamento (Fig. 3.3C), associadas normalmente a maior cataclase ou cominuição/‘quebra’ de grãos e rejeito (Fossen et al., 2007, 2017). Além disso, as BD podem ser classificadas segundo Fossen et al. (2007) de acordo com os mecanismos deformacionais atuantes em seus desenvolvimentos em: (1) BD de desagregação (Fig. 3.4A), associadas a fluxo granular onde os grãos rotacionam e tem-se o rompimento do cimento; (2) BD cataclásticas (Fig. 3.4C), estando associadas a fluxos cataclásticos que envolvem a quebra de grãos (cataclase) e redução significativa de poros; (3) BD filossilicáticas (Fig. 3.4B), quando o conteúdo de material argiloso é superior a 10–15%, essas BD são consideradas também um tipo específico de BD de desagregação; e por fim (4) BD de dissolução e cimentação (Fig. 3.4D), são BD associadas a compactação química ou a precipitação de materiais diagenéticos após a deformação.



**Fig. 3.3.** Ilustração e fotos de campo de bandas de deformação do tipo (A) *single*; (B) *Clusters* e (C) superfícies de deslizamento na Bacia Rio do Peixe. A foto de campo da Fig. 3.3C foi retirada de Nogueira et al. (2021).



**Fig. 3.4.** Principais tipos de bandas de deformação baseados em mecanismos deformacionais: (A) Bandas de desagregação; (B) Bandas filossilicáticas; (C) Bandas cataclásticas; e (D) Bandas de dissolução e cimentação. (Adaptada a partir de Fossen et al. (2007)).

As BD cataclásticas podem ter porosidades menores que 1%, e as permeabilidades reduzidas em até 7 ordens de magnitude com relação as rochas hospedeiras (Ballas et al., 2015; Pizzati et al., 2020). No que se refere a porosidade das BD, a redução normalmente está relacionada a intensidade de cataclase ou cominuição dos grãos que por sua vez está associada a geração de matriz cataclástica, que ocupa os poros da rocha hospedeira (Torabi e Fossen, 2009; Pontes et al., 2019; Nogueira et al., 2021). Quanto a permeabilidade das BD ( $K_{BD}$ ), essa

é influenciada por diversos fatores, mas que por sua vez também estão relacionados a processos cataclásticos ou intensidade desses processos (Alikarami et al., 2013; Torabi et al., 2013; Ballas et al., 2015; Pizatti et al., 2020; Nogueira et al., 2021).

### **3.2.2. Propriedades Petrofísicas das Bandas de Deformação, Espaços Interbanda e Núcleo de falhas**

A distribuição das propriedades petrofísicas ao longo de zonas de falha com BD é afetada por fatores internos e externos (Schultz e Siddharthan, 2005; Fossen et al., 2007; Ballas et al., 2015). Dentre os fatores internos que afetam essa distribuição têm-se a mineralogia, porosidade, forma e comportamento dos grãos, mecanismos de deformação e até o grau de litificação da rocha (Fossen et al., 2007; Torabi et al., 2013). Por outro lado, são considerados fatores externos o regime tectônico, profundidade de soterramento, e configuração da zona de falha (e.g., se há interação entre falhas ou não) (Ballas et al., 2015).

Dentre os fatores externos que determinam a  $K_{BD}$ , os regimes tectônicos influenciam no contraste de permeabilidade das BD com relação as rochas hospedeiras ( $K_{RH}$ ), de modo que o regime de falha normal é o que tende a gerar bandas com menor permeabilidade ou maiores contrastes dessa com relação a rocha hospedeira (Ballas et al., 2015). Os menores valores de  $K_{BD}$  do regime de falha normal são associadas a maior concentração de *stress* que ocorre nesse regime que por sua vez favorece processos cataclásticos (Ballas et al., 2015). A redução de permeabilidade também ocorre em sentido decrescente das BD do tipo *singles* (Fig. 3.3A) até o núcleo de falhas, passando pelas bandas do tipo *clusters* (Fig. 3.3B) e superfícies de deslizamento (Fig. 3.3C) (Torabi et al., 2013). Essa tendencia foi associada aos processos cataclásticos mais intensos que ocorrem no núcleo das falhas em detrimento das outras estruturas (Torabi et al., 2013, 2021; Ballas et al., 2015). Por outro lado, esses processos

cataclásticos estão diretamente relacionados ao acúmulo de rejeito ao longo das zonas de falha (Pizatti et al., 2020).

Além da redução das  $K_{BD}$ , Sorkhabi e Hasekawa (2005) também observaram em uma zona de falha na Malásia, que as  $K_{RH}$  internas as zonas de falha, foram reduzidas em até uma 1 ordem de magnitude com relação as rochas não deformadas. Esses autores associaram essa redução a compactação tectônica atuante em toda zona de falha. No entanto, Debenham et al. (2019) relataram que as reduções de permeabilidade da rocha hospedeira em zonas de falha pode estar associadas a cataclase de grãos individuais, principalmente próximo ao núcleo da falha a partir de dados de zonas de falha da Bacia de Otway (SE Australia). Em adição, essas reduções das permeabilidades das zonas de dano (estruturas e rocha hospedeira) estão associadas também ao tipo de estruturas desenvolvidas nas zonas de dano, por exemplo, se são fraturas ou BD, e a frequência dessas estruturas (Alikarami et al., 2013).

Quanto ao núcleo de falha, as propriedades são variáveis a depender das rochas de falha que o compõem. De forma geral, quando estão associados com processos de cataclase, esses núcleos podem atuar como barreiras (e.g., Shipton et al., 2002; Balsamo e Storti, 2010; Faulkner et al., 2010; Torabi et al., 2013, 2021) ou condutos (Farrel et al., 2014) ao fluxo de fluidos. Por exemplo, Balsamo e Storti (2010) observaram em um sistema extensional de falhas com rejeito inferior a 30 m (subsísmicas) que a permeabilidade do núcleo se relaciona com o rejeito das falhas. As falhas analisadas por esses autores tiveram reduções em até três ordens de magnitude no núcleo, enquanto as BD nas zonas de dano de até 2 ordens. Além disso, o núcleo das falhas analisadas em Utah (Estados Unidos) também se mostraram como barreiras capilares, até mais efetivas que as próprias BD, podendo essas exercerem barreiras hidrostáticas > 140 m (Torabi et al., 2013). Shipton et al. (2002) observaram valores de até 1.4 mD para o núcleo das falhas, constatando assim que a geometria dessas estruturas associadas a permeabilidade pode ter



grandes influência sobre as propriedades hidráulicas de reservatórios. Por outro lado, Torabi et al. (2021) observaram que a espessura do núcleo da falha pode ter relação com a permeabilidade e porosidade. A partir dos dados de um afloramento da BRP, Torabi et al. (2021) observaram que quanto maior a espessura do núcleo da falha analisada menores os valores de porosidade e permeabilidade desse. Em adição, esses autores também observaram uma relação anisotrópica para as permeabilidade paralela e perpendicular ao *dip* da falha. No entanto, alguns dos elementos do núcleo, como por exemplo *gouges* de falha, podem ter permeabilidade superior a 200 mD (e.g., Pizatti et al., 2020), o que podem torná-los barreiras pouco efetivas. Um exemplo, de núcleo de falha associado a processos cataclásticos, que pode atuar como conduto, foi apresentado por Farrel et al. (2014). Esses autores observaram que os processos deformacionais podem alterar a configuração dos poros em microescala e assim gerar condutores paralelamente a essas.

Diversos estudos também descrevem a anisotropia das propriedades petrofísicas ao longo das zonas de falha (e.g., Antonellini e Aydin, 1994; Balsamo et al., 2012; Farrel et al., 2014). Assim, tem-se que a menor permeabilidade ocorre perpendicular as BD e variam entre uma e duas ordens de magnitude com relação a permeabilidade paralela a essas (Antonellini e Aydin, 1994). Observações semelhantes foram feitas por Farrel et al. (2014), no entanto associadas a planos de falha, de modo que a anisotropia de permeabilidade medida chegou a 4 ordens de magnitude entre as diferentes direções.

Por fim, busca-se com as análises das propriedades petrofísicas de cada um dos elementos das zonas de falha quantificar valores efetivos dessas propriedades, a fim de serem incorporados a modelos geológicos (e.g., Cardwell e Parsons, 1945; Odling et al., 2004; Qu et al., 2017) e simulado o comportamento do fluxo de fluidos nessas zonas (Souza et al., 2022). Assim, a quantificação das propriedades petrofísicas (equivalentes e/ou efetivas) são feitas a

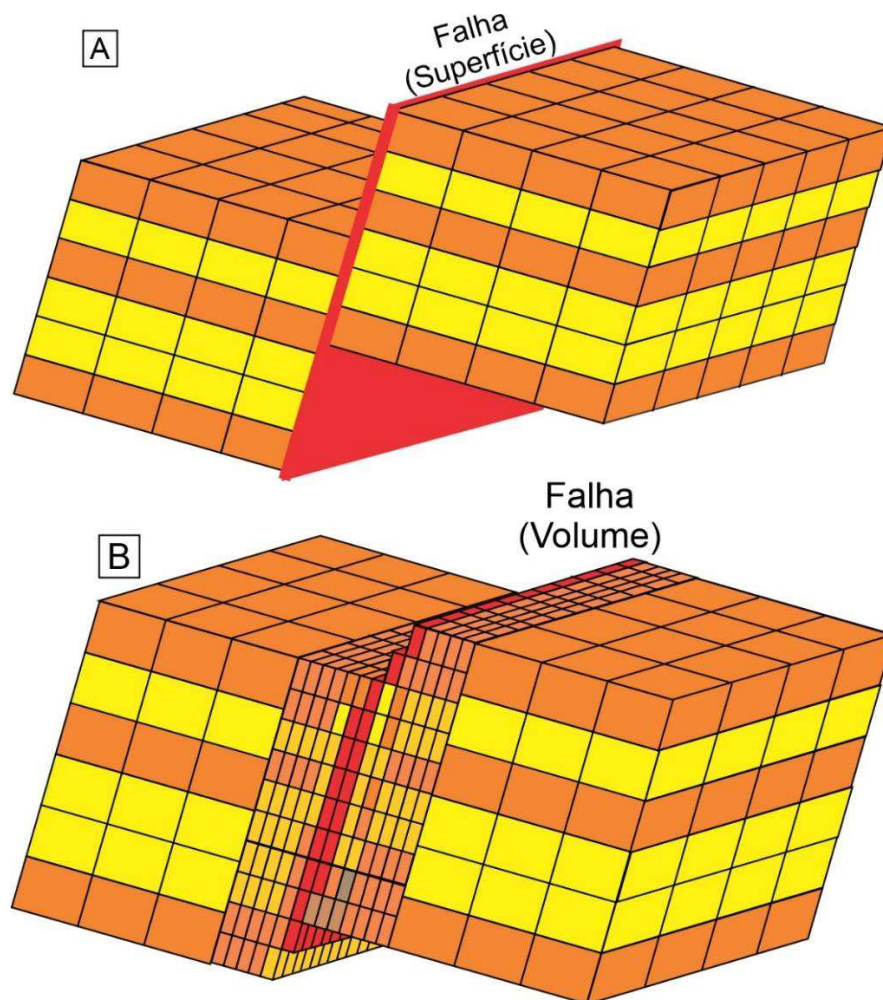
partir da distribuição e frequência das estruturas presentes no núcleo e nas zonas de dano, ou os volumes e proporções dessas estruturas e/ou rochas (e.g., Chesnaux et al., 2009; Qu e Tveranger, 2016; Fachri et al., 2016). De tal maneira, as permeabilidades equivalentes são calculadas a partir de médias ou modelos discretos de fraturas (*DFN – Discrete Fracture Networks*), que consideram a distribuição dos elementos das zonas de falha (e.g., Chesnaux et al., 2009; Fachri et al., 2013a).

### 3.3. Modelagem Geológica de Zonas de Falha

Até o início dos anos 90, a modelagem geológica de reservatórios naturalmente fraturados não incorporava as zonas de falha como volumes, mas sim, como planos com transmissibilidades distintas (Manzocchi et al., 1999; Tveranger et al., 2004, 2005) (Fig. 3.5). No entanto, a partir do conhecimento geológico dos componentes das zonas de falha (núcleo, zonas de dano e protólito) (Caine et al., 1996; Berg e Skar, 2005; Torabi et al., 2019a, 2019b) e de quão heterogêneas podem ser as propriedades petrofísicas dessas zonas (Braathen et al., 2009; Balsamo e Storti, 2010; Farrel et al., 2014) e a sua influência no fluxo de fluidos (e.g., Rotevatn e Fossen, 2011) esses volumes passaram a ser incorporados aos modelos convencionais de reservatórios, assim como suas heterogeneidades (e.g., Fachri et al., 2016).

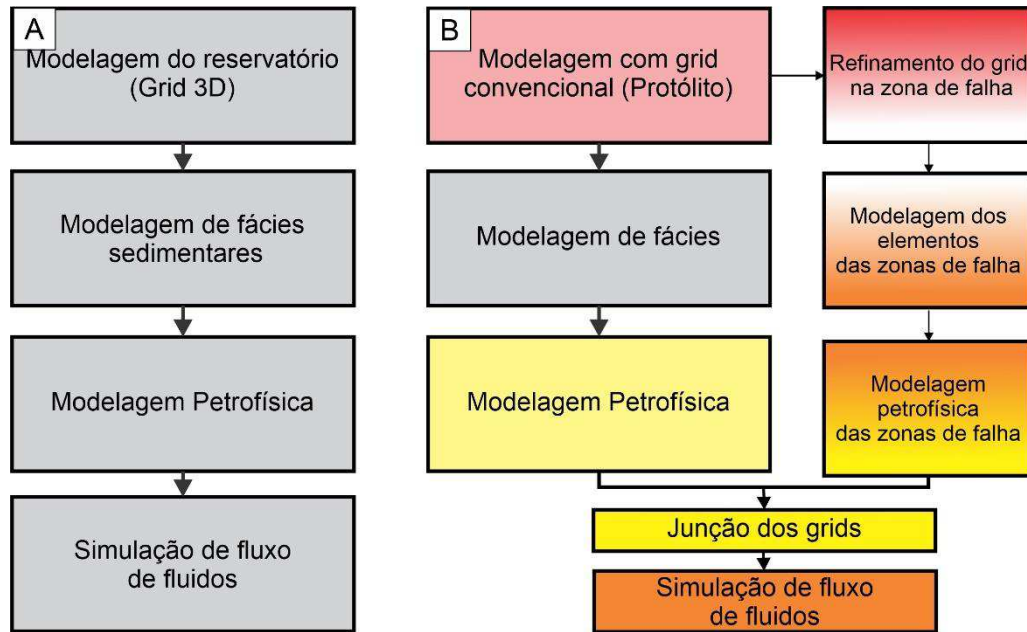
Novos *workflows* foram criados e/ou adaptados para a modelagem de reservatórios naturalmente fraturados (e.g., Syversveen et al., 2006; Qu et al., 2015) a partir dos *workflows* convencionais (e.g., Pyrcz et al., 2005), que somente (Fig. 3.6A): (1) delimitam as zonas de reservatório e com isso constroem o grid 3D; (2) modelam a distribuição de fácies sedimentares; (3) modelam as propriedades petrofísicas; e (4) incorporam esses modelos a simulação de fluxo. Essas adaptações fizeram com que os fluxogramas que incluem a modelagem de zonas de falha seguissem-se as seguintes etapas (Fig. 3.6B) (Syversveen et al., 2006): (1) modelagem com grid convencional; (2) modelagem de fácies de falha; (3) modelagem petrofísica; (4) refinamento

do grid na zona de falha (Fig. 3.5); (5) modelagem dos elementos das zonas de falha; (6) modelagem das propriedades petrofísicas das zonas de falha; (7) fusão ou junção dos grids; (8) incorporação dos modelos a simulação de fluxo.



**Fig. 3.5.** Modelos geológicos (Grid) que consideram as zonas de falhas como (A) superfícies e (B) como volumes. (Adaptada a partir de Tveranger et al. (2014))

Dois das etapas do *workflows* de modelagem das zonas de falha que mais se tem estudados são: (1) a geração de grids 3D refinados nas zonas de falha, tais que a heterogeneidade dessas zonas possa ser modelada de forma precisa a um baixo custo computacional (menor quantidade de células possíveis) (e.g., Fachri et al., 2016; Qu et al., 2015); e (2) a distribuição das rochas de falha e estruturas presentes nessas zonas (e.g., Fachri et al., 2013a, b).

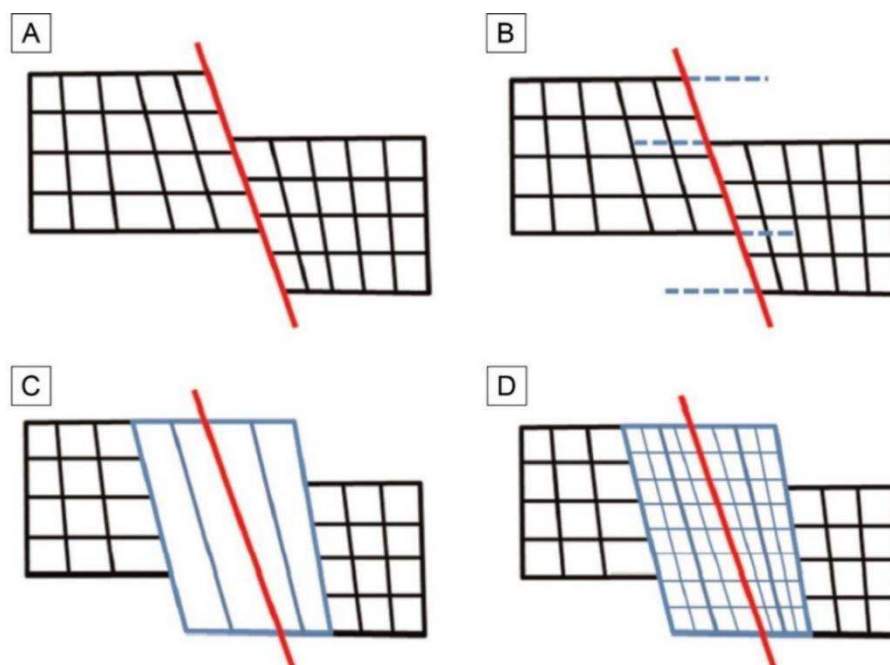


**Fig. 3.6.** Workflows (A) convencional e (B) adaptado para a modelagem de reservatórios com zonas de falha (adaptado a partir de Syversveen et al. 2006.)

Referindo-se a primeira etapa, Qu et al. (2015) propuseram um algoritmo que integram os grids das zonas de falhas (refinados) ao das regiões adjacentes a essas (rochas não deformadas), onde esses grids podem ser gerados de forma independente em *softwares* convencionais de modelagens de reservatórios (e.g., Petrel<sup>TM</sup>, RMS<sup>TM</sup>). No algoritmo sugerido por esses autores (Fig. 3.7), o modelo original (Fig. 3.7A, B) é rendido por um grid refinado (Fig. 3.7C) na zona de falha cujos limites foram previamente estabelecidos (Fig. 3.7A, B), suportando essas zonas outros refinamentos independentes das regiões adjacentes (Fig. 3.7D). Em adição, essa metodologia vem possibilitando a representação de diversas geometrias das zonas de falha (Fig. 3.8) e distribuição efetiva das propriedades dessas zonas (Fachri et al., 2016; Qu e Tveranger., 2016; Qu et al., 2017).

No que se refere a distribuição dos elementos das zonas de falha, o uso de fácies de falha é uma abordagem que vem se consolidando para a modelagem multiescalar de zonas de falha por fazer essa abordagem o uso de ferramentas disponíveis em *softwares* convencionais de

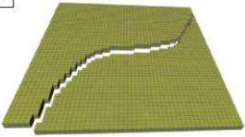
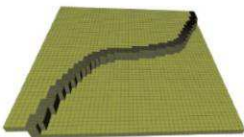


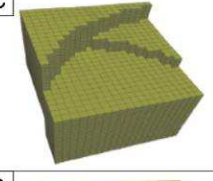
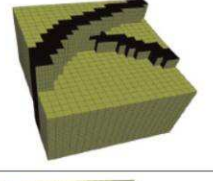
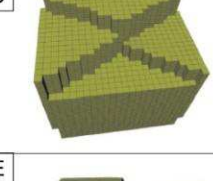
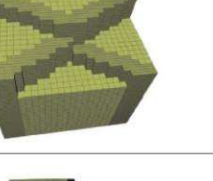
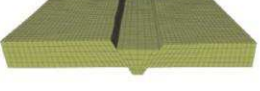
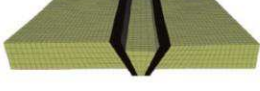

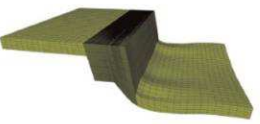
modelagem (e.g., Braathen et al., 2009; Fachri et al., 2011, 2013a, 2013b; Qu e Tveranger, 2016; Qu et al., 2017; Botter et al., 2017; Botter e Champion, 2019).



**Fig. 3.7.** *Workflow* usado por Qu et al. (2015) ilustrando o grid da zona de falha em (A) um corte transversal com a falha traçada, em (B) e (C) a base e o topo da zona de falha e em (D) somente o refinamento do grid nessa zona (retirado de Qu et al., 2015).

### 3.3.1. Modelagem de Fácies de Falha

A modelagem de fácies sedimentares é algo extremamente comum para o *workflow* de modelagem de reservatórios (e.g., Harding et al., 2005). Assim, fazendo o uso de conceito geral de fácies, que são corpos rochosos com propriedades específicas (Braathen et al., 2009 e suas referências). Tveranger et al. (2005) definiram fácies de falha como sendo corpos rochosos cujas propriedades são provenientes da deformação tectônica. De tal maneira, a modelagem das zonas de falha a partir de fácies de falha consegue aplicar todas as ferramentas e algorítmicos usados para modelagem de fácies sedimentares (e.g., Fachri et al., 2011), para a distribuição dos elementos dessas zonas quanto a sua ocorrência, tipo, posição, tamanho forma e outras propriedades (Braathen et al., 2009).

	Convencional	Com grid da zona de falha volumétrica	Informações do grid
A			<b>Número de células</b> Esquerda: 15.000 Direita: 126.000  <b>Resolução (X-Y)</b> Grid Global: 20 m x 20 m ZF: 2 m x 20 m
B			<b>Número de células</b> Esquerda: 42.000 Direita: 298.800  <b>Resolução (X-Y)</b> Grid Global: 10 m x 10 m ZF: 5 m x 20 m
C			<b>Número de células</b> Esquerda: 8.000 Direita: 188.000  <b>Resolução (X-Y)</b> Grid Global: 30 m x 30 m ZF: 1 m x 10 m
D			<b>Número de células</b> Esquerda: 11.250 Direita: 182.500  <b>Resolução (X-Y)</b> Grid Global: 20 m x 20 m ZF: 2 m x 10 m
E			<b>Número de células</b> Esquerda: 10.000 Direita: 170.000  <b>Resolução (X-Y)</b> Grid Global: 10 m x 10 m ZF: 0.1 m x 5 m
F			<b>Número de células</b> Esquerda: 6.000 Direita: 54.000  <b>Resolução (X-Y)</b> Grid Global: 10 m x 10 m ZF: 0.5 m x 5 m

**Fig. 3.8.** Aplicação do algoritmo de Qu et al. (2015) para o refinamento de grids em diversos tipos de zona de falha (ZF). (A) falha curva, (B) rampa de revezamento, (C) e (D) intersecção entre falhas, (E) falhas inclinadas e (F) falhas com *hangingwall drag-fold* (retirado de Qu et al. 2015).

A maior aplicação da modelagem de fácies de falha ainda se refere a distribuição de BD nas zonas de dano compostas por arenitos porosos (Fachri et al., 2013a, b; Qu e Tveranger, 2016; Qu et al., 2017). Essa abordagem possibilita a integração de dados da frequência dessas estruturas obtidos em escala de afloramento a partir de linhas de varreduras (*scanlines*), não somente para modelagem nessa escala (afloramentos), mas também para a modelagem em

escala de reservatórios (e.g., Qu e Tveranger, 2016; Qu et al., 2017). E assim, através da distribuição das BD ou fácies de falha das frequências de BD, entende-se como essas estruturas impactam na distribuição das propriedades petrofísicas das zonas de dano (e.g., Fachri et al., 2013a), e no fluxo de fluidos em meios porosos.

# *Capítulo. 4*

## *Resultados*

### *Permeability modeling of a basin-bounding fault damage zone in the Rio do Peixe Basin, Brazil.*

Artigo publicado na *Marine and Petroleum Geology (Elsevier Journal)*.

Artigo submetido em: 10 de Março de 2021

Artigo Publicado em: 27 de outubro de 2021



**Permeability modeling of a basin-bounding fault damage zone in the Rio do Peixe Basin,  
Brazil**

Silva, M. E.<sup>a \*</sup>, Nogueira, F.C.C.<sup>b</sup>, Pérez, Y.A.R.<sup>c</sup>, Vasconcelos, D.L.<sup>b</sup>, Stohler, R.C.<sup>d</sup>,  
Sanglard, J.C.D.<sup>d</sup>, Balsamo, F.<sup>e</sup>, Bezerra, F.H.R.<sup>c</sup>, Carvalho, B.R.B.M.<sup>d</sup>, Souza, J.A.B.<sup>d</sup>

<sup>a</sup> Post-Graduation Program in Petroleum and Mineral Exploration, Federal University of Campina Grande, Brazil

<sup>b</sup> Department of Petroleum Engineering, Federal University of Campina Grande, Brazil

<sup>c</sup> Department of Geology, Federal University of Rio Grande do Norte, Brazil

<sup>d</sup> Petrobras Research Center, Brazil

<sup>e</sup> Department of Chemistry, Life Science and Environmental Sustainability, University of Parma, Italy

\*Corresponding author

E-mail address: [maria.eduarda@uaepetro.ufcg.edu.br](mailto:maria.eduarda@uaepetro.ufcg.edu.br) (Silva, M.E.)

**Abstract**

In permeability modeling of fault damage zones affecting porous sandstones, deformation bands are commonly considered low-permeability structures that influence fluid flow. Permeability in damage zones of such rocks exhibits and is influenced by complex networks of deformation bands separated by volumes of seemingly undeformed host rock. This study used deformation band frequency data to delimit and model the fault damage zone boundaries and fault facies in the hanging wall of the Malta Fault segment in the Rio do Peixe Basin, Brazil.

We then integrate in situ permeability data collected in deformation bands and interband spaces (deformed host rock located between adjacent deformation bands) with damage zones and fault facies models to estimate the equivalent permeability perpendicular and parallel to the main fault. Our results indicated a logarithmic decrease in deformation band frequency towards the protolith with local variations controlled by minor faults in the damage zone. We identified three damage zone subdomains (inner and outer damage zones and transitional zone); which totalizing roughly 200 m of width. Permeabilities of the deformation bands and interband spaces increase towards the protolith non-uniformly due to the difference in deformation intensity. The deformation bands and interband spaces in the inner and outer damage zones, which comprise fault facies representing the highest deformation intensities, exhibit permeability reductions of 1–3 orders of magnitude compared to the undeformed rocks, whereas 0–2.5 orders of magnitude reductions were observed in the transitional zone between the damage zone and the protolith. This study provides new perspectives about the permeability in deformation bands and interband spaces by different subdomains of damage zones and fault facies. This information proved is essential for modeling equivalent permeabilities along damage zones and assessing its implications to siliciclastic reservoirs affected by fault zones, where deformation bands are pervasive.

**Keywords:** Fault Zone; Damage Zone; Deformation bands; Fault facies; Equivalent permeability; Permeability modeling; Siliciclastic reservoirs.

## 1. Introduction

A widely accepted practice in reservoir simulation involves assigning transmissibility multipliers to cell connections/boundaries to represent hydraulic behavior of fault surfaces in

geological models (Manzocchi et al., 1999; Tveranger et al., 2004; Shipton et al., 2005; Qu et al., 2017). However, faulting is frequently associated with formation of deformed zones with very heterogeneous properties compared to the undeformed rocks (Caine et al., 1996; Braathen et al., 2009; Faulkner et al., 2010; Choi et al., 2016). In this context, fault zones might encompass two distinct architectural elements, a fault core and a surrounding damage zone (Fig. 1A) (Caine et al., 1996; Choi et al., 2016; Balsamo et al., 2019; Celestino et al., 2020). The fault accommodates the bulk of displacement and deformation intensity and may contain cataclasites, gouges, breccias, slip surfaces, chemically altered rocks, among other features (Micarelli et al., 2003; Wibberley et al., 2007; Braathen et al., 2009; Childs et al., 2009; Torabi et al., 2019). The damage zone comprises subsidiary structures such as minor faults, deformation bands, and joints (Fig. 1A) (Berg and Skar, 2005; Rotevatn et al., 2009; Faulkner et al., 2010; Torabi and Berg, 2011; Torabi et al., 2020a), where the frequency of these structures tends to decrease from the fault core toward the protolith (Fig. 1B) (e.g., Schueller et al., 2013; Fossen et al., 2017; Balsamo et al., 2019). In the protolith, the frequency of these subsidiary structures termed as background frequency, usually equaling to one or two structures per meter, which may not be directly linked to faulting, but to pre-existing deformation (Choi et al., 2016 and references therein; Torabi et al., 2020a).

Several studies have addressed the importance of determining the structural elements of damage zones and their properties, particularly in porous rocks, where cataclastic deformation bands can be pervasive (e.g., Torabi et al., 2013; Fachri et al., 2013a, 2013b; Qu and Tveranger, 2016; Torabi et al., 2020a). Cataclastic deformation bands are subseismic, millimeter to centimeters thick tabular structures with high matrix content due to grain-size reduction associated with the cataclasis (Fossen et al., 2007, 2017 and references therein). Deformation bands normally show reduced petrophysical properties compared to their host rock (e.g.,

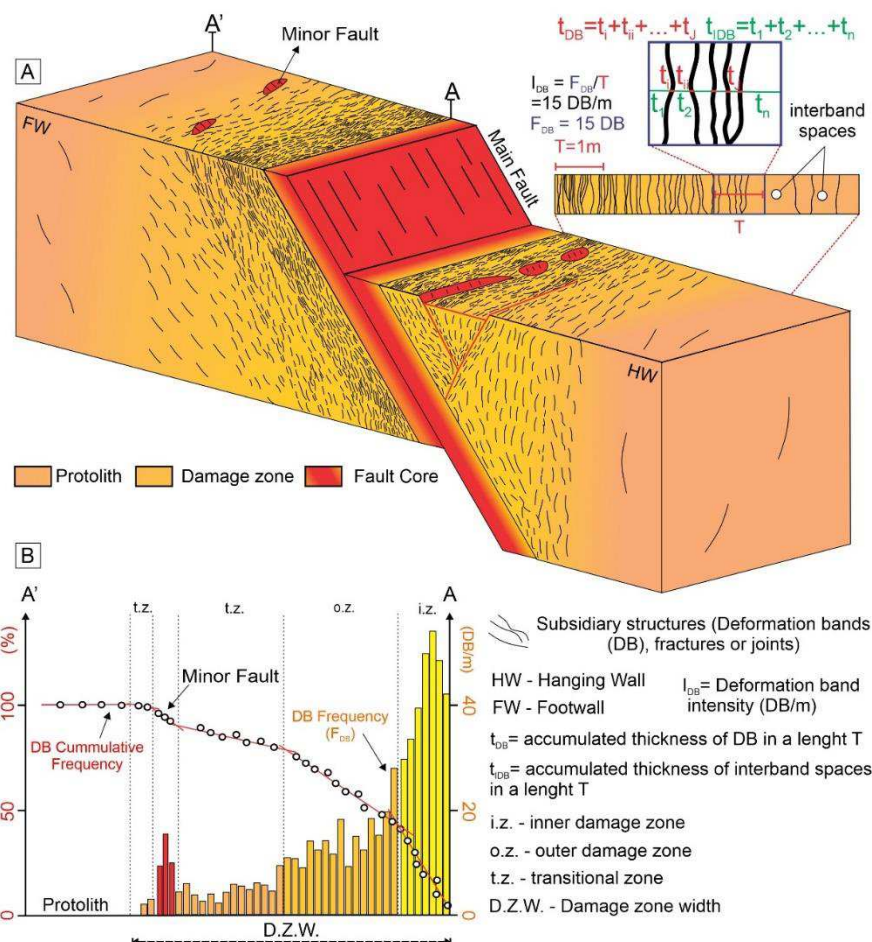
Antonellini and Aydin, 1994; Torabi et al., 2013; Ballas et al., 2015; Nogueira et al., 2021) and increased mechanical properties such as Uniaxial Compressive Strength (UCS) (e.g., Pontes et al., 2019; Del Sole et al., 2020) compared to undeformed rocks. Thus, there has been a growing interest in understanding and capturing damage zone property distribution in the subsurface, especially with respect to reservoir models, where two main challenges have formed the focus of attention: The first involves the delimitation of the damage zone boundaries, including the definition of subdomains known as inner and outer damage zones (Choi et al., 2016; Torabi et al., 2020a) and the transitional zone (Berg and Skar, 2005) (Fig. 1B). In this context, several studies have used the cumulative frequency of structures present in fault damage zones, from fault core to protolith, and some internal fault properties to provide an approximation of internal fault subdomains (inner and outer damage zones and transitional zone) (Fig. 1B) (e.g., Berg and Skar, 2005; Choi et al., 2016; Araújo et al., 2018; Torabi et al., 2020a; Pizzati et al., 2020). This information has also been used to obtain predictive relationships for constraining these boundaries in the subsurface (e.g., Schueller et al., 2013; Choi et al., 2016; Alaei and Torabi, 2017; Ma et al., 2019; Torabi et al., 2020a). The second challenge relates to subsurface constraints to data-acquisition. Distribution of the subsidiary structures and variation in the damage zones properties are commonly not resolvable using standard seismic processing methods at the reservoir scale (Maerten et al., 2006; Botter et al., 2016b; Fossen et al., 2017). Shortcomings to acquisition can occur even at well-log scale, where image logs often fail to detect structural features such as deformation bands and fractures. However, subsurface distribution of damage zone elements and their properties can be approximated and modeled at reservoir scale using outcrop based methods such as fault facies (e.g., Braathen et al., 2009; Fachri et al., 2011, 2013a, 2013b; Qu and Tveranger, 2016; Qu et al., 2017; Botter et al., 2017; Botter and Champion, 2019). These fault facies are defined as rocky bodies whose properties arise from tectonic deformation (Tveranger et al., 2004, 2005; Braathen et al., 2009). As fault

facies can be defined and adapted on a fit-for-purpose base, they allow the modeling of several properties of fault zones regardless of scales (Braathen et al., 2009).

Several recent studies have employed the fault facies concept to model damage zone volume, spatial distribution of deformation bands and deformation intensity (deformation bands/m or DB's/m) (Fig. 1A) (Fachri et al., 2013a, 2013b; Qu and Tveranger, 2016; Qu et al., 2017). However, few studies have characterized the permeability in deformation bands and the interband spaces (Fig. 1A) (i.e., the relatively undeformed host rock, cf. Nogueira et al., 2021) along damage zones subdomains (e.g., inner and outer damage zone) (e.g., Sorkhabi and Hasegawa, 2005; Pizzati et al., 2020). This issue is fundamental for understanding the reservoir connectivity, hydrocarbon recovery, break-through time, and fluid flow complexity in porous media, associated with permeability contrast between deformation bands, interband spaces, and host rock (Rotevatn et al., 2009; Rotevatn and Fossen, 2011; Fachri et al., 2013a, 2013b; Qu and Tveranger, 2016). Therefore, some questions are not yet fully clarified and present some uncertainties, such as: (1) how does deformation band intensity vary in each subdomain of the hanging wall damage zone towards the protolith? (2) Does the permeability of deformation bands and interband spaces change with the deformation intensity? (3) Is the interband permeability a critical parameter for quantifying and modeling the equivalent permeability of the damage zones, parallel and perpendicular to the main fault? (4) How does equivalent permeability vary between different damage zone subdomains?

In this context, the porous sandstones exposed along the Malta bounding fault in the Rio do Peixe Basin (RPB), Brazil (Fig. 4.2), represent a place well-suited to investigate and propose solutions to the questions raised above. This study describes and models the hanging wall fault damage zone and the distribution of the deformation band intensity using fault facies modeling. First, we used deformation band cumulative frequency to delimit and model the boundaries of

the damage zone subdomains and the frequency data to define the fault facies (Fig. 1B). Then, we employed in situ permeability data, collected from deformation bands and interband spaces, to populate damage zone subdomains and fault facies with permeability values.. Our results indicate that the deformation intensity controls the permeability distribution in damage zone subdomains so that in the most deformed subdomains the permeabilities of deformation bands and interband spaces exhibit a reduction of similar magnitude when compared to the undeformed rocks. These results have many implications for the equivalent permeabilities calculation and modeling, especially for the fault parallel permeability tensor, along damage zones where deformation bands are the dominant brittle structures.



**Fig. 4.1.** (A) Model

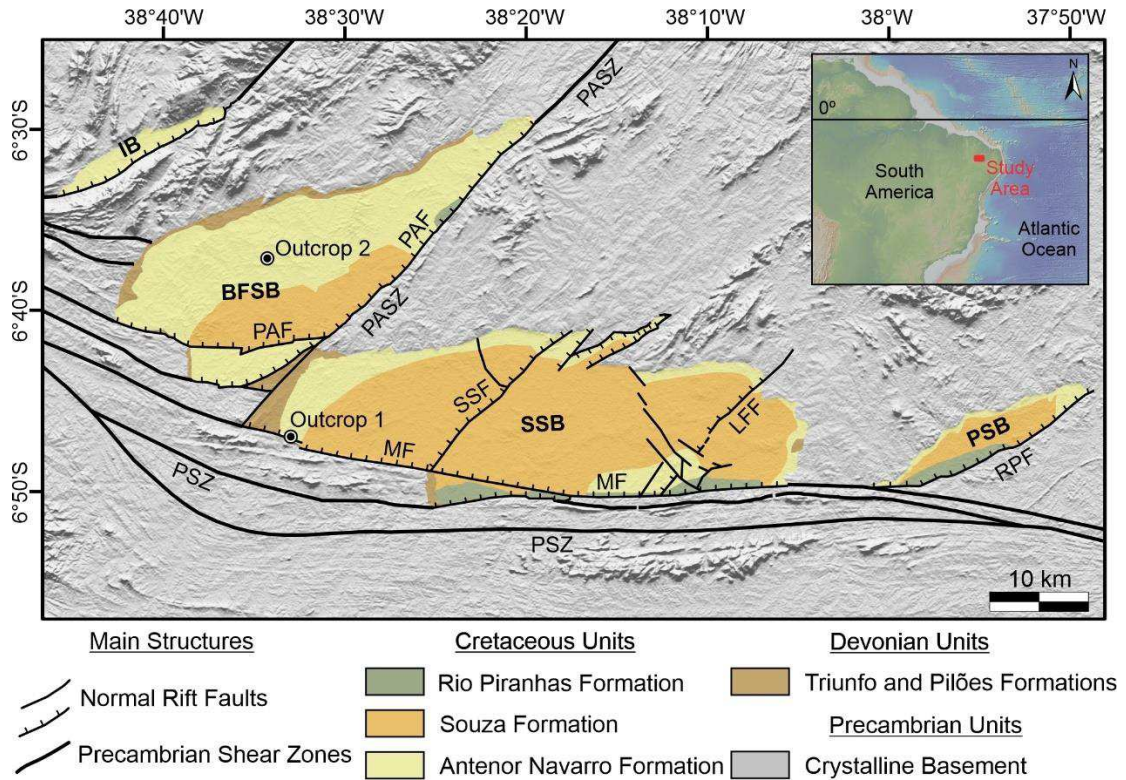
of a normal fault zone with its main elements subdivided according to Caine et al. (1996) in

fault core, damage zones, and protolith. In the damage zone, the black lines represent the deformation bands, which tend to be more frequent near the fault core. Minor faults, represented here by segments in red, can also develop in the damage zone. The interband space (the adjacent region between two deformation bands) is also represented, as well as how the intensity of deformation bands (IDB) in a length  $T$  (DB/m) is calculated (more details are presented in the methods section). The accumulated thickness of deformation bands ( $t_{DB}$ ) and interband spaces ( $t_{IDB}$ ) is detailed. (B) Graph of deformation bands cumulative frequency and deformation band frequency (FDB) along of the footwall damage zone (A-A') used for delimitation of the damage zone subdomains (Inner and outer damage zones and transitional zone) and damage zone width (DZW). Adapted from Berg and Skar (2005), Choi et al. (2016), and Torabi et al. (2020a).

## 2. Geological Setting

The RPB (Fig. 4.2) is a medium-sized intracontinental basin located in northeastern Brazil. This basin was formed in the Early Cretaceous (145 to 130 Ma) during the Pangea fragmentation, under an NW- to NNW-oriented extension that triggered a regional rifting process (Sénant and Popoff, 1991; Matos, 1992; de Castro et al., 2007; Nogueira et al., 2015). Subsequently, a change in the stress field in the RPB, involving the shift of the maximum compressive stress from vertical to horizontal, induced by far-field compressive stresses from the opposite pushes of the Mid-Atlantic Ridge and the Andes, triggered tectonic inversion from the Late Cretaceous (ca. 80 Ma) to present day (Nogueira et al., 2015; Vasconcelos et al., 2021). Rift development was controlled by brittle reactivations of the Precambrian E-W-striking Patos and NE-SW-striking Portalegre shear zones (Sénant and Popoff, 1991; de Castro et al., 2007; Nogueira et al., 2015). These shear zones acted as weakness zones that controlled the location and geometry of bounding faults of the RPB (Portalegre, Malta, and Rio Piranhas faults, respectively PAF, MF, and RPF in Fig. 4.2). Furthermore, these faults also control the main

depocenters in the RPB, resulting in the development of three sub-basins with half-grabens: (1) Brejo das Freiras (BFSB), (2) Sousa (SSB), and (3) Pombal (PSB) (Sénant and Popoff, 1991; de Castro et al., 2007) (Fig. 4.2).



**Fig. 4.2.** The geological map of the RPB with the outcrop locations representing the fault zone (outcrop 1) and the undeformed rocks (outcrop 2). The main structures and geologic units are based on Sénant and Popoff (1991), Medeiros et al. (2005), and Vasconcelos et al. (2021). Key – Shear Zones: PSZ – Patos; PASZ – Portalegre. Faults: MF – Malta; PAF – Portalegre; RPF – Rio Piranha; SSF – Sítio Sagui; LFF – Lagoa do Forno. Basin and sub-basins: IB – Icozinho; BFSB – Brejo das Freiras; SSB – Sousa; PSB – Pombal.

The sedimentary fill of the RPB comprises rocks of the Rio do Peixe Group (Early Cretaceous) deposited unconformably over rocks of the Santa Helena Group (Early Devonian), which overlie the crystalline rocks of the Precambrian basement (Carvalho et al., 2013; Silva et al., 2014). The stratigraphic units, from base to top, are the following: (1) Pilões Formation



(Early Devonian), predominantly composed of siltstones and shales, associated with deltaic to fluvial-deltaic depositional environments; (2) Triunfo Formation (Early Devonian), mainly consisting of fluvial–deltaic white to grey sandstones and conglomerates; (3) Antenor Navarro Formation (Early Cretaceous) composed of fluvial fine to conglomeratic sandstones and conglomerates; (4) Sousa Formation (Early Cretaceous) dominated by lacustrine, comprising intercalations of shales and siltstone; (5) Rio Piranhas Formation (Early Cretaceous) mainly composed of conglomerates, with feldspar and lithic fragments, associated with alluvial fans.

The most frequent deformational element in the fine to conglomeratic sandstones of the Antenor Navarro Formation are cataclastic deformation bands, whose structural, compositional, petrophysical, and geomechanics aspects have been addressed previously (Nogueira et al., 2015, 2021; Araújo et al., 2018; Maciel et al., 2018; Nicchio et al., 2018; Pontes et al., 2019; de Souza et al. 2021). For instance, Nicchio et al. (2018) pointed out that the processes of reducing grain sizes, rotating grains, and grain border comminuting during cataclasis result in slip zones with high degrees of comminution, composed of preferential alignment of feldspar fragments along these slip zones. Maciel et al. (2018) also analyzed the cataclastic processes and how porosity reduction is associated with the development of cataclastic fabric within the deformation bands, preventing fluid-rock interaction, reducing feldspars wear, and inhibiting autogenesis of clays. In addition, Araújo et al. (2018) suggested a logarithmic decay in the deformation band frequency as they move away from the basin-bounding faults and control grain size in the deformation band clusters. Pontes et al. (2019) addressed the mechanical behavior of deformation bands and observed that uniaxial compressive strength (UCS) in fault zones is four times higher than those in undeformed units. de Souza et al. (2021) showed that cataclastic bands grow into a fault zone through a multiscalar process of microcrack coalescence and deformation band linkage. Finally, Nogueira et al. (2021) characterized a

progressive decrease in porosity and permeability and reduced pore diameter with an increased generation of the cataclastic matrix related to the intensity of cataclasis.

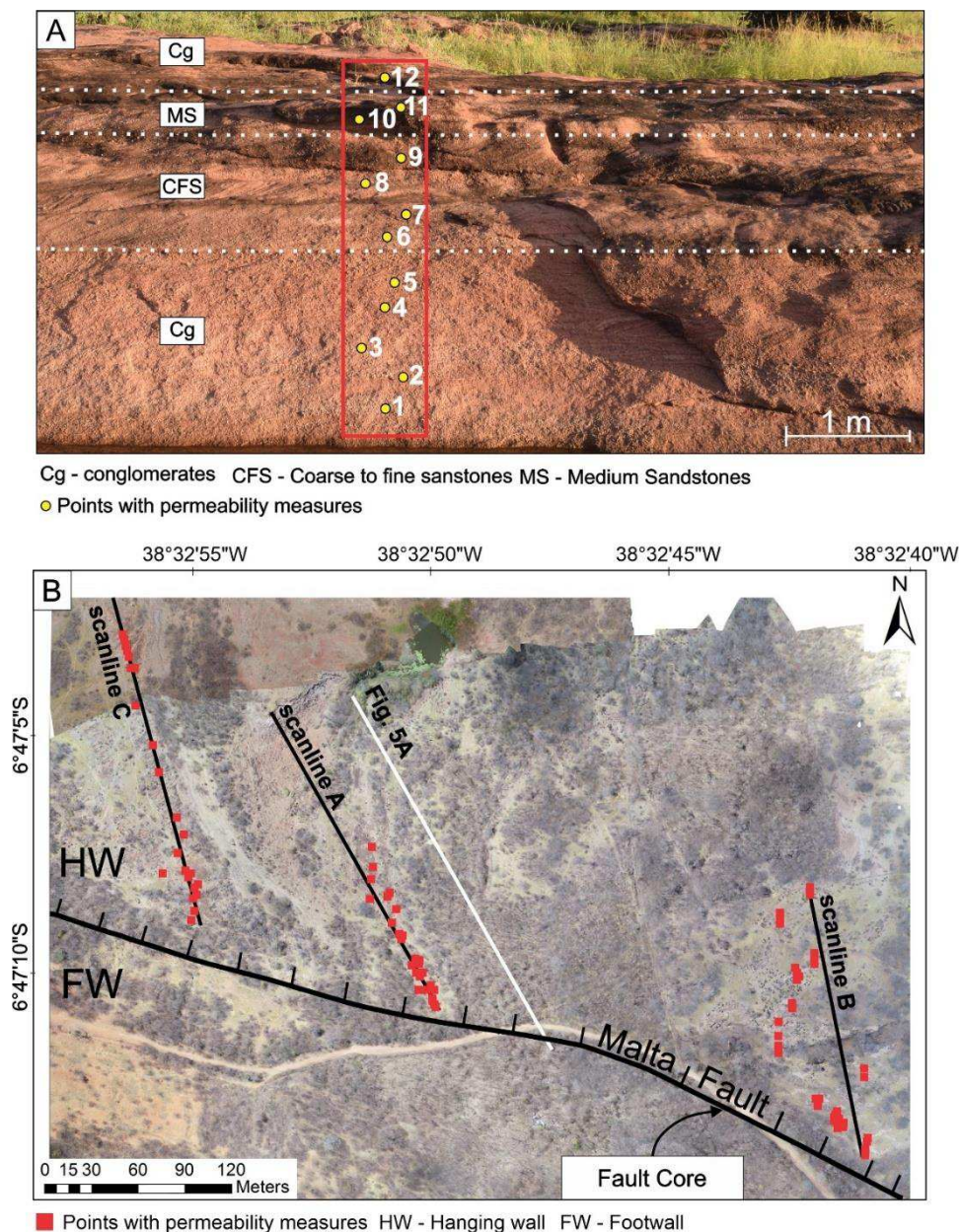
### 3. Methods

We investigated two outcrops in the RPB (Fig. 4.2). The first outcrop (1 in Fig. 4.2) corresponds to the Malta Fault Zone and the second (2 in Fig. 4.2) to undeformed rocks of the Antenor Navarro Formation. Outcrop 1 encompasses the Malta Fault western segment located in the SSB. This fault zone is composed of a footwall with fractured mylonites of the crystalline basement and a hanging wall mainly made up of fine to conglomeratic sandstones of the Antenor Navarro Formation with deformation bands. Outcrop 2 (Fig. 4.2) is located in the middle of the BFSB. It comprises undeformed rocks composed of poorly sorted sandstones, silty sandstones, conglomerates, coarse sandstones, and clay lenses of the same formation (Fig. 4.3A). Being exposed from any major fault, outcrop 2 was chosen in this work to represent the intact siliciclastic sequence which was used as a reference to compare structural and petrophysical properties in deformed and undeformed states.

#### 3.1. *Measurements of deformation features*

We analyzed the deformational features only in the conglomeratic to fine sandstones of the Antenor Navarro Formation in the hanging wall of the Malta Fault Zone (Fig. 4.3B). To characterize this hanging wall fault damage zone, we reprocessed the structural data acquired by Araújo et al. (2018) along the SL1 linear scanline (scanline A in Fig. 4.3B). We collected new structural data along two other linear scanlines (scanlines B and C in Fig. 4.3B), totaling all scanlines a length of 599 m. Then, we analyzed the following parameters: (a) orientation and (b) thickness of the deformation bands (Ortega et al., 2006); (c) deformation band spacing;

and (d) deformation band frequency (F) per unit length, characterizing the deformation band intensity or just deformation intensity ( $I_{DB}$ ) (Fig. 4.1A) (Dershowitz and Herda, 1992). Although the linear scanlines are oblique to the strike of the main fault (Fig. 4.3B), the deformation bands spacing (distance between two adjacent or subparallel deformation bands, Fig. 4.1A) along the scanlines was measured orthogonally to their strike (true spacing).

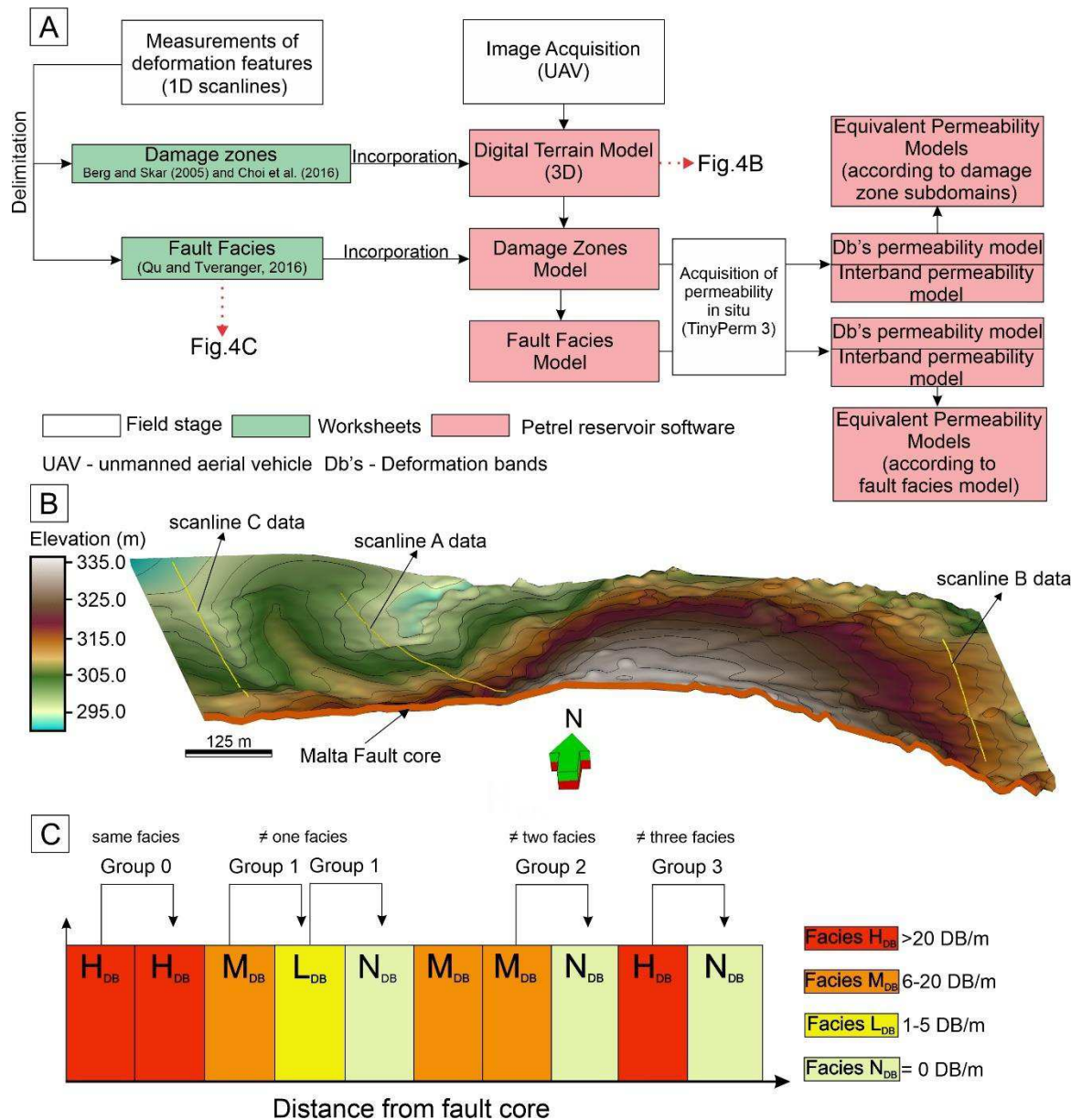


**Fig. 4.3. (A)**

Detail of the undeformed sedimentary unit in outcrop 2 with its sedimentary facies represented by the Cg, CFS, and MS. The yellow circles are the point location of permeability



measurements. (B) Unmanned Aerial Vehicle image from outcrop 1. The continuous black lines are the scanlines A, B, and C on the fault hanging wall. The solid white line represents the outcrop geological profile (Fig. 4.5A). The red squares are the points of permeability measurements.



**Fig. 4.4.** (A) Simplified workflow used in this study. (B) Digital model of outcrop 1, and location of the deformation band intensity data acquired along scanlines A, B, and C. Vertical exaggeration of 1.5x. (C) Spatial Relationship Classes between the facies H<sub>DB</sub> (High

deformation band intensity),  $M_{DB}$  (Medium deformation band intensity),  $L_{DB}$  (Low deformation band intensity), and  $N_{DB}$  (No deformation bands) (adapted from Qu and Tveranger, 2016).

### 3.2. Constraining and modeling the damage zone

The workflow designed to carry out the analyses and modeling is illustrated in Fig. 4.4. Initially, based on the deformation band frequency along the scanlines, we determine on the hanging wall the damage zone widths and its subdomains (Fig. 4.4A). The protolith in this study is defined as a region adjacent to the damage zone with a background frequency less than or equal to 1 DB/m. The boundaries of the damage zone subdomains were defined at the changes/inflections of slopes in the curve that correlates the deformation band cumulative frequency with the distance from the fault core (Fig. 1B) (e.g., Berg and Skar, 2005; Choi et al., 2016; Torabi et al., 2020a). According to Berg and Skar (2005), this curve presents normally (a) a steeper slope for the inner damage zone, (b) a non-linear pattern in the outer damage zone, (c) a low slope in the transitional zone, and (d) a constant flat curve in the protolith. Due to the gaps along the scanlines, we applied the correction proposed by Choi et al. (2016) on scanlines B and C, which is equivalent to using in sections without data (gaps) the slope gradient around them. The three scanlines used in this work were spaced hundreds of meters along the Malta Fault segment strike to analyze the damage zone subdomains width (Fig. 4.3B).

To perform the modeling of the hanging wall fault damage zone, here called damage zone subdomains model or damage zone model, we first built the outcrop 1 model. We made a 3D grid using the topographic data obtained through Unmanned Aerial Vehicle (UAV) imagery in the Schlumberger Petrel™ software (Fig. 4.4B). Then, the whole Malta Fault segment (Fig. 4.4B), which mainly represents the fault core, was incorporated into our 3D model. This segment's geometry and location were based on previous works (e.g., Nogueira et al., 2015; Araújo et al., 2018). Finally, we used the damage zone width acquired in each scanline to obtain

the damage zone subdomains model at the outcrop scale. We performed a linear interpolation of these widths in the areas between the scanlines to build the damage zone model. This model comprises a grid with 399 m x 548 m x 3 m (X, Y, Z), with a resolution of 1 m x 1 m x 1 m (I, J, K), totaling 655,956 cells. The choice of 3 m in the Z direction was associated with the outcrop mean vertical exposures.

### 3.3. Fault facies analysis and modeling

The deformation intensity data were discretized (deformation bands/m) in four groups, corresponding to different fault facies (Fig. 4.4A). These fault facies were defined by Qu and Tveranger (2016) as "High", "Medium", "Low", and "None" based on the number of deformation bands per meter (DB/m):  $H_{DB}$  (>20 DB/m),  $M_{DB}$  (6-20 DB/m),  $L_{DB}$  (1-5 DB/m), and  $N_{DB}$  (0 DB/m). After delimiting the fault facies, we analyzed each fault facies proportion ( $H_{DB}$ ,  $M_{DB}$ ,  $L_{DB}$ , and  $N_{DB}$ ) in all damage zone subdomains and the protolith. We also analyzed the spatial relationship between these four fault facies in each meter (Fig. 4.4C) and their continuity (perpendicular to the Malta Fault core) in each damage zone subdomain. When two consecutive one-meter segments contain the same facies, their relationship equals zero (0), i.e., there is a continuity of fault facies (Fig. 4.4C). In contrast, when there is a change of fault facies in two neighboring one-meter intervals, we analyzed this intensity variation (Fig. 4.4C). For example, for a fault facies change of  $H_{DB}$  to  $M_{DB}$ ,  $M_{DB}$  to  $L_{DB}$ , and  $L_{DB}$  to  $N_{DB}$ , these correspond to groups one (1),  $H_{DB}$  to  $L_{DB}$  and  $M_{DB}$  to  $N_{DB}$  to group two (2), and  $H_{DB}$  to  $N_{DB}$  to group three (3).

We integrated (upscaled) the fault facies data (scanline data in Fig. 4.4B) into the damage zone model (Fig. 4.4A). Besides, we populated these fault facies in the model cells (Fig. 4.3A) using the Truncated Gaussian Simulation (TGS) algorithm (Journel and Isaaks, 1984; Matheron et al., 1987). The TGS algorithm was used to model fault facies because, according to Fachri et

al. (2013a, 2013b) this can represent in detail brittle structures/deformation present in fault damage zones honoring specifically ordered transitions between facies and prior facies proportions. Therefore, these are important aspects to model deformation band distribution using fault facies (e.g., Fachri et al., 2013a; Qu and Tveranger, 2016). Thus, we build our fault facies model using the (1) fault facies data (scanline data), (2) fault facies proportion trends of each damage zone subdomain, (3) fault facies spatial order, and (4) spherical variograms with anisotropy ranges (Table 1), which represent the fault facies continuity and geometry. The variogram range value assigned to the minor (x) orientation was the fault facies continuity of each damage zone subdomain, obtained from scanline data (Table 1). For major (y) orientation, we used the variogram range value equal to the maximum lateral distance between the scanlines (Table 1). Furthermore, the vertical variogram range value (Z) was established as 3 m (Table 1), considering that the fault facies do not vary in this direction throughout the model.

Finally, we correlated the deformation intensity (DB/m) with the distance from the fault core for each fault facies, using logarithmic fits. These logarithmic fits or equations were used to generate a continuous deformation intensity (DB/m) model (calculated) from the discrete fault facies model. This continuous model aimed to represent the variation in deformation intensity (DB/m) with the distance from the fault core of each fault facies and thus enables a more accurate calculation of the equivalent permeability.

**Table 1**

Variogram parameters for modeling fault facies and equivalent permeabilities.

Parameters	Fault facies modeling	Permeability modeling of the deformation bands, interband space, and equivalents (x and y directions)
Azimuth direction	ENE-WSW (Mean = - 074) – parallel to the fault and main direction of deformation bands	
Minor range perpendicular to the main fault (m)	According to the lateral continuity of the fault facies in each damage zone subdomain (Fig. 4.9)	5
Major range parallel to the main fault (m)	350	175
Vertical range (m)	3	3

**Table 2**

General Characteristics of scanlines.

Scanline	Scanline Direction	Distance from fault core to the scanline outset (m)	Scanline Length (m)	Number of deformation bands
Scanline A	NNW-SSE (330°)	0	216	1136
Scanline B	NNW-SSE (349°)	17	166	649
Scanline C	NNW-SSE (345°)	23	217	666

### 3.4. Permeability modeling

We performed in situ permeability measurements across the fault zone and protolith (Fig. 4.3A) using a portable air minipermeameter (TinyPerm 3 – New England Research, Inc.), which provides reliable permeability values in the range from  $10^{-3}$  up to 10 Darcy. These permeabilities were measured in the deformation bands ( $K_{DB}$ ) and interband spaces ( $K_{IDB}$ ) in



each damage zone subdomains and fault facies. All measurements were parallel to deformation bands dip, which are vertical to sub-vertical (Fig. 4.5). The measurements were vertical/perpendicular to the outcrop pavement in the interband spaces, which corresponds to the same direction as the deformation band measurements. In addition, the measured surface was polished before the acquisition of permeability data to remove a thin thickness of weathered rock. We also carefully remove all particulate matter generated by polishing the surface, to prevent this material to not interfere with the results.

To characterize the permeabilities of the geological model of damage zones, we made multiple measurements of the same direction (~3 at each point) at 141 points along the scanlines (red squares in Fig. 4.3B) and used the average of each point. Of these 141 points (448 measurements), 123 were in the damage zone subdomains, and the remaining 18 points were in the protolith. Likewise, we used these same measurements to analyze the permeability on each fault facies (H<sub>DB</sub>, M<sub>DB</sub>, L<sub>DB</sub>, N<sub>DB</sub>). We also acquired multiple permeability measurements (~7 at each point) in the horizontal direction (perpendicular to the section) (Fig. 4.3A) at 12 points (87 measurements) in undeformed rocks or outcrop 2 (K<sub>UR</sub>) and used the average of each point. These measurements were made (Fig. 4.3A) several km away from any fault zone (outcrop 2 in Fig. 4.2) to compare the permeability in undeformed rocks and deformed zones besides the protolith (as background deformation) adjacent to these. As measurements were taken in different directions on outcrops 1 (vertical) and 2 (horizontal), we used a linear correlation  $K-V = (0.7903 * K-H) + 3.431$  ( $R^2=0.8685$ ) obtained from data in sandstones by Shedid (2019) to estimate the vertical permeability (K–V) from the horizontal permeability (K–H) measured at outcrop 2. It was only then possible to compare the hanging wall damage zone permeabilities (Outcrop 1 in Fig. 4.2) with those of undeformed rocks (Outcrop 2 in Fig. 4.2). Although permeability measurements were made and estimated along the entire section in outcrop 2 (Fig.

4.3A), we compared  $K_{DB}$  and  $K_{IDB}$  measurements (outcrop 1) only with those of coarse to fine sandstones (points 5-8 in Fig. 4.3A) because it is the predominant lithology in outcrop 1.

The permeability data were then processed to obtain the average values representing the deformation bands ( $K_{DB}$ ) and the interband spaces ( $K_{IDB}$ ) for each damage zone subdomain and fault facies. We upscaled/integrated the deformation band permeability data ( $K_{DB}$ ) into the models of damage zones and fault facies, and we modeled this property using the Sequential Gaussian Simulation (SGS) algorithm (Deutsch and Journel, 1998). Similarly, we upscaled and modeled the interband space permeability ( $K_{IDB}$ ) according to the damage zone subdomains and fault facies using the same algorithm (SGS). We used a conditioner for the  $K_{DB}$  and  $K_{IDB}$  modeling according to the damage zones subdomains, the limits of these subdomains, and trends models based on the correlations between the  $K_{DB}$  and  $K_{IDB}$  with distance from the fault core. For modeling the  $K_{DB}$  and  $K_{IDB}$  conditioned to the fault facies, we used the distance from the fault core as a trend. We also used spherical variograms with anisotropic ranges and the same variogram direction to model the fault facies (Table 1). In addition, the variogram ranges applied in all  $K_{DB}$  and  $K_{IDB}$  models were the same, whose values were 5 m in the direction perpendicular to the main fault (X), 175 m in the direction parallel to the main fault (Y), and 3 m in the vertical direction (Z) (Table 1). The anisotropic range value was defined in the vertical direction based on the outcrop model thickness.

Finally, we calculated directly on the 3D grid (outcrop model) the equivalent permeabilities perpendicular ( $K_{EQ(x)}$ ) and parallel ( $K_{EQ(y)}$ ) to the main fault using harmonic (Equation 1) and arithmetic mean (Equation 2) (Cardwell and Parsons, 1945; Fachri et al., 2013a), respectively. Regarding the input parameters to the calculation of equivalent permeabilities (X and Y directions) conditioned to the damage zone subdomains and fault facies: (1) we applied the  $K_{DB}$  and  $K_{IDB}$  models obtained according to analyzes of these

subdomains and facies; (2) we calculated the accumulated thickness of deformation bands ( $t_{DB}$ ) along the 3D grid using Equation 3; (3) deformation band intensity ( $I_{DB}$ ) was obtained through models of the correlations of the deformation band frequency ( $F$ ) with the distance from the fault core along all damage zone subdomains and to each fault facies. Thus, we obtained a distribution model of the equivalent permeability conditioned to both damage zone subdomains and fault facies, parallel and perpendicular to the main fault. The equivalent permeability calculation along the grid was simplified, considering that all deformation bands follow the average orientation value of  $\sim 70^\circ$  (Figs. 4A and 8C). Deformation bands show orientation variations of up to  $30^\circ$  compared to the average value ( $\sim 70^\circ$ ).

$$\text{Equation 1} \quad K_{EQ(x)} = \left( \frac{\sum_{i=1}^n t_i / k_i}{\sum_{i=1}^n t_i} \right)^{-1} = \frac{T}{\frac{t_{DB}}{K_{DB}} + \frac{t_{IDB}}{K_{IDB}}}$$

$$\text{Equation 2} \quad K_{EQ(y)} = \left( \frac{\sum_{i=1}^n t_i k_i}{\sum_{i=1}^n t_i} \right) = \frac{k_{DB} t_{DB} + k_{IDB} t_{IDB}}{T}$$

where  $K_{EQ(x)}$  (mD) is the equivalent permeability perpendicular to the main fault (in the X direction), and  $K_{EQ(y)}$  (mD) is the equivalent permeability parallel to the main fault (in the Y direction) over a distance  $T$  (m), which corresponds to the model cell length (1 m in this study);  $K_{DB}$  (mD) and  $K_{IDB}$  (mD) are the permeabilities of the deformation bands and interband spaces; and  $t_{DB}$  (m) and  $t_{IDB}$  (m) are the accumulated thickness of the deformation bands and interband spaces in a  $T$  length (Fig 4.1A).

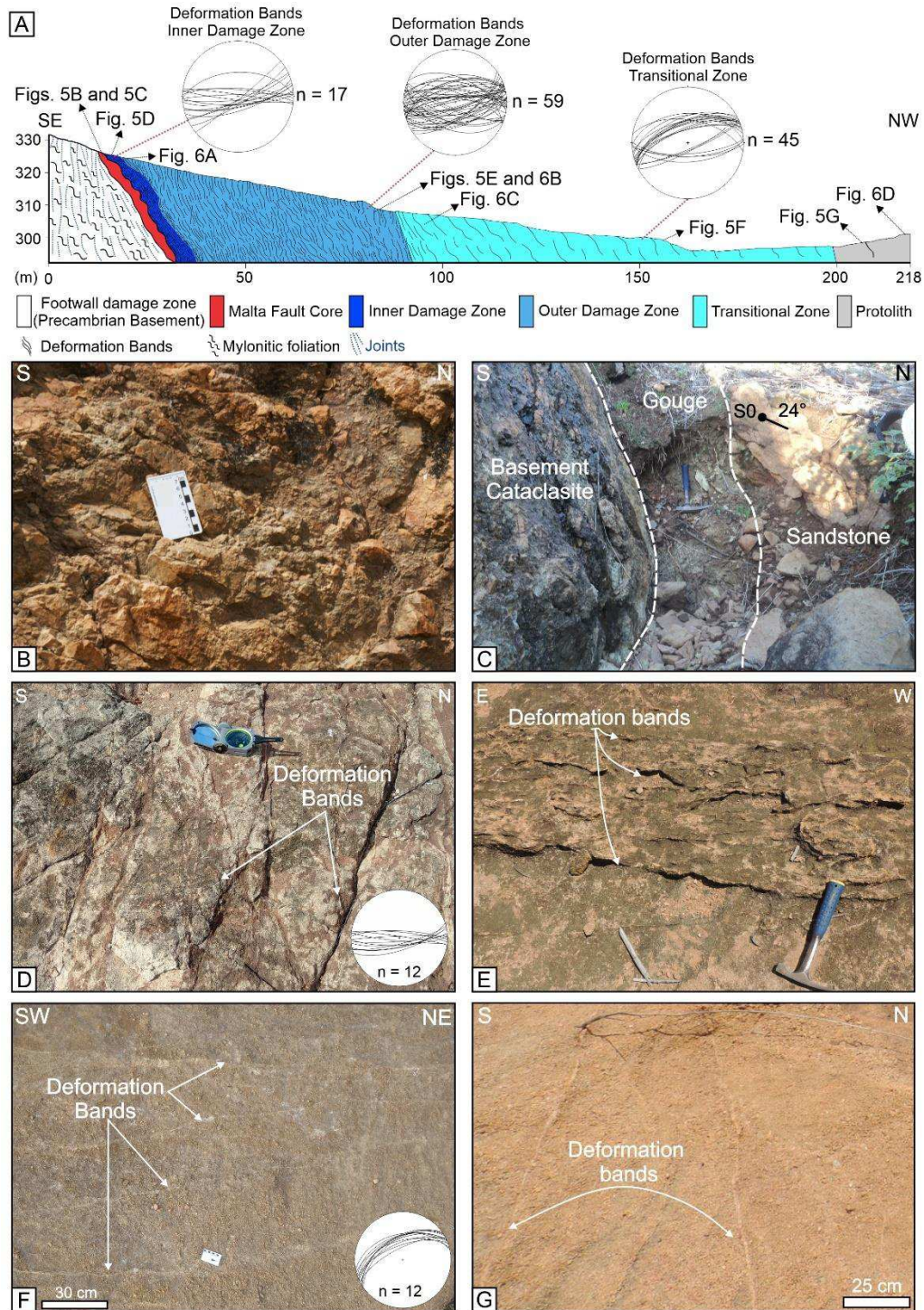
$$\text{Equation 3} \quad t_{DB} = I_{DB} T \bar{t} = F \bar{t}$$

where  $t_{DB}$  (m) is the accumulated thickness of the deformation bands in a length  $T$ ,  $I_{DB}$  is the deformation band intensity (number of deformation bands/m or DB/m),  $T$  (m) is the model cell thickness (1 m in this study),  $\bar{t}$  is the average deformation band thickness (m) in the outcrop, and  $F$  is the deformation band frequency (Fig. 4.1A).

## 4. Results

### 4.1. Main fault and its damage zone

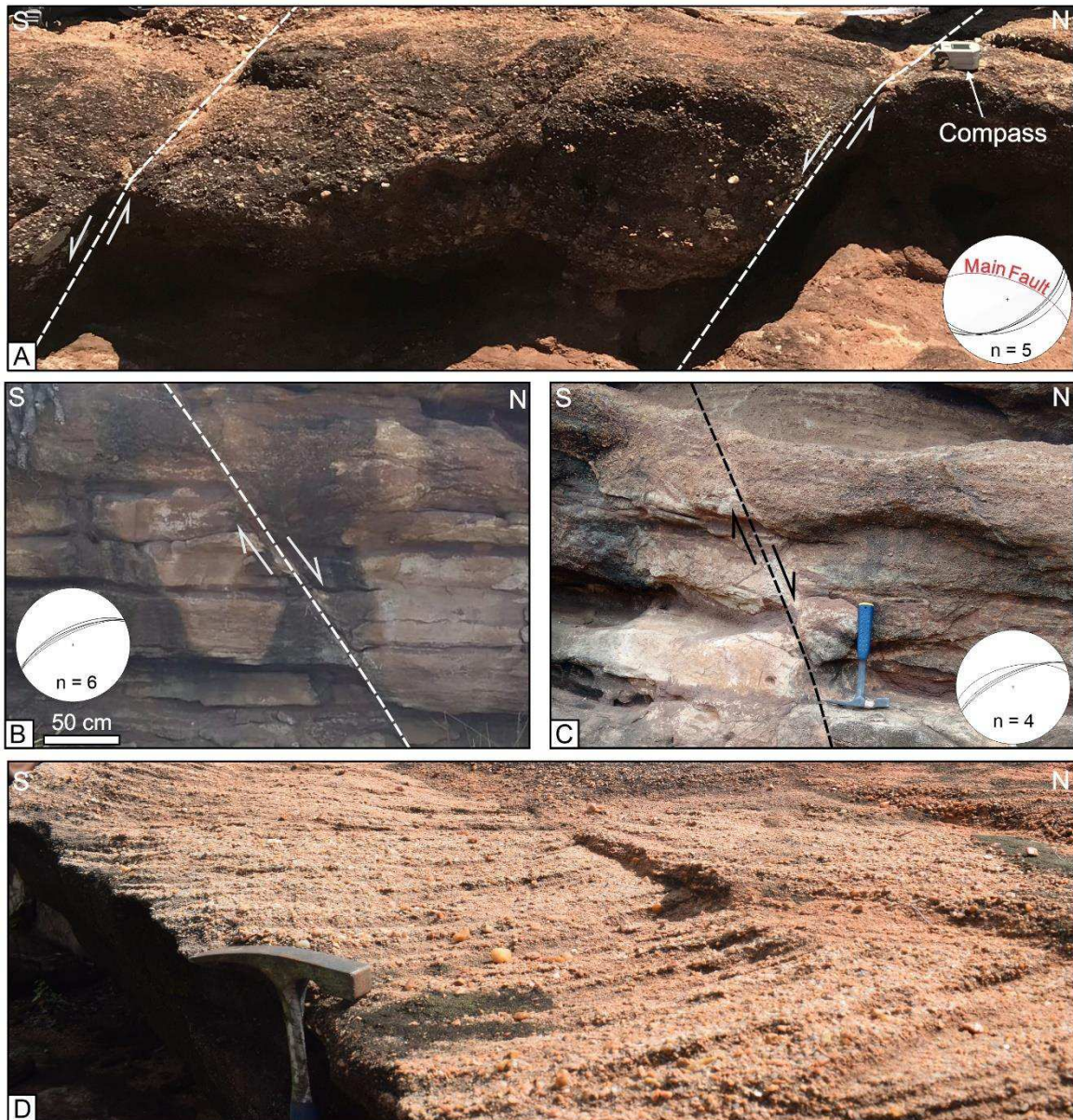
The Malta Fault segment (outcrop 1 in Fig. 4.2) strikes WNW-ESE (dip direction/plunge, 015/70). It exhibits a predominant normal fault component, juxtaposing Precambrian units of the crystalline basement in the footwall and Cretaceous siliciclastic units of the Antenor Navarro Formation in the hanging wall (Fig. 4.5A). The fault core is about 12 m thick and comprises a set of fault rocks, such as cataclasites, breccia (Fig. 4.5B, C), and gouge (Fig. 4.5C). The hanging wall damage zones comprise deformation bands (Fig. 4.5D, E, F), Quartz veins, and rare joints in fine to conglomeratic sandstones. In contrast, the footwall damage zones are composed of mylonites of crystalline rocks with joints and minor faults (Fig. 4.5A). We also noted that the deformation bands are the main structures in the inner (Fig. 4.5D) and outer (Fig. 4.5E) damage zones and transitional zone (Fig. 4.5F) in the hanging wall. We counted 2451 deformation bands and no fractures along the three linear scanlines (Table 2). These deformation bands preferentially strike E-W and ENE-WSW (Fig. 4.5A). Moreover, we observed antithetic (Fig. 4.6A) and synthetic (Fig. 4.6B, C) minor normal faults along some damage zone subdomains. We also observed that the highest frequency of deformation bands occurs close to the fault core and decreases in a non-linear pattern away from it (Fig. 4.7) toward the protolith (Figs. 5G and 6D).



**Fig. 4.5.** (A) Geological profile of the Malta Fault Zone segment (outcrop 1) and deformation band distribution and orientation in each architectural element. The Malta Fault Core comprises (B) breccia, (C) cataclasite, and gouge. Deformation bands arranged in the hanging wall damage



zone (D) in fine sandstones of the inner damage zone, (E) thicker in the outer damage zone, (F) widely spaced in the transitional zone, and (G) rarely occurring in protolith.



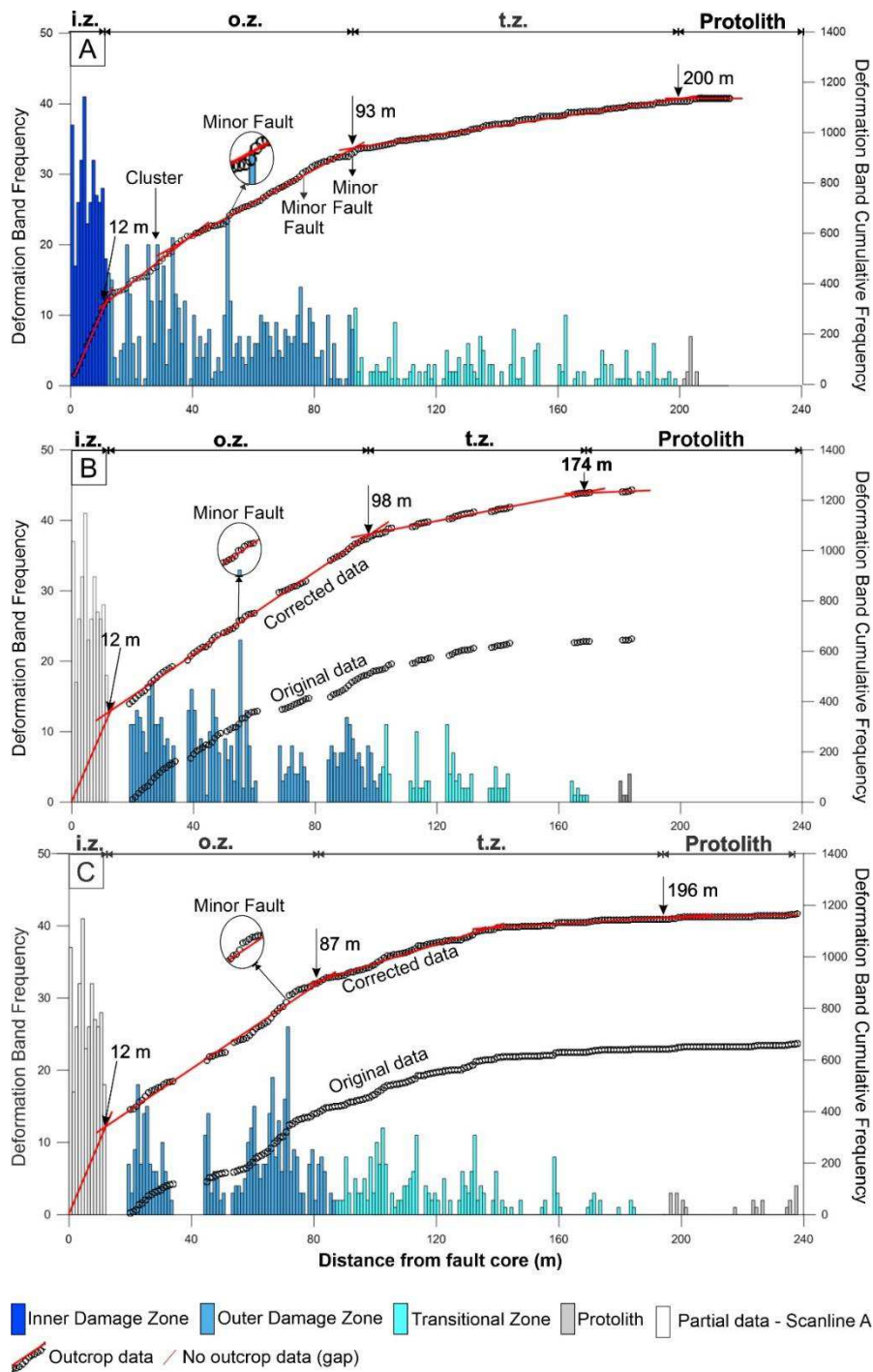
**Fig. 4.6.** Outcrop 1 pictures in the Malta Fault hanging wall damage zone, of (A) Antithetic minor normal faults in the inner/outer damage zones, synthetic minor normal faults in the (B) outer damage zone and (C) in the transitional zone, and (D) a detail of the protolith lithology, with no deformation bands. For more details on pictures localizations, see Fig. 4.5A.

We estimated the widths of the inner and outer damage zones, and transitional zone, as far as the protolith, using the deformation band cumulative frequency from the fault core (Fig. 4.7). Scanline A shows that the inner zone is 12 m thick (Fig. 4.7A). The absence of outcrop exposure in the first 17 and 23 m of scanlines B and C (Table 2) (Fig. 4.3B), respectively, did not compromise the characterization of these damage zones. Thus, considering the gradient of the inner damage zone similar in the three scanlines with a constant width (Fig. 4.7A, B, C), and using the correction proposed by Choi et al. (2016) in the other gaps of scanlines B and C, we estimated from the cumulative frequency curves (Fig. 4.7A, B, C) that (1) the inner damage zone is 12 m wide, (2) the width of the outer damage zone varies between 75 and 86 m, (3) the width of the transitional zone varies between 76 and 109 m, and (4) the protolith is 174 to 201 m from the fault core.

Additionally, we observed that the inner damage zone exhibits a section of fine sandstones (Fig. 4.5D), where the deformation bands' high frequency varying between 41 and 18 DB/m occurs (Fig. 4.7). In contrast, the outer damage zone is composed of coarse sandstones and conglomeratic sandstones (Fig. 4.5E) with deformation bands frequency between 26 and 0 DB/m (Fig. 4.7), adjacent to some minor synthetic and antithetic faults to the main fault (Fig. 4.6A, B). The thicknesses of the deformation bands vary between 0.075 mm (singles) and 25.0 mm (clusters) with a mode of 1.4 mm in the fine sandstone of the inner damage zone (Table 3). In contrast, these values vary between 0.140 mm (singles) and 100 mm (cluster), with a mode of 4.0 mm in the coarse sandstone of the outer zone (Table 3).

The transitional zone, which is also composed of coarse and conglomeratic sandstones (Fig. 4.5F), exhibits a deformation band frequency varying between 14 and 0 DB/m (Fig. 4.7) and some minor synthetic faults (Fig. 4.6C). The transitional zone changes toward the protolith (Fig. 4.5G and 6D), where the structures are less frequent or did not occur, and exhibits a

deformation band frequency varying between 7 and 0 DB/m. In the transitional zone (Fig. 4.5F), the thickness of the deformation bands varies between 0.115 mm (singles) and 75 mm (cluster), with a mode of 4.0 mm (Table 3). In contrast, in the protolith (Fig. 4.6D), a few deformation bands occur (Fig. 4.5G) as singles structures (Fig. 4.5G) with a mode thickness of 5.0 mm (Table 3).





**Fig. 4.7.** Frequency distribution and the deformation band cumulative frequency with respect to distance from the fault core on the hanging wall of the Malta Fault segment (outcrop 1 in Fig. 4.2). (A) Scanline A. (B) Scanline B. (C) Scanline C. Scanline A shows only the original data, whereas scanlines B and C exhibit the original and corrected data. The corrected data consist of the correction proposed by Choi et al. (2016) and the same gradient/width for the inner damage zone, coming from scanline A. Key: i.z = inner damage zone; o.z. = outer damage zone; t.z. = transitional zone.

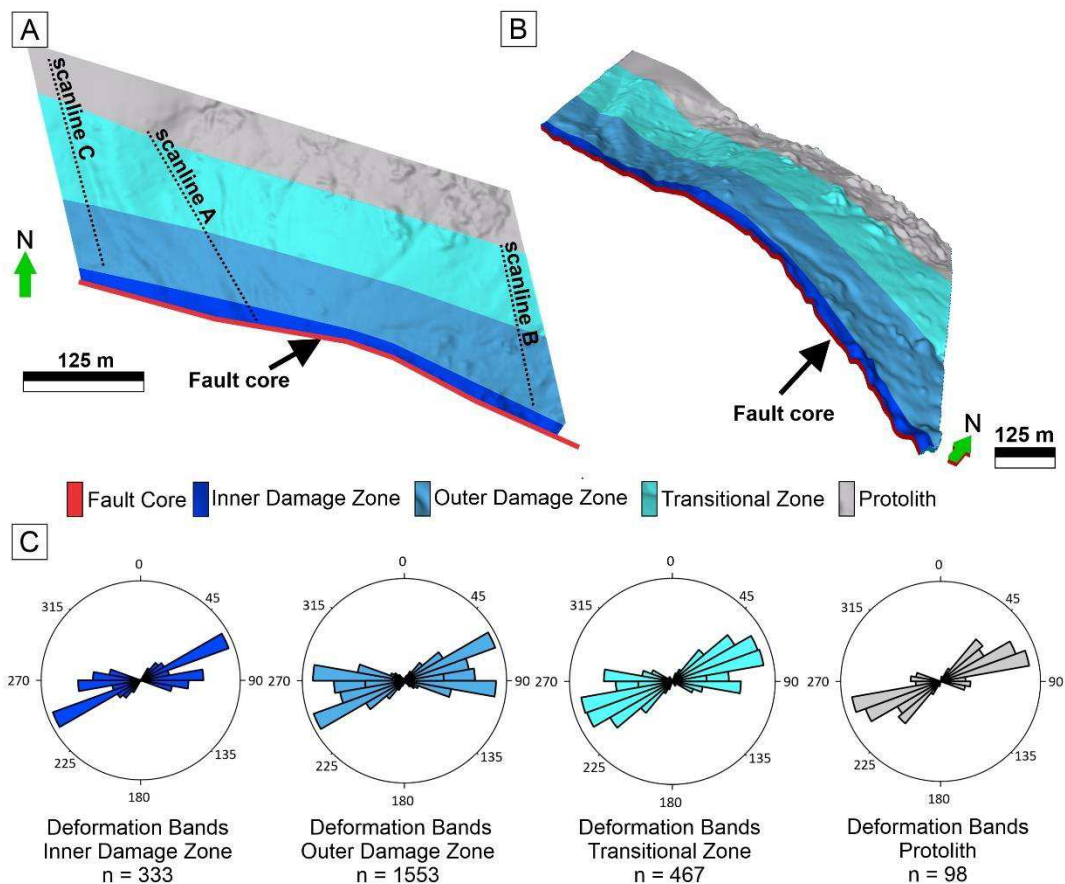
**Table 3**

Deformation band thickness in different subdomains of damage zones.

Subdomain	Number of data	Deformation band thickness (mm)				
		Average	Median	Mode	Min	Max
Inner damage zone	333	1.7	1.25	1.4	0.075	25.0
Outer damage zone	1553	4.5	2.65	4.0	0.140	100.0
Transitional zone	467	4.0	2.65	4.0	0.115	75.0
Protolith	97	2.9	3.00	5.0	0.175	10.0

#### 4.2. Modeling of damage zones

We carried out an architectural elements model of the main fault segment (outcrop 1 in Fig. 4.2), integrating the topographic model (Fig. 4.4B) into the fault core and delimiting the widths of the damage zone subdomains and the protolith (Fig. 4.8A, B). Thus, our model incorporates the fault core like a simple fault trace and linearly interpolated the lateral widths of the inner and outer damage zones, transitional zone, and the protolith, estimated from scanlines (Fig. 4.7).



**Fig. 4.8.** The damage zone model and the fault core integrated into the digital terrain model from the UAV image. (A) Top view with the scanlines location and (B) side view of the damage zone model. The model exhibits a vertical exaggeration of 1.5. (C) Stereogram orientations of deformation bands in each damage zone (inner and outer), transitional zone, and protolith.

Relating deformation bands intensity from the corrected scanlines data (Fig. 4.7) to the damage zone model of the main fault (Fig. 4.8A, B), we observed that 81.9% of the deformation bands are concentrated in 37.2% of the model's volume (Fig. 4.8A, B), corresponding to the inner and outer damage zones. The inner damage zone comprises 7.3% of our model's volume and exhibits 32.1% of the deformation band concentration. The outer damage zone corresponds to 29.9% of our model's volume and presents 49.8% of the deformation band concentration.

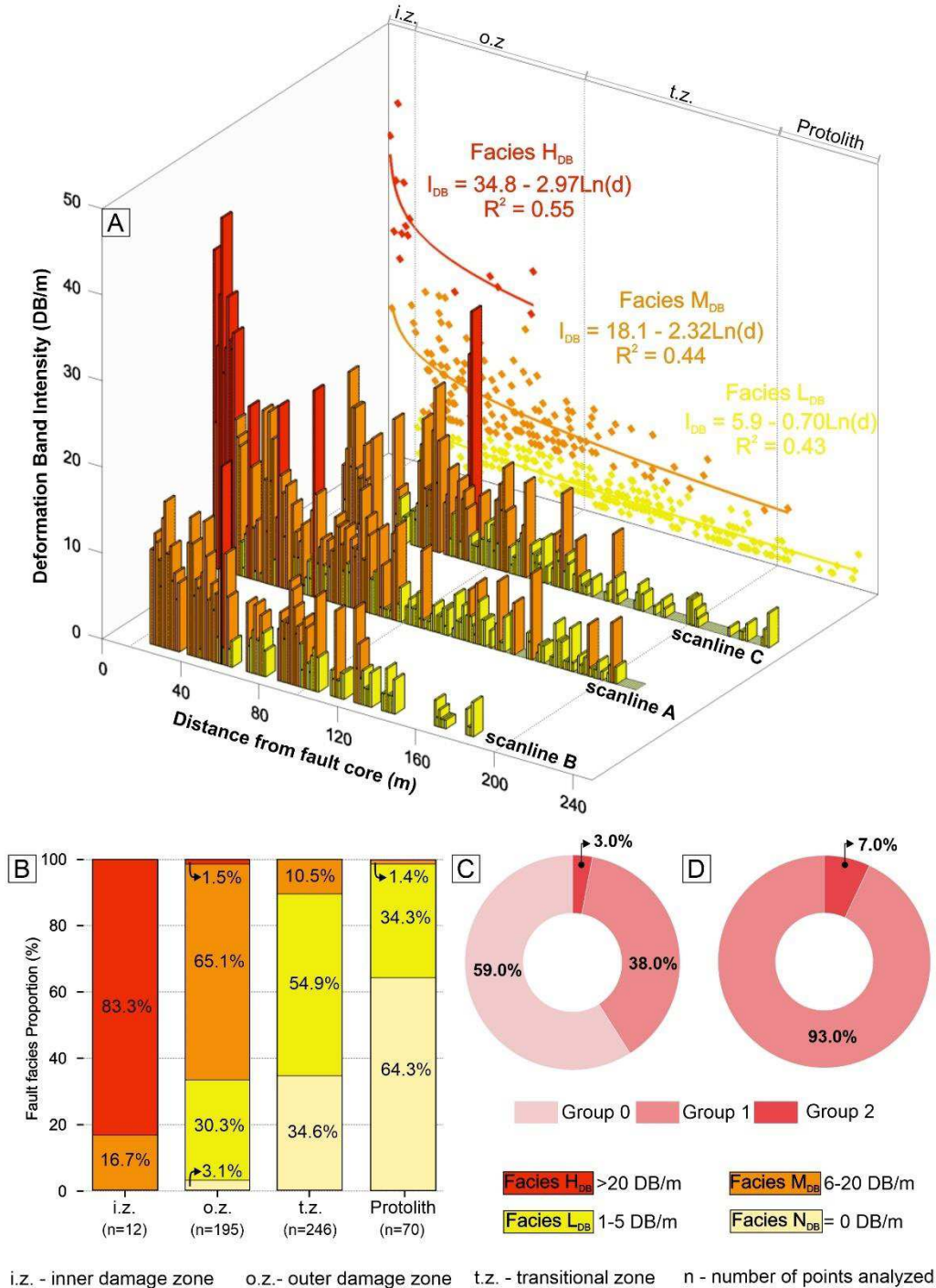
Finally, the transitional zone and protolith correspond to 36.3% and 26.5% of our model's volume and concentrate 15.0% and 3.1% of the deformation bands, respectively.

Moreover, we analyzed the 2451 orientations of the deformation bands in the damage zone subdomains and protolith along all scanlines (Fig. 4.8C). These structures mainly strike E-W and ENE-WSW, with few direction variations in these zones. For this reason, we used the main direction of the deformation bands to define the azimuth of spherical variograms (Table 1) used in modeling the fault facies and permeabilities of deformation bands and interband spaces.

#### 4.3. Fault facies analysis and modeling

Following the four fault facies delimitation at each meter along the scanlines (Fig. 4.9A), we analyze the deformation intensity and proportion of fault facies within each damage zone subdomain using these scanline data (Fig. 4.9B). We observed that the most significant deformation occurs closer to the fault core (Fig. 4.9B). For example, the  $H_{DB}$  and  $M_{DB}$  fault facies are predominant in the inner and outer damage zones, respectively, while the  $L_{DB}$  and  $N_{DB}$  are predominant in the transitional and protolith. Furthermore, we verified the spatial relationship between fault facies  $H_{DB}$ ,  $M_{DB}$ ,  $L_{DB}$ , and  $N_{DB}$  at each meter along the three scanlines, totaling 520 transitions (Fig. 4.9C, D). None of the transitions are from group 3 ( $H_{DB}$  to  $N_{DB}$ ). The more abrupt transitions are group 2,  $H_{DB}$  to  $L_{DB}$ , and  $M_{DB}$  to  $N_{DB}$ , representing only 3% of the total (Fig. 4.9C). In contrast, 38% of the transitions occur gradually (facies  $H_{DB}$  to  $M_{DB}$ ,  $M_{DB}$  to  $L_{DB}$ , and  $L_{DB}$  to  $N_{DB}$ , group 1), and 59% of the transitions do not show changes between the fault facies (group 0) (Fig. 4.9C). Analyzing only the changes between the fault facies, we observed that the group 1 transitions prevail in the entire fault damage zone (93%), and group 2 occurs locally (7%) (Fig. 4.9D). Therefore, as transitions are mostly gradual (group

1), we consider that the lateral spatial ordering between the fault facies used for modeling would be  $H_{DB}$  to  $M_{DB}$ ,  $L_{DB}$ , and  $N_{DB}$ .



**Fig. 4.9.** (A) Distribution of the deformation band intensities, at every meter along the scanlines A, B, and C, regarding the fault facies  $H_{DB}$ ,  $M_{DB}$ ,  $L_{DB}$ , and  $N_{DB}$ , and logarithmic decay

(correlation) of deformation band intensity with the distance from fault core to fault facies  $H_{DB}$ ,  $M_{DB}$  and  $L_{DB}$  (red, orange, and yellow dots, respectively). (B) Fault facies ( $H_{DB}$ ,  $M_{DB}$ ,  $L_{DB}$ , and  $N_{DB}$ ) proportions according to scanlines data in the inner and outer damage zones, transitional zone, and protolith. (C) Percentage transitions between fault facies analyzing all groups 0, 1, and 2 and analyzing (D) the groups 1 and 2.

We also analyzed the lateral continuity (x-direction) of the fault facies in each damage zone subdomain (Table 4) to determine the minor range value of the variogram for fault facies modeling. The fault facies are mostly continuous in all subdomains for only 1 m (see mode values in Table 4). However, the average of the lateral continuity is greater than 2 m in all zones. The inner damage zone showed the greatest average lateral continuity of 3.5 m, while in the other subdomains, these values varied little, between 2.4 m and 2.7 m (Table 4).

**Table 4**

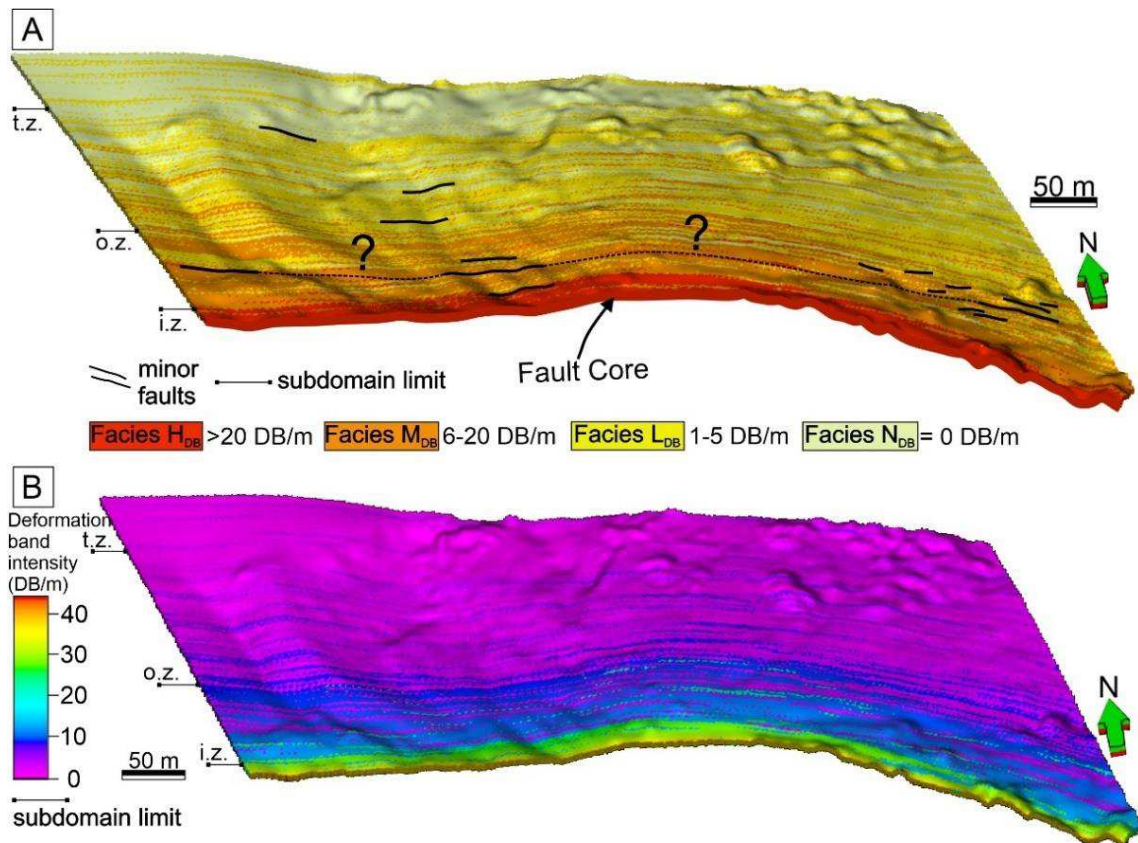
Continuity of the fault facies (x-direction) in the inner and outer damage zones, transition zone, and protolith from scanline data.

Subdomain	Number of data	Continuity of fault facies (m)				
		Average	Median	Mode	Min	Max
Inner damage zone	4	3.5	2.0	1.0	1.0	9.0
Outer damage zone	80	2.4	1.0	1.0	1.0	21.0
Transitional zone	98	2.3	1.0	1.0	1.0	19.0
Protolith	35	2.7	1.0	1.0	1.0	15.0

Proceeding in the workflow, we next modeled the fault facies (Fig. 4.10A), integrating the scanline data (Fig. 4.9A) to the outcrop model (Fig. 4.3B). We also used as input parameters:

the fault facies proportions of each damage zone subdomain (Fig. 4.9B), spatial ordering between the facies (Fig. 4.9C, D), and spherical variograms with anisotropic ranges (Tables 1 and 4). Similar to the previous analysis (Fig. 4.9), we observed in the fault facies model (Fig. 4.10A) that the inner damage zone exhibits two of the most deformation intensity fault facies (Figs. 9B and 10A):  $H_{DB}$  (83.3%) and  $M_{DB}$  (16.7%). The outer damage zone presents all fault facies (Figs. 9B and 10A), but facies  $M_{DB}$  (65.1%) and  $L_{DB}$  (30.3%) dominate. When facies  $H_{DB}$  appears in the outer damage zone (1.5%), this is associated with minor faults (indicated in Fig. 4.10A). These locations coincide with some intervals where we recorded a more abrupt variation of fault facies (group 2 in Fig. 4.9C, D). In the transitional zone (Figs. 9B and 10C), despite the occurrence of fault facies  $M_{DB}$  (10.5%), facies  $L_{DB}$  (54.9%) and  $N_{DB}$  (34.6%) are more frequent, while in the protolith fault facies  $N_{DB}$  (64.3%) predominates over facies  $L_{DB}$  (34.3%) and  $M_{DB}$  (1.4%). Similar to the inner and outer damage zones, we observed minor faults in the transitional zone. These faults are associated with group 2 transitions (Fig. 4.9C, D), corresponding to the transition from  $M_{DB}$  facies to  $N_{DB}$ . Additionally, the fault facies related to these faults is the  $M_{DB}$  facies, not the  $H_{DB}$  facies (Fig. 4.10A), as reported in the inner and outer damage zones.

Finally, we observed that the deformation band intensity of the fault facies  $H_{DB}$ ,  $M_{DB}$ , and  $L_{DB}$  vary in each subdomain or with the distance from the fault core (Fig. 4.9A) and follows different logarithmic decays/fits (Fig. 4.9A). Thus, we also built a continuous model of the deformation band intensity from the fault facies model (Fig. 4.10B) and the logarithmic decay correlations with the distance from the fault core (Fig. 4.9A). This model (Fig. 4.10B) shows the variation in the deformation intensity of each fault facies along the damage zone subdomains. Thus, we observed a level of deformation band intensity that marks each subdomain.



**Fig. 4.10.** Fault facies distribution model in the Malta Fault segment (outcrop 1 in Fig. 2) with minor faults observed in the field. (B) Continuous model of the deformation band intensity obtained through the fault facies model (Fig. 4.10A) and logarithmic decay correlation of the deformation band intensity with the distance from the fault core (Fig. 9A). The models are shown with a vertical exaggeration of 1.5x. Key: i.z. = inner damage zone; o.z. = outer damage zone; t.z. = transitional zone.

#### 4.4. Permeability analysis

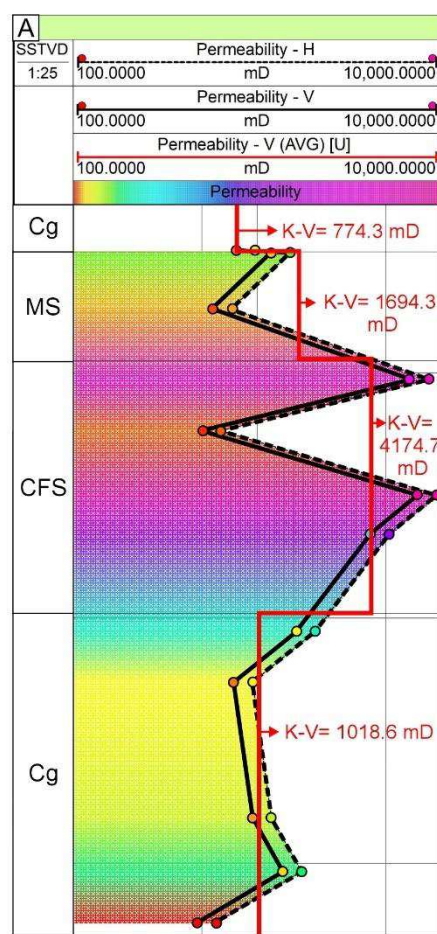
##### 4.4.1. Damage zones permeability analysis and modeling

Our permeability analysis is summarized in Fig. 4.11A, B and indicates the following points: (1) the permeabilities of undeformed rocks (outcrop 2) ( $K_{UR}$ ) vary significantly with the lithology along the analyzed section (Fig. 4.11A); (2) the undeformed fine to coarse sandstones

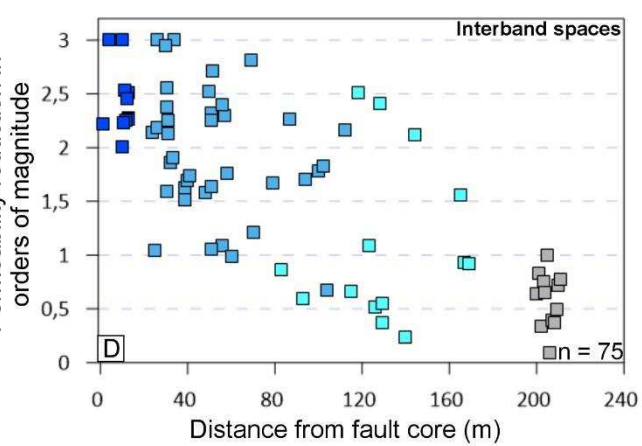
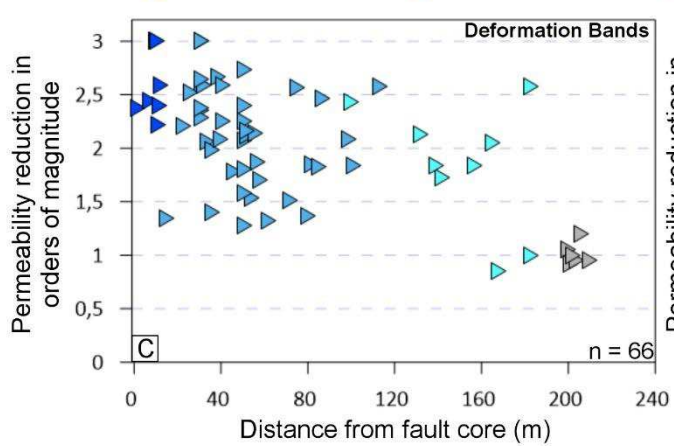
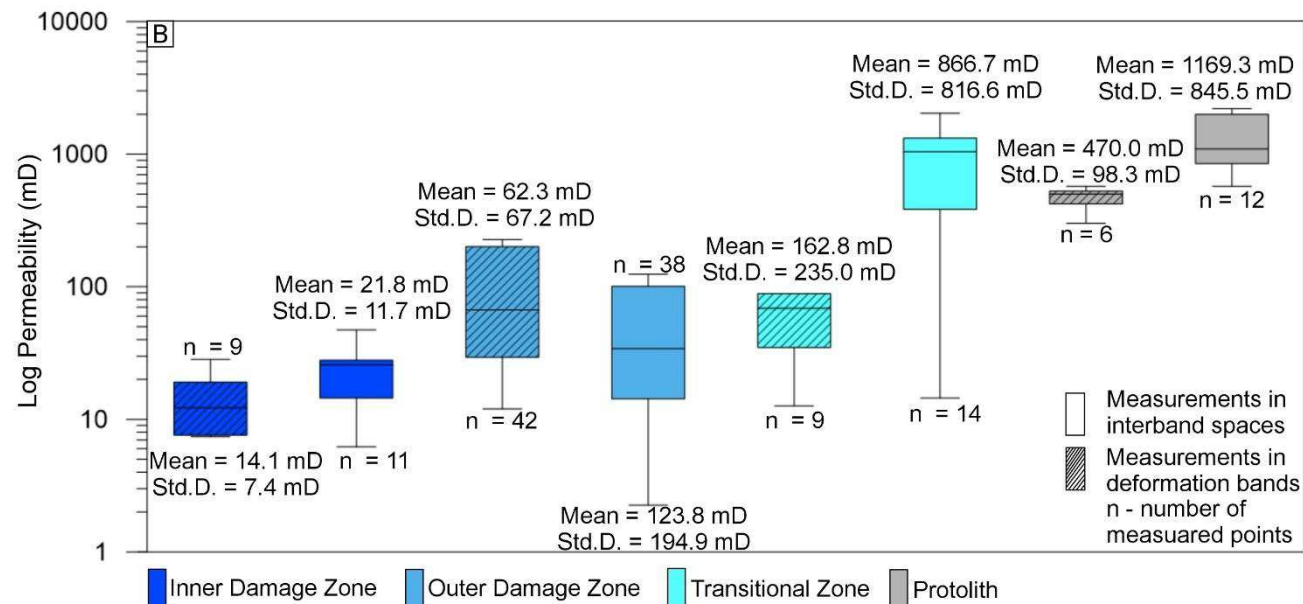
(outcrop 2) showed the highest average vertical permeability values (4174.7 mD) (Fig. 4.11A), which corresponds to approximately four times the average permeability of the protolith (outcrop 1) (Fig. 4.11B); (3) both the permeability of the deformation bands ( $K_{DB}$ ) and the interband spaces ( $K_{IDB}$ ) exhibit an increasing trend from the inner and outer damage zones to the transitional zone and protolith (Fig. 4.11B).

In addition, we analyzed the reduction in orders of magnitude with the distance from the fault core of the permeabilities of deformation bands ( $K_{DB}$ ), and interband spaces ( $K_{IDB}$ ) compared to fine to coarse undeformed sandstones (outcrop 2) (Fig. 4.11C, D). We observed that the largest reductions in orders of magnitude of both  $K_{DB}$  and  $K_{IDB}$  compared to  $K_{UR}$  happen near the fault core and are smaller with distance from it (Fig. 4.11C, D). For instance, the inner damage zone showed the largest  $K_{DB}$  and  $K_{IDB}$  reductions in orders of magnitude, between 2.0–3.0. The outer damage zone presents reductions to  $K_{DB}$  e  $K_{IDB}$  compared to  $K_{UR}$  of 1.0–3.0 and 0.5–3.0, respectively. Finally, the reductions of  $K_{DB}$  compared to  $K_{UR}$  are smaller in the transitional zone (2.5-0.5 orders) and the protolith (1.0 order), as are those of  $K_{IDB}$ , between 0.0-2.5 in the transitional zone and 0.0-1.0 in the protolith.





Cg - conglomerates  
 CFS - Coarse to fine sandstones  
 MS - Medium sandstones  
 H - Horizontal V - Vertical  
 K-V - Vertical permeability  
 AVG - Average  
 ● Points with permeability measures

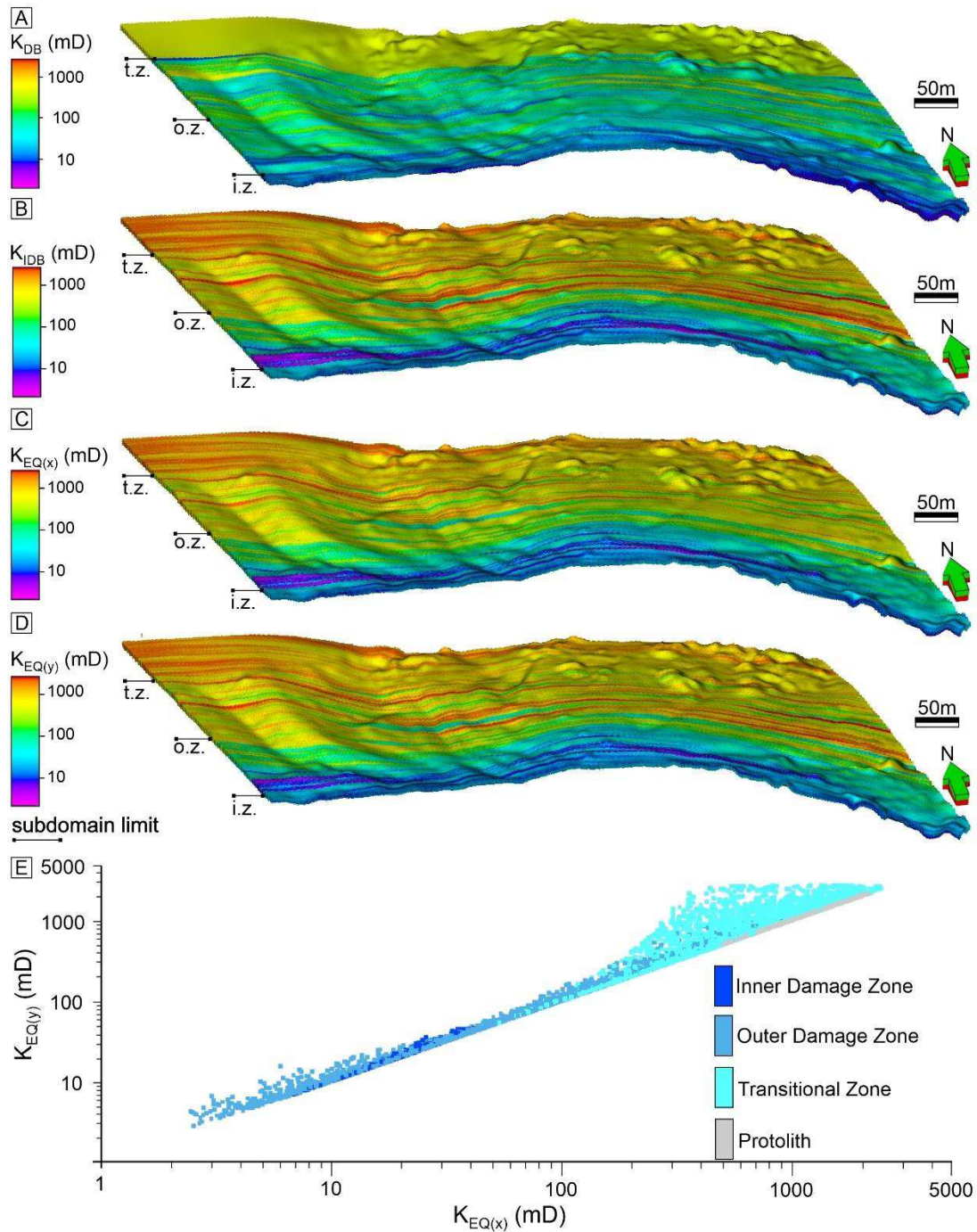


■ Measurements in inner damage zone    ■ Measurements in outer damage zone  
 ■ Measurements in transitional zone    ■ Measurements in protolith

**Fig. 4.11.** (A) Horizontal (measured) and vertical (estimated from the relationship obtained by Shedid (2019) permeabilities profiles of undeformed rocks (outcrop 2 in Fig. 4.2). Details of the measurement points along conglomerates, medium sandstones, and fine to coarse sandstones are available in Fig. 4.3B (points 1 to 12). The solid red line shows the average permeability value by lithology. (B) Permeability diagram in the deformation bands and interband spaces for the inner and outer damage zone, transitional zone, and protolith along the Malta Fault segment (outcrop 4.2 in Fig. 1). The black lines within the box represent the median value. The black lines on the top and bottom are the maximum and minimum values, respectively. Permeability distribution reductions, in orders of magnitude, with the distance from the fault core of (C) the deformation bands and (D) interband spaces for each zone (inner and outer damage zone, transitional zone, and protolith) of the Malta Fault segment (outcrop 1 in Fig. 4.1) compared to undeformed rocks (coarse to fine sandstones in Fig. 4.11A).

Subsequently, we modeled the  $K_{DB}$  and  $K_{IDB}$  (Fig. 4.12A, B), incorporating the  $K_{DB}$  and  $K_{IDB}$  data into the damage zone model (Fig. 4.8A, B). In the  $K_{DB}$  and  $K_{IDB}$  models (Fig. 4.12A, B), the inner damage zone concentrates the lowest permeability values, with averages of 14.1 mD for the deformation bands and 21.8 mD in interband spaces. The outer damage zone predominantly concentrates cells with  $K_{DB}$  and  $K_{IDB}$  between 20 mD and 227 mD, with averages of 62.3mD and 123.8mD, respectively (Figs. 11B and 12A, B). In addition, the outer damage zone presents some isolated cells with  $K_{DB}$  of about 10 mD and  $K_{IDB}$  greater than 100 mD (up to 2000 mD) (Fig. 4.12A, B). The transitional zone shows mainly cells with  $K_{DB}$  between 35 mD and 200 mD (average of 162.8 mD), and few cells with  $K_{DB}$  less than 10 mD and 470 mD. The protolith has small variations in this property, with an average  $K_{DB}$  of 470 mD (Figs. 11B and 12A). Regarding the  $K_{IDB}$  distribution, the transitional zone and the protolith have mainly permeability cells between 720 mD and 1200 mD, with  $K_{IDB}$  averages of 866.7 mD and 1169.3

mD, respectively. Some cells with  $K_{IDB}$  of 100 mD and above 1200 mD (Fig. 4.12B) are observed in the transitional zone and protolith (Fig. 4.12B).



**Fig. 4.12.** 3D models, conditioned to the damage zone model, of the (A) deformation band permeability ( $K_{DB}$ ), (B) interband spaces permeability ( $K_{IDB}$ ), and equivalent permeabilities (C) perpendicular,  $K_{EQ(x)}$ , and (D) parallel,  $K_{EQ(y)}$ , to the main fault. (E) Graph of equivalent PPGPEM – UFCG

permeability perpendicular ( $K_{EQ(x)}$ ) versus parallel ( $K_{EQ(y)}$ ) to the main fault modeled according to the damage zone subdomains model (data from the  $K_{EQ(x)}$  and  $K_{EQ(y)}$  models, in Fig. 4.12C, D). The models exhibit a vertical exaggeration of 1.5x. Key: i.z = inner damage zone; o.z. = outer damage zone; t.z. = transitional zone.

Using the  $K_{DB}$  and  $K_{IDB}$  models (Fig. 4.12A, B), we calculated the equivalent permeabilities (Fig. 4.12C, D) perpendicular ( $K_{EQ(x)}$ ) and parallel ( $K_{EQ(y)}$ ) to the main fault according to the damage zones model along all 3D-grid (outcrop model). From these  $K_{EQ(x)}$  and  $K_{EQ(y)}$  models (Fig. 4.12C, D), we observed similarly to the  $K_{IDB}$  model that the inner and outer damage zones have equivalent permeabilities predominantly between 10 mD and 100 mD in both directions. However, the transitional zone presents the greatest contrasts between  $K_{EQ(x)}$  and  $K_{EQ(y)}$  (Fig. 4.12C, D). For example, the  $K_{EQ(x)}$  model has cells mainly between 100 mD and 500 mD. In comparison, the  $K_{EQ(y)}$  model has mostly cells with permeability between 500 mD and 1000 mD and even cells with a permeability greater than 1000 mD (red cells in Fig. 4.12D). The protolith exhibits small variations between  $K_{EQ(x)}$  and  $K_{EQ(y)}$  (according to the models in Fig. 4.12C, D), wherein both models, cells with 1000 mD are pervasive.

The relationship between  $K_{EQ(x)}$  and  $K_{EQ(y)}$  calculated along the grid, according to the damage zone subdomains, is summarized in the cross-plot graph (Fig. 4.12E). This graph (Fig. 4.12E) shows an linear relationship between the  $K_{EQ(x)}$  and  $K_{EQ(y)}$ . Therefore, (1) each damage zone subdomain occupies limited ranges of  $K_{EQ}$ s; (2) the inner and outer damage zones and the protolith have a little dispersed pattern between these  $K_{EQ}$ , which means that  $K_{EQ}$ s is less contrasting and more connected within each subdomain; (3) the transitional zone showed a more dispersed and contrasting pattern between the  $K_{EQ}$ , indicating that similar  $K_{EQ(x)}$  values can be associated with very variable  $K_{EQ(y)}$  values (less connected). Finally, we observed the equivalent permeability distribution in the cells of  $K_{EQ(x)}$  and  $K_{EQ(y)}$  models (Table 5). Similar

number of cells was observed in all ranges of the  $K_{EQ(x)}$  and  $K_{EQ(y)}$  models, with a small decrease in the percentage of cell numbers with equivalent permeability less than 10.0 mD (to 2.8%) and an increased number of cells with such permeabilities greater than 500.0 mD, compared the  $K_{EQ(y)}$  model to  $K_{EQ(x)}$  (Table 5).

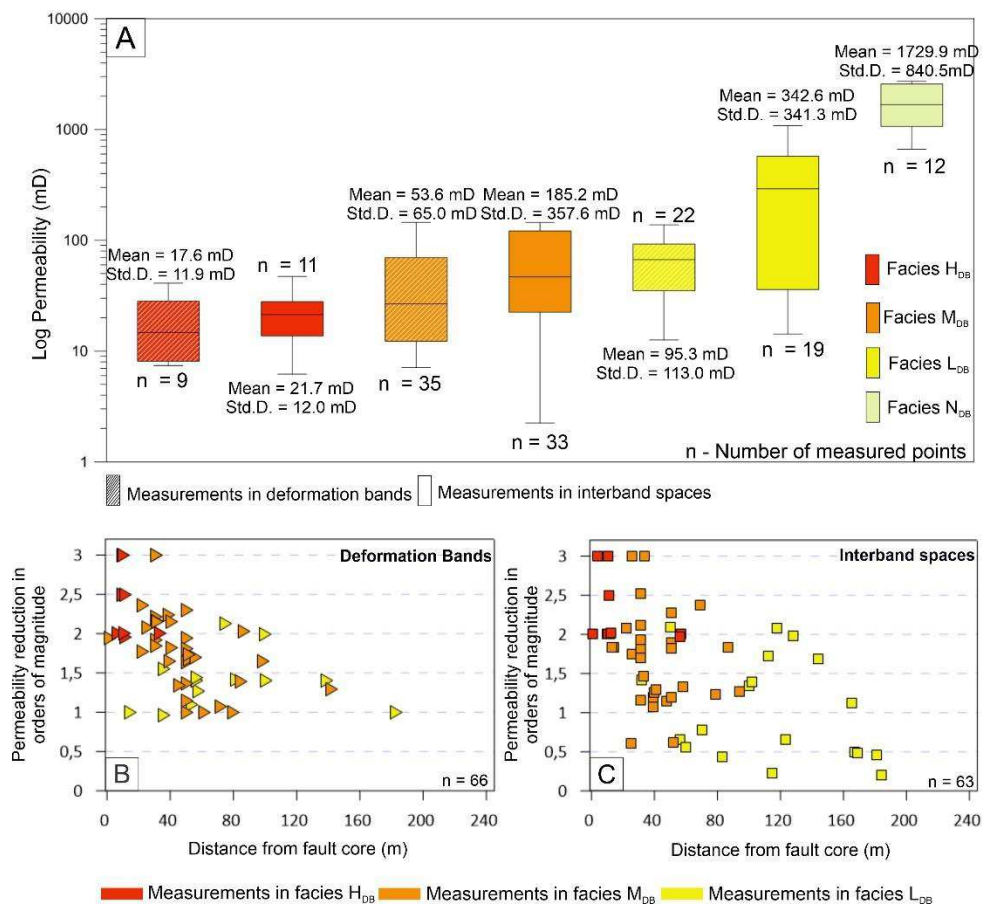
#### 4.4.2. Fault facies permeability analysis and modeling

The analyzes of fault facies permeabilities (Fig. 4.13A) showed an increasing trend of permeability from the more deformed ( $H_{DB}$ ) to the less deformed facies ( $N_{DB}$ ). We also verified the permeability reductions in orders of magnitude with distance from the fault core of deformation bands and interband space of  $H_{DB}$ ,  $M_{DB}$ , and  $L_{DB}$  facies compared to the average permeability of  $N_{DB}$  facies (Fig. 4.13B, C). We observed that the  $K_{DB}$  and  $K_{IDB}$  showed the largest reductions near the fault core, and there is a downward trend for these reductions with distance from it, especially for  $K_{IDB}$  (Fig. 4.13C). The  $H_{DB}$  fault facies, which occur mainly close to the fault core, showed reductions between 2.0–3.0 orders of magnitude in both  $K_{DB}$  and  $K_{IDB}$  compared to the permeability of the  $N_{DB}$  facies (Fig. 4.13B, C). Furthermore, the  $M_{DB}$  and  $L_{DB}$  fault facies showed very similar reductions of  $K_{DB}$ , between 1.0-3.0 orders and 1.0-2.5 orders, respectively, with slight variation from the fault core (Fig. 4.13B). However, greater  $K_{IDB}$  reductions with distance from the fault core occur in the  $M_{DB}$  and  $L_{DB}$  fault facies (Fig. 4.13C). The  $M_{DB}$  fault facies presented reductions between 0.5.–3.0 orders of magnitude and the  $L_{DB}$  between 0–2.5 orders of magnitude compared to permeability of the  $N_{DB}$  facies.

The  $K_{DB}$  and  $K_{IDB}$  data (Fig. 4.13A) were integrated into the fault facies model (Fig. 4.10) and thus distributed along it (Fig. 4.14A, B). The  $K_{DB}$  model (Fig. 4.14A) shows in the inner and outer damage zones the predominance of cells with  $K_{DB}$  of 10 mD associated with  $H_{DB}$  facies (average of 17.6) and between 10 mD and 100 mD associated with  $M_{DB}$  (average of 53.6) facies (Fig. 4.13A). In the outer damage zone (Fig. 4.14A), cells are observed rarely with



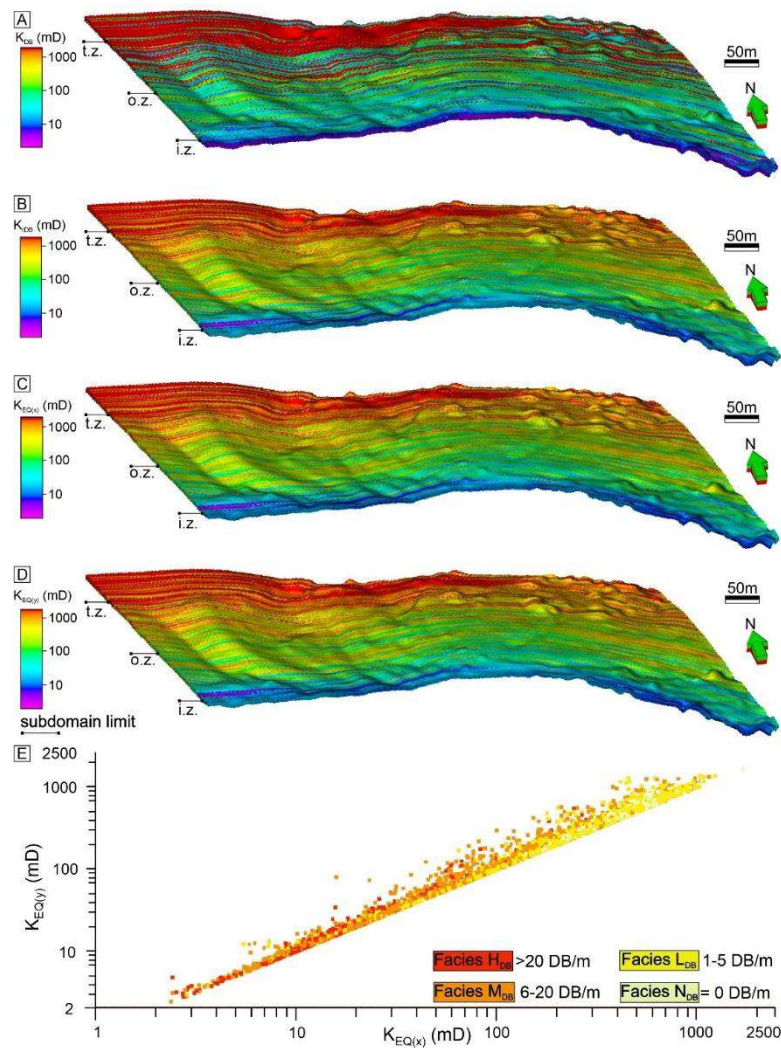
$K_{DB}$  of about 100 mD ( $L_{DB}$  facies), with an average of 95.2 mD, or equal to 1729.9 mD ( $N_{DB}$  facies). In the transitional zone, the cells of the  $K_{DB}$  model (Fig. 4.14A) are predominantly concentrated between intervals of about 100 mD ( $L_{DB}$  facies), with some cells with permeability close to 10 mD (facies  $M_{DB}$ ). When the deformation bands occur in the protolith subdomain, associated with the  $M_{DB}$  and  $L_{DB}$  facies (Fig. 4.10A), the  $K_{DB}$  in this zone's cells (Fig. 4.14A) varies between 10 mD and a more than 100 mD.



**Fig. 4.13.** (A) Permeability graph of the deformation bands and interband spaces for facies  $H_{DB}$ ,  $M_{DB}$ ,  $L_{DB}$ , and  $N_{DB}$ . The black lines within the box mean the median value. The black lines on the top and bottom mean the maximum and minimum values, respectively. Permeability reduction distribution, in orders of magnitude, in the (B) deformation bands and (C) interband

spaces for the facies  $H_{DB}$ ,  $M_{DB}$ , and  $L_{DB}$  compared to facies  $N_{DB}$ , with the distance from the fault core.

In the  $K_{IDB}$  model (Fig. 4.14B), the inner damage zone presents a distribution of  $K_{IDB}$  similar to that of the  $K_{DB}$  with  $K_{IDB}$  model cells predominantly between 2 mD and just over 10 mD, in agreement with the  $K_{IDB}$  average of  $H_{DB}$  and  $M_{DB}$  fault facies (Fig. 4.13A). The outer damage zone and transitional zone, the  $K_{IDB}$  (Fig. 4.14B) mainly occurs between 100 mD and 500 mD, associated with the facies  $M_{DB}$  and  $L_{DB}$  (Fig. 4.13A). In the protolith, the interband space permeability is mostly above 1000 mD ( $N_{DB}$  facies), with few  $K_{IDB}$  model cells with permeability below 1000 mD.



**Fig. 4.14.** 3D models, conditioned to the fault facies model (Fig. 4.10), of the (A) deformation band permeability ( $K_{DB}$ ), (B) interband spaces permeability ( $K_{IDB}$ ), and equivalent permeabilities (C) perpendicular,  $K_{EQ(x)}$ , and (D) parallel,  $K_{EQ(y)}$ , to the main fault. (E) Graph of equivalent permeability perpendicular ( $K_{EQ(x)}$ ) versus parallel ( $K_{EQ(y)}$ ) to the main fault modeled according to the fault facies (data from the  $K_{EQ(x)}$  and  $K_{EQ(y)}$  models, in Fig. 4.14C, D). The models exhibit a vertical exaggeration of 1.5x. Key: i.z = inner damage zone; o.z. = outer damage zone; t.z. = transitional zone.

Moreover, we calculated the equivalent permeabilities perpendicular ( $K_{EQ(x)}$ ) and parallel ( $K_{EQ(y)}$ ) to the main fault along the 3D grid (outcrop model). Then, we got the equivalent permeability models conditioned to the fault facies for x (Fig. 4.14C) and y directions (Fig. 4.14D). We observed that the distribution of  $K_{EQ(x)}$  and  $K_{EQ(y)}$  along the models (Fig. 4.14C, D) are similar to the  $K_{IDB}$  distribution (Fig. 4.14B). In contrast to the  $K_{EQ(x)}$  and  $K_{EQ(y)}$  models built from the analysis of damage zone subdomains (Figs. 12C, D, and 12E), we observed that the values of equivalent permeability of the fault facies do not have values in specific ranges. Still, the values can vary 2.0 orders of magnitude (Fig. 4.14E).

**Table 5**

Distribution of equivalent permeability in the cells of the  $K_{EQ(x)}$  and  $K_{EQ(y)}$  models conditioned to the fault facies (FF) and damage zone subdomains (DZS) models.

Equivalent permeability (mD)	Percentage of Cells (%)			
	$K_{EQ(x)}$ model (FF)	$K_{EQ(y)}$ model (FF)	$K_{EQ(x)}$ model (DZS)	$K_{EQ(y)}$ model (DZS)
<10	3.3	2.8	2.1	1.8
>10-100	24.1	24.0	25.3	25.4
>100-500	28.1	20.5	34.3	30.3
>500-1000	23.6	29.9	12.4	18.1



---

>1000	20.9	22.8	25.9	24.4
-------	------	------	------	------

---

We also verified the distribution (Table 5) of the cells of the  $K_{EQ(x)}$  and  $K_{EQ(y)}$  models (Fig. 4.14C, D) according to the fault facies analysis. The percentage of cells in the equivalent permeability model ( $K_{EQ(y)}$ ) parallel to the main fault (Fig. 4.14D) is similar at each analyzed interval (Table 5) in the  $K_{EQ(x)}$  model. We compared the  $K_{EQ(y)}$  model with the  $K_{EQ(x)}$  model and observed only a small decrease in the percentage of cells with permeabilities lower than 10.0 mD and an increase in the percentage of cells with more than 500.0 mD.

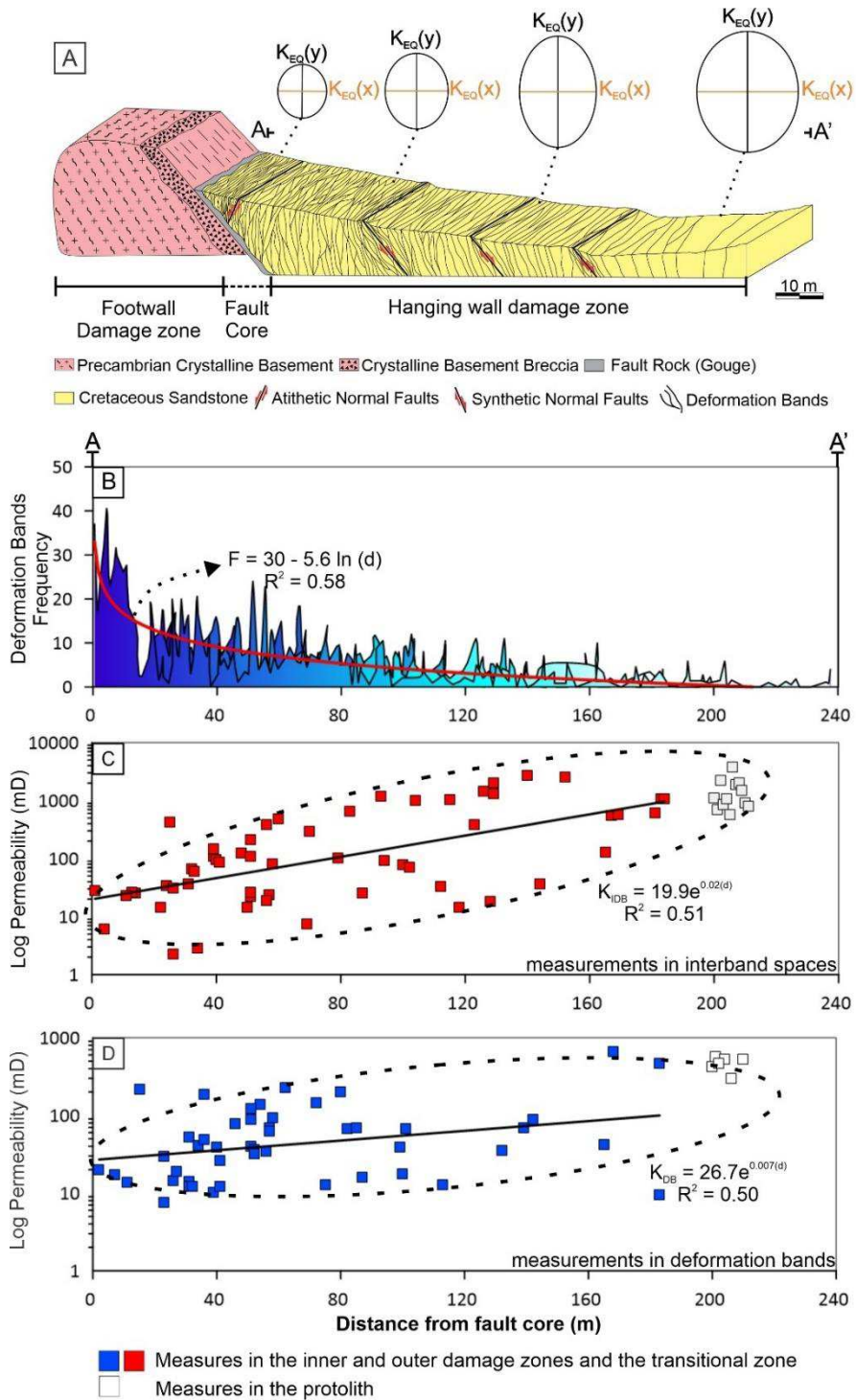
## 5. Discussion

### 5.1. Characterization and modeling of damage zones and fault facies

To understand the impact of fault damage zone on hydrocarbon reservoir, it is essential to define the Damage Zone boundaries (Schueller et al., 2013; Choi et al., 2016; Bistacchi et al., 2020) and their controlling factors, such as displacement and mechanical behavior in different layers (Alaei and Torabi, 2017; Balsamo et al., 2019; Ma et al., 2019; Torabi et al., 2020a; Navabi et al., 2020). Similarly, it is crucial to characterize the main elements of damage zones, their distributions (Schueller et al., 2013; Fossen et al., 2017), and petrophysical properties (Farrel et al., 2014; Debenham et al., 2019; Del Sole et al., 2020).

In this study, we identified (Fig. 4.7) and modeled (Fig. 4.8A, B) the boundaries of the hanging wall damage zone subdomains of a basin-bounding fault segment (Malta Fault in Fig. 4.2). We observed that the single and cluster deformation bands (Figs. 5D, E, F, and 15A) were the main structures developed throughout all these damage zone subdomains (Fig. 4.5A) on the hanging wall of this main fault. These results agree with previous studies carried out in the damage zones of that same fault (e.g., Araújo et al., 2018), as well as in the damage zones of

the Portalegre Fault (e.g., Nicchio et al., 2018; Pontes et al., 2019; Nogueira et al., 2021). The deformation bands of this study area were characterized as cataclastic bands (Nicchio et al., 2018), whose strikes (ENE-WSW) (Figs. 5A and 8C) and kinematics were directly influenced by the main fault (Figs. 2 and 3B) (Araújo et al., 2018).



**Fig. 4.15.** (A) Conceptual model of the fault zone, with the main architectural elements, the footwall and hanging wall damage zones, and the fault core. In the hanging wall damage zone, the distribution of deformation bands and their configurations (anastomosed pattern) are illustrated, as well as the permeability tensor, parallel and perpendicular to the main fault, from A to A' throughout this zone. (B) logarithmic decay of the deformation bands frequency from the fault core towards the protolith, and exponential increase permeability (C) of the interband spaces and (D) deformation bands.

Minor antithetic and (Fig. 4.6A) synthetic faults (Fig. 4.6B, C) to the main fault (Fig. 4.15A) were also observed in the hanging wall damage zone, which, according to Faulkner et al. (2010) and Navabi et al. (2020), can be explained by various slip cycles associated with increasing shear stress throughout the evolutionary stages of a fault zone. Associated with these minor faults, we identified local variations in the three accumulated frequency curves or a polymodal pattern in the bar graph (Fig. 4.7). This type of interpretation has been suggested previously in several studies (e.g., Choi et al., 2016; Soliva et al., 2016; Torabi et al., 2020a), where these local variations (Choi et al., 2016; Torabi et al., 2020a) or polymodal pattern (Soliva et al., 2016) may be associated with minor faults and with clustering, changes in the mechanical properties of layers, or even the interaction of damage zones from different faults.

Some studies report the changes in the frequency distribution of deformation bands in different sedimentary layers (e.g., Shipton and Cowie 2001; Fossen et al., 2007) and the strong control of grain size on the thickness of cataclastic deformation bands (e.g., Fossen et al., 2007, 2017), including in the RPB (Araújo et al., 2018). In this study, we observed that the deformation band thickness varied significantly with the variation of the lithological/grain size aspects (Table 3), increasing from the fine sandstones of the inner damage zone to the coarse and conglomeratic sandstones of the other subdomains on average from 1.7 to 2.6 times (Table

3). For example, the thickness varies from 1.7 mm in the inner damage zone to 4.5 mm in the outer, 4.0 mm in the transitional zone, and 2.9 mm in the protolith. This relationship between variations in the deformation band clusters thickness and lithological variations agrees with those made by Fossen et al. (2017) in porous sandstones of the Entrada Formation (Utah), which also observed that the clusters thickness systematically increased from very fine sandstones to coarse sandstones.

The deformation intensity along all damage zones subdomains is maximum near the fault core (Figs. 7 and 15A), equal to 41 DBs/m, and decrease in a logarithmic way (Fig. 4.15B) up to ~ 1 DB/m (protolith), following the function  $F = 30 - 5.6 \ln(d)$ , where  $F$  is the deformation band frequency/m and  $d$  is the distance from the fault core. The logarithmic decay observed in our study is consistent with those presented by Schueller et al. (2013), Fossen et al. (2017), and Mayolle et al. (2019). Considering that the background deformation band frequency in the protolith is 1 DB/m, from the logarithm decay, the damage zone width would be ~ 178 m from the main fault. These results are to those obtained through the methodologies proposed by Berg and Skar (2005) and Choi et al. (2016), where the inner and outer damage zones, and the transitional zone are approximately 200 m thick. Besides, our results corroborate those presented by Araújo et al. (2018), which recorded a value of 43 DB/m close to the Malta Fault core. Araújo et al. (2018) also investigated two other segments of the Portalegre Fault, another major fault in RPB (PAF in Fig. 4.2), also suggesting a deformation band logarithm decrease in the RPB. Other functions can fit the decay of structures in the damage zones. For example, Celestino et al. (2020) report a decrease in the deformation intensity following a power law distribution in a basin-bounding damage zone in the Araripe Basin, located approximately 150 km SW of the study area.

In addition to previous work (e.g., Berg and Skar, 2005; Choi et al., 2016; Araújo et al., 2018; Celestino et al., 2020; Torabi et al., 2020a), we correlated the percentage volumes of each damage zone subdomain with the deformation band intensity (Figs. 7, 8, and 9B). According to Fachri et al. (2011, 2013a), the damage zone width directly impacts properties such as equivalent permeability and fluid flow in hydrocarbon reservoirs. Thus, we infer that identifying and correlating the damage zone subdomain volumes with their deformation intensities are relevant for characterizing fault zones (e.g., Malta Fault in RPB).

The evaluation of transition patterns among fault facies has shown that ordered spatial relationships occurred in 93.0% of the contacts between different facies are from group 1 (Fig. 4.9D), and only 7.0% from group 2 (Fig. 4.9D). These results are similar to those presented by Fachri et al. (2013b) and Qu and Tveranger (2016). However, we observed that the fault facies transitions  $H_{DB}/L_{DB}$  and  $M_{DB}/N_{DB}$  (group 2 contacts) (Figs. 9A and 10A) coincide mostly with the local variations in the cumulative frequency graph (Fig. 4.7). These local variations are associated with minor faults present in these damage zone subdomains, indicated in the fault facies model (Fig. 4.10A). Besides, some points with transitions of group 2 or minor faults (Fig. 4.10A) appear aligned on the scanlines, between 52 and 67 m away from the fault core (Figs. 7 and 10A). This pattern may be associated with the occurrence of a continuous segment of a synthetic major fault (dashed line in Fig. 4.10A).

Furthermore, the spatial relationship between the fault facies (Fig. 4.9C, D) is replicable at the subdomains scale, where each zone has a predominance of one fault facies (Fig. 4.9B) with a greater or lesser degree than the adjacent zones. Previous work has not addressed the fault facies proportions in the damage zone subdomains (e.g., Fachri et al., 2011). However, we suggest that this approach is applicable and of great importance to modeling fault facies in the subsurface, since the damage zone subdomains are identifiable through the application of PPGPEM – UFCG

seismic attributes (e.g., Alaei and Torabi, 2017; Liao et al., 2020a, 2020b) and the proportions of these facies can be analyzed in different tectonic contexts with outcrop data (e.g., Fachri et al., 2011; this study). Fachri et al. (2011) show results of fault facies percentage in each of the damage zone subdomains similar to those of this study. We also infer that the analysis of the correlations between the deformation band intensity ( $I_{DB}$ ) with the distance from the fault core (Fig. 4.9A) in each of the fault facies can lead to more accurate models of this property ( $I_{DB}$ ) and equivalent permeabilities calculation so that the  $I_{DB}$  can vary a lot with the distance from the fault core.

### *5.2. Permeability and its connections with different deformational aspects in porous sandstones*

The relationships between the permeability of the deformation bands ( $K_{DB}$ ) and interband spaces ( $K_{IDB}$ ) associated with relatively undeformed ‘host rock’ ( $K_{UR}$ ), were analyzed in different geological contexts, tectonic regimes, types of deformation bands, and lithologies (Antonellini and Aydin, 1994; Torabi and Fossen, 2009; Balsamo and Storti, 2010; Torabi et al., 2013; Ballas et al., 2015; Del Sole et al., 2020; Pizzati et al., 2020; Nogueira et al., 2021). Unlike those studies, we investigated  $K_{DB}$  and  $K_{IDB}$  in the different damage zone subdomains and the protolith (Fig. 4.11B) and fault facies (Fig. 4.13A). We have also analyzed the permeability of undeformed rocks ( $K_{UR}$ ) distant from any fault zone of the RPB (Fig. 4.11A).

We observed that the deformation bands are always the least permeable elements compared to the interband spaces of the same damage zone subdomain or fault facies. These results are consistent with several previous studies (e.g., Antonellini and Aydin, 1994; Fossen and Bale, 2007; Torabi and Fossen, 2009; Nogueira et al., 2021). Although the average  $K_{DB}$  values are always lower than the  $K_{IDB}$  values, when comparing the different damage zone subdomains (Fig. 4.11A) and fault facies (Fig. 4.13A), the  $K_{IDB}$  may show similar reductions with respect to permeability of  $K_{UR}$  and facies  $N_{DB}$ .  $K_{IDB}$  reductions of up to 1.0 order of

magnitude compared to undeformed rocks have been reported in normal fault zones in Northern Sarawak in Malaysia by Sorkhabi and Hasegawa (2005). According to these authors, the  $K_{IDB}$  reductions are likely to occur through tectonic compaction, even where deformation bands are not observed.

The  $K_{DB}$  and  $K_{IDB}$  reductions with respect to the  $K_{UR}$  (Figs. 11C, D) and  $N_{DB}$  fault facies (Figs. 13B, C) vary with distance from the fault core, with the most deformed subdomains and fault facies (close to the fault core) showing the greatest permeability reductions. These observations agree with the results presented by Alikarami et al. (2013). These authors suggested an inverse relationship between permeability and compressive strength of rocks in the fault damage zones located in San Rafael Swell (Utah-USA) and Cache Valley (Utah), changing these properties with the type of structure (deformation bands or fractures) and deformation density (DB/m).

Results similar to those of Alikarami et al. (2013) were presented by Pontes et al. (2019) that analyzed two fault zones and their protolith in the RPB. One of these faults is a single fault zone associated with moderate deformation, and the other a complex fault zone with intense deformation and several fault cores. In the latter, Pontes et al. (2019) suggested a direct relationship between the deformation intensity and the increase in Uniaxial Compressive Strength (UCS measure) associated with an increase in the degree of cataclasis and reduced porosity in these areas (Araújo et al., 2018; Pontes et al., 2019; Nogueira et al., 2021; and this study). Moreover, Pontes et al. (2019) observed that the deformation bands are always the elements with the highest UCS values in the analyzed areas, considering the high degree of cataclasis and low porosities associated with these structures (Nogueira et al., 2021). However, Pontes et al. (2019) observed that UCS values in the deformation band interspace also increase with the deformation complexity of the zone. Debenham et al. (2019) inferred that clays and

fine sandstones near the fault core in the Castle Cove Fault (Otway Basin) are associated with individual grain cataclasis and may negatively influence the petrophysical properties of the host rock or space between brittle structures.

Based on the discussion above, we infer that the  $K_{DB}$  and  $K_{IDB}$  and their contrasts in regards to the  $K_{UR}$  or the  $N_{DB}$  facies permeability (Figs. 11 and 13) vary with the distance from the fault core due to different deformation intensities (Figs. 7 and 9B). The inner and outer damage zones are associated with greater complexity and deformation ( $H_{DB}$  and  $M_{DB}$  facies) (Figs. 7, 9A, and 15A), which causes the largest  $K_{IDB}$  reductions in orders of magnitude compared to the  $K_{UR}$  or the  $N_{DB}$  facies permeability. In addition, the  $K_{IDB}$  values in the inner damage zone can be smaller in this subdomain due to the more intense tectonic deformation and the influence of lithology, where this zone is predominantly composed of fine sandstones. According to these findings, Del Sole et al. (2020) showed a direct relationship between the grain size of the host rock and the permeability from observation in the Northern Apennines (Italy), where the smaller grain size, lower permeability, and vice versa.

Regardless of the approach, damage zones, or fault facies, there is a relationship between deformation band intensity and the  $K_{DB}$  and  $K_{IDB}$  crossing the hanging wall damage zone of the Malta Fault (Fig. 4.15). Hence, as the deformation band intensity decays with the distance from the fault core, through a logarithmic function,  $F = 30 - 5.6 \ln(d)$  (Fig. 4.15B), the permeabilities grows exponentially with the distance from the fault core ( $d$ ), following the  $K_{IDB} = 19.9 e^{0.02d}$  ( $R^2 = 0.51$ ) (Fig. 4.15C) and  $K_{DB} = 26.7e^{0.007d}$  ( $R^2 = 0.50$ ) (Fig. 4.15D). Thus,  $K_{DB}$  and  $K_{IDB}$  correlations can be complex and variable across fault damage zones.

Rotevatn and Fossen (2011), Fachri et al. (2013a, 2013b), and Qu and Tveranger (2016) observed that the reduction of the  $K_{DB}$  compared to the  $K_{IDB}$ , or permeability of the host rock, is one of the parameters with the most significant impact on fluid flow in porous media since



the reduction in  $K_{DB}$  is followed by the decrease in the equivalent permeability ( $K_{EQ}$ ). However, in the Malta Fault damage zones, in addition to observing that  $K_{DB}$  and  $K_{IDB}$  are variable depending on the distance to fault core or damage zone subdomains and fault facies, they also have variable reductions relative to the  $K_{UR}$ . The contrasts of the  $K_{DB}$  regarding the  $K_{IDB}$  of the same zone or fault facies (Figs. 11A and 13A) showed reductions of at most 2.0 orders of magnitude, related to the fact that both permeabilities can have reductions of the same order of magnitudes compared to the  $K_{UR}$  (Figs. 11C, D, and 13B, C). These results differ from the logic used to assign the input parameters for the modeling of damage zones, used in several studies (Fachri et al., 2011, 2013a, 2013b; Rotevatn and Fossen, 2011; Qu and Tveranger, 2016), where the host rock permeability as well as the  $K_{DB}/K_{IDB}$  relationships are considered to be constant.. Therefore, with the increase in the contrast of  $K_{DB}$  regarding  $K_{IDB}$ , the  $K_{EQ}$  reductions are observed, and consequently, more significant impacts are related to these reductions. However, from our analyses, we infer that the most important factors in the quantification and modeling of  $K_{EQ}$  in damage zones, and consequently to studies the reservoir's impacts, are to determine: (1) the deformation intensities and their distributions along the fault zones (Figs. 7, 8A, B, and 10); (2) the permeability of the main structures and host rocks (interband space in this study) internally in the architectural elements of the fault zones (e.g., damage zones) or the fault facies, and their respective models (Figs. 12A, B, 14A, B).

From the models of  $K_{EQ(x)}$  and  $K_{EQ(y)}$  conditioned the damage zones (Fig. 4.12C, D) and fault facies (Fig. 4.14C, D), we observed similar distributions for these two properties or absolute values nearby (Table 5). However, the magnitude (absolute value) of the  $K_{EQ(x)}$  and  $K_{EQ(y)}$  tensors varied significantly over the hanging wall damage zone subdomains (Fig. 4.15A). We associate this variation with the deformation intensity, which has implications for  $K_{DB}$  and  $K_{IDB}$ . Consequently, the  $K_{IDB}$  influences the calculation of  $K_{EQ}$  perpendicular and parallel to

the main fault (Fig. 4.15A). In the permeability models presented by Qu and Tveranger (2016), the  $K_{EQ}$  parallel to the main fault for the H facies is 457.0 mD, considered an intensity of deformation bands perpendicular to the main fault of 6 DB/m,  $K_{DB} = 10.0$  mD, and  $K_{IDB} = 1000.0$  mD. Compared with the results observed by Qu and Tveranger (2016), our results show lower values of the equivalent permeability parallel to the main fault for the permeability of the  $H_{DB}$  facies, on average 10.0 mD (Table 5). We suggest that the reductions of up to 3.0 orders in the permeability of interband spaces were responsible for this difference. Therefore, the  $K_{EQ}$  (parallel to the fault) in the damage zones can be overestimated when uniform parameters or permeabilities are assigned to the elements and host rocks of the damage zones. We also observed that the greatest anisotropy of equivalent permeabilities occurs in the transitional zone (Figs. 12E and 15A) compared to the more complex zones exhibiting higher deformation intensity (inner and outer damage zones). These results may be linked to the sampling bias, considering that all measurements were taken parallel to the deformation bands dip. This anisotropy may be greater from measurements perpendicular to the strike and dip of the deformation bands and in these same directions in the interband space (e.g., Antonellini and Aydin, 1994; Farrel et al., 2014).

Finally, when analyzing the  $K_{DB}$  and  $K_{IDB}$  and calculating the equivalent permeabilities using two approaches, fault facies, and damage zone subdomains, we observed that: (1) both approaches showed similar equivalent permeability distributions, but the permeability variations associated with deformation intensities in each zone are rendered in higher detail using the fault facies (Fig. 4.14); (2) as the permeability reductions are associated with distance to the fault, models employing damage zone subdomains becomes preferable in addition to being more systematic for application in reservoir modeling, as it provides a more efficient constrain for permeability ranges (Fig. 4.14E); (3) the  $I_{DB}$  values vary in each of the facies

according to the subdomains/distance from the fault core (Fig. 4.9A) which associates a large range and permeability variability in these fault facies (Fig. 4.13A). Thus, in order to produce more representative equivalent permeability models, we suggest that the permeability variation of fault damage zone elements (e.g., deformation bands and interband spaces) in relation to the distance from the fault core must be considered. In addition, the damage zone architectural element must be considered because these are associated with different deformation backgrounds ( $I_{DB}$ ) that influence  $K_{DB}$  and  $K_{IDB}$ .

Other parameters can change equivalent permeabilities along fault zones and, consequently, influence fluid flow in porous media (e.g., Awdal et al., 2020). For example, Balsamo et al. (2012) showed that diagenetic carbonate concretions form as a result of permeability alterations affecting fluid flow in fault zones. Awdal et al. (2020) showed that the heterogeneous deformation band distribution vertically and laterally, has strong implications for fluid flow parameters, and Wilson et al. (2021) showed that through topological analysis, the connectivity of structures could also impact the fluid flow.

### *5.3. Implications for CO<sub>2</sub> and petroleum reservoirs characterizations*

The workflow used in this study (Fig. 4A) can be applied to the characterization and modeling of subsurface fault zones. Moreover, the delimitation of the damage zones and fault facies boundaries in the subsurface can be further constrained with the use of seismic attributes (e.g., Botter et al., 2016a; Torabi et al., 2016; Alaei and Torabi, 2017; Botter et al., 2017; Botter and Champion, 2019; Ma et al., 2019; Liao et al., 2020a, 2020b), whereas the properties of the fault zones can be obtained from well cores, outcrops, and data integration (e.g., Qu and Tveranger., 2016; Wilkins et al., 2019; Liao et al., 2020a; Torabi et al., 2020b).

Based on observations made on the hanging wall damage zone of the Malta Fault in the RPB, regarding the distribution of the deformation bands and their characteristics along the damage zones of this fault, and the  $K_{DB}$ ,  $K_{IDB}$ , and  $K_{EQ}$  perpendicular and parallel to the main fault, we infer that the principal implications of our results for the characterization and modeling of siliciclastic reservoirs are the following: (1) the heterogeneity of permeabilities ( $K_{DB}$ ,  $K_{IDB}$ ,  $K_{EQ}$ ) in the different damage zones, transitional and protolith zones (Fig. 4.15) can lead to different behaviors of these zones when subjected to stress by  $CO_2$  injection. According to Torabi et al. (2015), the characterization of permeability and resistance in non-deformed and deformed sandstones is essential for predicting rock behavior with  $CO_2$  injection. Therefore, characterizing the distribution of these deformation bands (Figs. 7, 10, and 15A, B) can be of importance to the integrity of the  $CO_2$  reservoirs since fractures generated from the deformation bands (Torabi et al., 2015) can promote the escape of unwanted gas (Bond et al., 2017); (2) Deformation bands in the different damage zones can have distinct influences on  $CO_2$  migration (Torabi et al., 2013; Romano et al., 2020) and hydrocarbon flow (Rotevatn and Fossen, 2011; Qu and Tveranger, 2016). This influence tends to decrease with the distance from the fault core, considering the increase in  $K_{DB}$  towards the protolith (Fig. 4.15C); (3) The presence of minor faults (Fig. 4.15A), such as subseismic faults, can present themselves as local barriers to fluid flow in porous media. According to Torabi et al. (2013), these faults are more efficient barriers than deformation bands and clusters and can lead in extreme cases to a sealing capacity greater than 140 m; (4) The  $K_{IDB}$  can induce the inner and outer damage zones to be large-scale barriers and/or baffles to fluid flow in porous media, given the reductions of up to 3.0 orders of magnitude (Fig. 4.15A) relative to the  $K_{UR}$ . In this context, Nogueira et al. (2021) suggested the presence of an architectural element between deformation bands (interband spaces) identified by protocataclastic texture in deformation bands, which show reductions up to 2.0 orders of magnitude compared to  $K_{UR}$ . We recommend that complementary analyses of rock

PPGEPM – UFCG

textures in the interband spaces across different damage zone subdomains may provide a better understanding of the impact of these zones on fluid migration.

We suggest that the characterization of the permeabilities of the main structures in the damage zones and the host rocks of each architectural or deformational element (fault facies) can lead to more accurate stochastic models for  $K_{EQ}$  (perpendicular and parallel) of subsurface reservoirs. Thus, this characterization can provide a better understanding of the fluid flow in these reservoirs (Caine et al., 1996). For example, Wilkins et al. (2019) showed that the values of equivalent permeabilities obtained through transient pressure analysis (PTA) are lower than those calculated in samples with deformation bands, using a harmonic mean (Equation 1). According to our results, this difference between the equivalent permeabilities can be given by the  $K_{IDB}$  reductions in the damage zones and by the complex relationships between  $K_{DB}/K_{IDB}$  (Fig. 4.15C, D) and  $K_{EQ}$  perpendicular and parallel to these zones. Therefore, the relations of  $K_{DB}$  and  $K_{IDB}$  with the distance from the fault core proposed in this work (Fig. 4.15C, D) and deformation intensity can support the  $K_{EQ}$  modeling along the subsurface damage zones associated with basin-bounding faults, for example.

## 6. Conclusions

Our study presents new data about the characterization and modeling of damage zones, fault facies, and permeability in Cretaceous sandstones on the hanging wall of the main bounding fault segment, the Malta Fault in the RPB, Brazil. Our results support the following conclusions:

1. The main structures developed in the damage zones on the hanging wall of the Malta Fault were deformation bands parallel to the main WNW-ESSE-striking fault, and minor synthetic and antithetic faults with small displacement and length.

2. We identified inner and outer damage zones and a transitional zone; the total width of these zones is approximately 200 m. They were determined from the deformation band accumulated frequency, measured from the fault core toward the protolith.

3. The deformation intensity represented by fault facies was heterogeneously distributed across the different damage zone subdomains. The most deformed facies ( $H_{DB}$  and  $M_{DB}$ ) are concentrated along the inner and outer damage zones, and the less deformed facies ( $L_{DB}$  and  $N_{DB}$ ) mainly occur in the transitional zone and the protolith.

4. The minor faults in the damage zones, identified from the small fluctuations in the deformation band accumulated frequency curve, or polymodal pattern in the frequency bar graph, were also represented in the contacts of fault facies of  $H_{DB}$ - $L_{DB}$  and  $M_{DB}$ - $N_{DB}$  types.

5. The variation of deformation intensity led to different permeabilities in the deformation bands ( $K_{DB}$ ) and the interband space ( $K_{IDB}$ ) along the damage zone subdomains and the protolith. Both permeabilities increase from the most deformed zone (inner damage zone) to the protolith. Likewise, the fault facies also show an increasing permeability trend in the  $K_{DB}$  and the  $K_{IDB}$ , from the  $H_{DB}$  facies toward  $N_{DB}$  facies.

6. The deformation bands have permeability ( $K_{DB}$ ) lower than the average permeability of the interband space ( $K_{IDB}$ ) in the same fault facies or damage zones. However, both deformation bands ( $K_{DB}$ ) and interband ( $K_{IDB}$ ) show reductions up to 3.0 orders of magnitude related the same features in the undeformed rocks ( $K_{UR}$ ).

7. Characterizing the permeabilities in the interband space ( $K_{IDB}$ ) is as essential as those of the deformation bands ( $K_{DB}$ ) themselves, as it allows more precise quantification and modeling of the perpendicular and parallel equivalent permeabilities ( $K_{EQ}$ ) along the fault damage zones, given the strong impact of the deformation on both permeabilities.

8. The deformation band frequency on the hanging wall follows a logarithmic decrease while the permeabilities of deformation bands ( $K_{DB}$ ) and interband permeability ( $K_{IDB}$ ) increase exponentially towards the protolith.

9. This work approach uses the deformational characterization and modeling of fault damage zones and, integrated analyses of main permeability elements. They contribute to more effective modeling and quantification of equivalent permeability, fluid flow simulation, and predictive behavior in siliciclastic faulted reservoirs.

### **Acknowledgements**

We are grateful to Dr. Charlotte Botter and Dr. Jan Tveranger for detailed and constructive comments, and the editorial guidance of Marine and Petroleum Geology Associate Editor Dr. Friedemann Baur. Their careful criticism greatly improved this article. We thank Schlumberger for providing Petrel software license to the Federal University of Campina Grande (UFCG). Petrobras funded the DEBRIP Project (TC 5850.0109438.18.9) coordinated by Francisco C. C. Nogueira (UFCG). This project also funded MES MSc, YARP and DLV post-doc grants, and FB visits to Brazil. FHRB thanks the Brazilian Research Council (CNPq) for his productivity grant.

### **References**

- Alaei, B., Torabi, A., 2017. Seismic imaging of fault damaged zone and its scaling relation with displacement. *Interpretation* 5, SP83–SP93. <http://dx.doi.org/10.1190/INT-2016-0230.1>.
- Alikarami, R., Torabi, A., Kolyukhin, D., Skurtveit, E., 2013. *International Journal of Rock Mechanics & Mining Sciences* 63, 27–38. <http://dx.doi.org/10.1016/j.ijrmms.2013.06.002>.
- Antonellini, M., Aydin, A., 1994. Effect of Faulting on Fluid Flow in Porous Sandstones: Petrophysical Properties. *AAPG Bulletin* 78, 355–377.  
PPGEPM – UFCG

Araújo, R. E. B., Bezerra, F. H. R., Nogueira, F. C. C., Balsamo, F., Carvalho, B. R. B. M., Souza, J. A. B., Sanglard, J. C. D., de Castro, D. L., Melo, A. C. C., 2018. Basement control on fault formation and deformation band damage zone evolution in the Rio do Peixe Basin, Brazil. *Tectonophysics* 745, 117–131. <https://doi.org/10.1016/j.tecto.2018.08.011>.

Awdal, A., Suramairy, R., Singh, K., Fabre, G., Alsop, G. I., 2020. Deformation bands and their impact on fluid flow: Insights from geometrical modelling and multi-scale flow simulations in sandstones. *Journal of Structural Geology* 141, 104215. <https://doi.org/10.1016/j.jsg.2020.104215>.

Ballas, G., Fossen, H., Soliva, R., 2015. Factors controlling permeability of cataclastic deformation bands and faults in porous sandstone reservoirs. *Journal of Structural Geology* 76, 1–21. <http://dx.doi.org/10.1016/j.jsg.2015.03.013>.

Balsamo, F., Storti, F., 2010. Grain size and permeability evolution of soft-sediment extensional sub-seismic and seismic fault zones in high-porosity sediments from the Croton basin, southern Apennines, Italy. *Marine and Petroleum Geology* 27, 822–837. <http://dx.doi.org/10.1016/j.marpetgeo.2009.10.016>

Balsamo, F., Storti, F., Grocke., D. R., 2012. Fault-related fluid flow history in shallow marine sediments from carbonate concretions, Croton basin, south Italy. *Journal of the Geological Society, London* 169, 613–626. <http://dx.doi.org/10.1144/0016-76492011-109>.

Balsamo, F., Clemenzi, L., Storti, F., Solum, J., Taberner, C., 2019. Tectonic control on vein attributes and deformation intensity in fault damage zones affecting Natih platform carbonates, Jabal Qusaybah, North Oman. *Journal of Structural Geology* 122, 38–57. <https://doi.org/10.1016/j.jsg.2019.02.009>.



Berg, S. S., Skar, T., 2005. Controls on damage zone asymmetry of a normal fault zone: outcrop analyses of a segment of the Moab fault, SE Utah. *Journal of Structural Geology* 27, 1803–1822. <http://dx.doi.org/10.1016/j.jsg.2005.04.012>.

Bistacchi, A., Mittempergher, S., Martinelli, M., Storti, F., 2020. On a new robust workflow for the statistical and spatial analysis of fracture data collected with scanlines (or the importance of stationarity). *Solid Earth*, 2535–2547. <https://doi.org/10.5194/se-11-2535-2020>.

Bond, C. E., Kremer, Y., Johnson, G., Hicks, N., Lister, R., Jones, D. G., Haszeldine, R. S., Saunders, I., Gilfillan, S. M. V., Shipton, Z. K., Pearce, J., 2017. The physical characteristics of a CO<sub>2</sub> seeping fault: The implications of fracture permeability for carbon capture and storage integrity. *International Journal of Greenhouse Gas Control* 60, 49–60. <http://dx.doi.org/10.1016/j.ijggc.2017.01.015>.

Botter, C., Cardozo, N., Hardy, S., Lecomte, I., Paton, G., Escalona, A., 2016a. Seismic characterization of fault damage in 3D using mechanical and seismic modelling. *Marine and Petroleum Geology* 77, 973–990. <http://dx.doi.org/10.1016/j.marpetgeo.2016.08.002>.

Botter, C., Cardozo, N., Lecomte, I., Rotevatn, A., Paton, G., 2016b. The impact of faults and fluid flow on seismic images of a relay ramp over production time. *Petroleum Geoscience* 23, 17–28. <https://doi.org/10.1144/petgeo2016-027>.

Botter, C., Cardozo, N., Qu, D., Tveranger, J., Kolyukhin, D., 2017. Seismic characterization of fault facies models. *Interpretation* 5, 1–18. <http://dx.doi.org/10.1190/INT-2016-0226.1>.

Botter, C., Champion, A., 2019. Seismic Fault Damage Zone Characterisation for Reservoir Modelling Using Advanced Attribute Analysis. Fifth International Conference on Fault and Top Seals, Palermo, Italy. <https://doi.org/10.3997/2214-4609.201902317>.

Braathen, A., Tveranger, J., Fossen, H., Skar, T., Cardozo, N., Semshaug, S.E., Bastesen, E., Sverdrup, E., 2009. Fault facies and its application to sandstone reservoirs. *AAPG Bulletin* 93, 891–917. <http://dx.doi.org/10.1306/03230908116>.

Caine, J. S., Evans, J. P., Forster, C. B., 1996. Fault zone architecture and permeability structure. *Geology* 24, 1025–1028. [https://doi.org/10.1130/0091-7613\(1996\)024<1025:FZAAPS>2.3.CO;2](https://doi.org/10.1130/0091-7613(1996)024<1025:FZAAPS>2.3.CO;2).

Cardwell, W. T., Parsons, R. I., 1945. Average permeability of heterogeneous sands. *Transactions of the American Institute of Mining Engineers* 160, 34–42.

Carvalho, I. S., Mendes, J. C., Costa, T., 2013. The role of fracturing and mineralogical alteration of basement gneiss in the oil exudation in the Sousa Basin (Lower Cretaceous), Northeastern Brazil. *Journal of South American Earth Sciences* 47, 47–54. <https://doi.org/10.1016/j.jsames.2013.06.001>.

Celestino, M. A. L., Miranda, T. S., Mariano, G., Lima, M. A., Carvalho, B. R. B. M., Falcão, T. C., Topan, J. G., Barbosa, J. A., Gomes, I. F., 2020. Fault damage zones width: Implications for the tectonic evolution of the northern border of the Araripe Basin, Brazil, NE Brazil. *Journal of Structural Geology* 138, 104116. <https://doi.org/10.1016/j.jsg.2020.104116>.

Childs, C., Manzocchi, T., Walsh, J. J., Bonson, C. G., Nicol, A., Schöpfer, M. P. J., 2009. A geometric model of fault zone and fault rock thickness variations. *Journal of Structural Geology* 31, 117–127. <https://doi.org/10.1016/j.jsg.2008.08.009>.

Choi, J. H., Edwards, P., Ko, K., Kim, Y. S., 2016. Definition and classification of fault damage zones: A review and a new methodological approach. *Earth-Science Reviews* 152, 70–87. <http://dx.doi.org/10.1016/j.earscirev.2015.11.006>.

de Castro, D. L., Oliveira, D. C., Castelo Branco, R. M. G., 2007. On the tectonics of the Neocomian Rio do Peixe rift basin, NE Brazil: lessons from gravity, magnetic and radiometric data. *Journal of South American Earth Sciences* 24, 184–202. <https://doi.org/10.1016/j.jsames.2007.04.001>.

de Souza, D.H.S., Nogueira, F.C.C., Vasconcelos, D.L., Torabi, A., Souza, J.A.B., Nicchio, M.A., Pérez, Y.A.R., Balsamo, F., 2021. Growth of cataclastic bands into a fault zone: A multiscale process by microcrack coalescence in sandstones of Rio do Peixe Basin, NE Brazil. *Journal of Structural Geology* 146, 104315. <https://doi.org/10.1016/j.jsg.2021.104315>.

Debenham, N., Farrell, N. J. C., Holford, S. P., King, R. C., Healy, D., 2019. Spatial distribution of micrometre-scale porosity and permeability across the damage zone of a reverse-reactivated normal fault in a tight sandstone: Insights from the Otway Basin, SE Australia. *Basin Research* 31, 640–658. <https://doi.org/10.1111/bre.12345>.

Del Sole, L., Antonellini, M., Calafato, A., 2020. Characterization of sub-seismic resolution structural diagenetic heterogeneities in porous sandstones: Combining ground-penetrating radar profiles with geomechanical and petrophysical *in situ* measurements (Northern Apennines, Italy). *Marine and Petroleum Geology* 117, 104375. <https://doi.org/10.1016/j.marpetgeo.2020.104375>.

Dershowitz W. S., Herda, H. H., 1992. Interpretation of fracture spacing and intensity. 33<sup>rd</sup> U.S. Symposium Rock Mechanics, 757–766.

Deutsch, C. V., Journel, A. G., 1998. *Geostatistical Software Library and User's Guide*. Oxford University Press 2, 1–352.

Fachri, M., Tveranger, J., Cardozo, N., Pettersen, O., 2011. The impact of fault envelop structure on fluid flow: A screening study using fault facies. *AAPG Bulletin* 95, 619–648. <http://dx.doi.org/10.1306/09131009132>.

Fachri, M., Tveranger, J., Braathen, A., Schueller, S., 2013a. Sensitivity of fluid flow to deformation-band damage zone heterogeneities: A study using fault facies and truncated Gaussian simulation. *Journal of Structural Geology* 52, 60–79. <http://dx.doi.org/10.1016/j.jsg.2013.04.005>.

Fachri, M., Rotevatn, A., Tveranger, J., 2013b. Fluid flow in relay zones revisited: Towards an improved representation of small-scale structural heterogeneities in flow models. *Marine and Petroleum Geology* 46, 144–164. <http://dx.doi.org/10.1016/j.marpetgeo.2013.05.016>.

Farrel, N. J. C., Healy, D., Taylor, C. W., 2014. Anisotropy of permeability in faulted porous sandstones. *Journal of Structural Geology* 63, 50–67. <http://dx.doi.org/10.1016/j.jsg.2014.02.008>.

Faulkner, D. R., Jackson, C. A. L., Lunn, R. J., Schlische, R. W., Shipton, Z. K., Wibberley, C. A. J., Withjack, M. O., 2010. A review of recent developments concerning the structure, mechanics and fluid flow properties of fault zones. *Journal of Structural Geology* 32, 1557–1575. <https://doi.org/10.1016/j.jsg.2010.06.009>.

Fossen, H., Bale, A., 2007. Deformation bands and their influence on fluid flow. *AAPG Bulletin* 91, 1685–1700. <https://doi.org/10.1306/07300706146>.

Fossen, H., Schultz, R. A., Shipton, Z. K., Karen, M., 2007. Deformation bands in sandstone: a review. *Journal of Geological Society (London)* 164, 755–769. <https://doi.org/10.1144/0016-76492006-036>.

Fossen, H., Soliva, R., Ballas, G., Trzaskos, B., Cavalcante, C., Schultz, R. A., 2017. A review of deformation bands in reservoir sandstones: geometries, mechanisms and distribution. *Journal of Geological Society (London)* 459, 9–33. <https://doi.org/10.1144/SP459.4>.

Journel, A. G., Isaaks, E., 1984. Conditional indicator simulation: application to a Saskatchewan uranium deposit. *Mathematical Geology* 16, 685–718. <https://doi.org/10.1007/BF01033030>.

Liao, Z., Chen, W., Chen, X., Zhou, Y., Hao, F., 2020a. Multiscale fracture and damage zone characterization in a tight sandstone reservoir, Sichuan Basin, China. *Interpretation* 8, 1–11. <http://dx.doi.org/10.1190/INT-2019-0107.1>.

Liao, Z., Hu, L., Huang, X., Carpenter, B. M., Marfurt, K. J., Vasileva, S., Zhou, Y., 2020b. Characterizing damage zones of normal faults using seismic variance in the Wangxuzhuang oilfield, China. *Interpretation* 8, 1–8. <http://dx.doi.org/10.1190/INT-2020-0004.1>.

Ma, D. B., Wu, G. H., Scarselli, N., Luo, X. S., Han, J. F., Chen, Z. Y., 2019. Seismic damage zone and width-throw scaling along the strike-slip faults in the Ordovician carbonates in the Tarim Basin. *Petroleum Science* 16, 752–762. <https://doi.org/10.1007/s12182-019-0352-4>.

Maciel, I. B., Dettori, A., Balsamo, F., Bezerra, F. H. R., Vieira, M. M., Nogueira, F. C. C., Salvioli-Mariani, E., Sousa, J. A. B., 2018. Structural Control on Clay Mineral Authigenesis in Faulted Arkosic Sandstone of the Rio do Peixe Basin, Brazil. *Minerals* 8, 1–17. <https://doi.org/10.3390/min8090408>.

Maerten, L., Gillespie, P., Daniel, J. M., 2006. Three-dimensional geomechanical modelling for constraint of subseismic fault simulation. *AAPG Bulletin* 90, 1337–1358. <https://doi.org/10.1306/03130605148>.

Manzocchi, T., Walsh, J. J., Nell, P., Yielding, G., 1999. Fault transmissibility multipliers for flow simulation models. *Petroleum Geoscience* 5, 53–63. <https://doi.org/10.1144/petgeo.5.1.53>.

Matheron, G., Beucher, H., de Fouquet, C., Galli, A., Guerillot, D., Ravenne, C., 1987. Conditional Simulation of the Geometry of Fluvio-deltaic Reservoirs. SPE 16753.

Matos, R. M. D., 1992. The northeastern Brazilian Rift System. *Tectonics* 11, 766–791. <https://doi.org/10.1029/91TC03092>.

Mayolle, S., Soliva, R., Caniven, Y., Wibberley, C., Ballas, G., Milesi, G., Dominguez, S., 2019. Scaling of fault damage zones in carbonate rocks. *Journal of Structural Geology* 124, 35–50. <https://doi.org/10.1016/j.jsg.2019.03.007>.

Medeiros, V. C., Amaral, C. A., Rocha, D. E. G. A., Santos, R. B., 2005. Programa Geologia do Brasil - PGB. Sousa. Folha SB.24-Z-A. Estados da Paraíba, Rio Grande do Norte e Ceará. Mapa Geológico. Recife: CPRM, 2005, 1 mapa, color., 66cm x108cm. Escala 1:250.000.

Micarelli, L., Moretti, I., Daniel, J. M., 2003. Structural properties of rift-related normal faults: the case study of the Gulf of Corinth, Greece. *Journal of Geodynamics* 36, 275–303. [https://doi.org/10.1016/S0264-3707\(03\)00051-6](https://doi.org/10.1016/S0264-3707(03)00051-6).

Navabi, S. T., Alavi, S. A., Wibberley, C. A. J., Jahangiri, M., 2020. Normal fault networks and their spatial relationships in Plio-Quaternary sedimentary series: A case study in the Zanzan Depression, NW Iran. *Journal of Structural Geology* 136, 104072. <https://doi.org/10.1016/j.jsg.2020.104072>.

Nicchio, M. A., Nogueira, F. C. C., Balsamo, F., Souza, J. A. B., Carvalho, B. R. B. M., Bezerra, F. H. R., 2017. Development of cataclastic foliation in deformation bands in feldspar-rich

conglomerates of the Rio do Peixe Basin, NE Brazil. *Journal of Structural Geology* 107, 132–141. <https://doi.org/10.1016/j.jsg.2017.12.013>.

Nogueira, F. C. C., Marques, F. O., Bezerra, F. H. R., Fuck, R., 2015. Cretaceous intracontinental rifting and post-rift inversion in NE Brazil: Insights from the Rio do Peixe Basin. *Tectonophysics* 644-645, 92–107. <http://dx.doi.org/10.1016/j.tecto.2014.12.016>.

Nogueira, F. C. C., Nicchio, M. A., Balsamo, F., Souza, J. A. B., Silva, I. V. L., Bezerra, F. H. R., Vasconcelos, D. L., Carvalho, B. R. B. M., 2021. The influence of the cataclastic matrix on the petrophysical properties of deformation bands in arkosic sandstones. *Marine and Petroleum Geology* 134, 104825. <https://doi.org/10.1016/j.marpetgeo.2020.104825>.

Ortega, O. J., Marrett, R. A., Laubach, S. E., 2006. A scale-independent approach to fracture intensity and average spacing measurement. *AAPG Bulletin* 90, 193–208. <http://dx.doi.org/10.1306/08250505059>.

Pizzati, M., Balsamo, F., Storti, F., 2020. Displacement-dependent microstructural and petrophysical properties of deformation bands and gouges in poorly lithified sandstone deformed at shallow burial depth (Crotone Basin, Italy). *Journal of Structural Geology* 137, 104069. <https://doi.org/10.1016/j.jsg.2020.104069>.

Pontes, C. C. C., Nogueira, F. C. C., Bezerra, F. H. R., Balsamo, F., Miranda, T.S., Nicchio, M. A., Souza, J. A. B., Carvalho, B. R. B. M., 2019. Petrophysical properties of deformation bands in high porous sandstones across fault zones in the Rio do Peixe Basin, Brazil. *International Journal of Rock Mechanics and Mining Sciences* 114, 153–163. <https://doi.org/10.1016/j.ijrmms.2018.12.009>.

Qu, D., Tveranger, J., 2016. Incorporation of deformation band fault damage zones in reservoir models. *AAPG Bulletin* 100, 423–443. <https://doi.org/10.1306/12111514166>.

Qu, D., Tveranger, J., Fachri, M., 2017. Influence of deformation-band fault damage zone on reservoir performance. *Interpretation* 5, 41–56. <http://dx.doi.org/10.1190/INT-2016-0229>.

Roesner, H. E., Lana, C. C., Le Herissé, A., & Melo, J. H. G., 2011. Bacia do Rio do Peixe (PB). Novos resultados biocronoestratigráficos e paleoambientais. In I. S. Carvalho, N. K. Srivastava, O. Strohschoen Jr, & C. C. Lana (Eds.), *Paleontologia: Cenários de Vida*, 3. Rio de Janeiro. Interciência 135–141.

Romano, C. R., Zahasky, C., Garing, C., Minto, J. M., Benson, S. M., Shipton, Z. K., Lunn, R. J., 2020. Subcore Scale Fluid Flow Behavior in a Sandstone With Cataclastic Deformation Bands. *Water Resources Research American Geophysical Union (AGU)* 56, 10–20. <http://dx.doi.org/10.1029/2019wr026715>.

Rotevatn, A., Fossen, H., 2011. Simulating the effect of subseismic fault tails and process zones in a siliciclastic reservoir analog: Implications for aquifer support and trap definition. *Marine and Petroleum Geology* 28, 1648–1662. <https://doi.org/10.1016/j.marpetgeo.2011.07.005>.

Rotevatn, A., Tveranger, J., Howell, J. A., Fossen, H., 2009. Dynamic investigation of the effect of a relay ramp on simulated fluid flow: geocellular modelling of the Delicate Arch Ramp, Utah. *Petroleum Geoscience* 15, 45–58. <https://doi.org/10.1144/1354-079309-779>.

Schueller, S., Braathen, A., Fossen, H., Tveranger, J., 2013. Spatial distribution of deformation bands in damage zones of extensional faults in porous sandstones: Statistical analysis of field data. *Journal of Structural Geology* 52, 148–162. <http://dx.doi.org/10.1016/j.jsg.2013.03.013>.

Sénant, J., Popoff, M., 1991. Early Cretaceous extension in northeast Brazil related to the South Atlantic opening. *Tectonophysics* 198, 35–46. [https://doi.org/10.1016/0040-1951\(91\)90129-G](https://doi.org/10.1016/0040-1951(91)90129-G).

Shedid, S.A., 2019. Vertical-horizontal permeability correlations using coring data. *Egyptian Journal of Petroleum* 28 (1), 97–101. <https://doi.org/10.1016/j.ejpe.2018.12.007>.  
PPGEPM – UFCG



Shipton, Z. K., Cowie, P. A., 2001. Damage zone and slip-surface evolution over  $\mu\text{m}$  to km scales in high-porosity Navajo sandstone, Utah. *Journal of Structural Geology* 23, 1825–1844. [https://doi.org/10.1016/S0191-8141\(01\)00035-9](https://doi.org/10.1016/S0191-8141(01)00035-9).

Shipton, Z. K., Evans, J. P., Thompson, L.B., 2005. The Geometry and Thickness of Deformation-band Fault Core and its Influence on Sealing Characteristics of Deformation-band Fault Zones. *AAPG Memoir* 85, 181–195. <https://doi.org/10.1306/1033723M853135>.

Silva, J. G. F., Córdoba, V. C., Caldas, L. H. C., 2014. Proposta de novas unidades litoestratigráficas para o Devoniano da Bacia do Rio do Peixe, Nordeste do Brasil. *Brazilian Journal of Geology* 44, 561–578. <https://doi.org/10.5327/Z23174889201400040004>.

Soliva, R., Ballas, G., Fossen, H., Philip, S., 2016. Tectonic regime controls clustering of deformation bands in porous sandstone. *Geology* 44, 423–426. <https://doi.org/10.1130/G37585.1>.

Sorkhabi, R., Hasegawa, S., 2005. Fault Zone Architecture and Permeability Distribution in the Neogene Clastics of Northern Sarawak (Miri Airport Road Outcrop), Malaysia. *AAPG Memoir* 85, 139–151. <https://doi.org/10.1306/1033721M853128>.

Souza, F. M., Gomes, I. F., Nogueira, F. C. C., Vasconcelos, D. L., Canabarro, B., Souza, J. A. B., Guimarães, L. J. N., Beserra, L. B. S., 2022. 2D modeling and simulation of deformation bands' effect on fluid flow: Implications for hydraulic properties in siliciclastic reservoirs. *Journal of Structural Geology* 158, 104581. <https://doi.org/10.1016/j.jsg.2022.104581>.

Stohler, R. C., 2021. Modelagem numérica 3D do impacto de bandas de deformação no fluxo de escoamento em meio poroso. Rio de Janeiro, 2021. xix, 208 f. Dissertação – Programa de Pós-graduação em Geologia, Instituto de Geociências, Universidade Federal do Rio de Janeiro.

Torabi, A., Fossen, H., 2009. Spatial variation of microstructure and petrophysical properties along deformation bands in reservoir sandstones. *AAPG Bulletin* 93, 919–938. <https://doi.org/10.1306/03270908161>.

Torabi, A., Berg, S. S., 2011. Scaling of fault attributes: A review. *Marine and Petroleum Geology* 28, 1444–1460. <https://doi.org/10.1016/j.marpetgeo.2011.04.003>.

Torabi, A., Fossen, H., Braathen, A., 2013. Insight into petrophysical properties of deformed sandstone reservoirs. *AAPG Bulletin* 97, 619–637. <https://doi.org/10.1306/10031212040>.

Torabi, A., Gabrielsen, R. H., Fossen, H., Ringrose, P., Skurtveit, E., Ando, E., Marinelli, F., Viggiani, G., Dal Point, S., Braathen, A., Hovland, A., Bésuelle, P., Alikarami, R., Zalmstra, H., Sokoutis, D., 2015. Strain localization in sandstone and its implications for CO<sub>2</sub> storage. *First break* 33, 81–92.

Torabi, A., Alaei, B., Kolyukhin, D., 2016. Analysis of fault scaling relations using fault seismic attributes. *Geophysical Prospecting* 65, 581–595. <https://doi.org/10.1111/1365-2478.12440>.

Torabi, A., Johannessen, M. U., Ellingsen, T. S. S., 2019. Fault core Thickness: Insights from siliciclastic and Carbonate Rocks. *Geofluids* 2019, 1–24. <https://doi.org/10.1155/2019/2918673>.

Torabi, A., Ellingsen, T. S. S., Johannessen, M. U., Alaei, B., Rotevatn, A., Chiarella, D., 2020a. Fault zone architecture and its scaling laws: where does the damage zone start and stop? *Geological Society, London, Special Publications*, 496, 99–124. <https://doi.org/10.1144/SP496-2018-151>.

Torabi, A., Millán, J. J., Espinosa, R. J., Tortosa, F. J. G., Abad, I., Ellingsen, T. S. S. 2020b. Effect of Mineral Processes and Deformation on the Petrophysical Properties of Soft Rocks during Active Faulting. *Minerals* 10, 444–472. <https://doi.org/10.3390/min10050444>.  
PPGEPM – UFCG

Tveranger, J., Braathen, A., Skar, T., 2004. Incorporation of fault zones as volumes in reservoir models. *Bolletino di Geofisica Teoretica et Applicata* 45, 316–318.

Tveranger, J., Braathen, A., Skar, T., Skauge, A., 2005. Centre for Integrated Petroleum Research: Research activities with emphasis on fluid flow in fault zones. *Norwegian Journal of Geology* 85, 179–187.

Vasconcelos, D., Marques, F. O., Nogueira, F. C. C., Perez, Y. A. R., Bezerra, F. H. R., Stohler, R. C., Souza, J. A. B., 2021. Tectonic inversion assessed by integration of geological and geophysical data: The intracontinental Rio do Peixe Basin, NE Brazil. *Basin Research* 33, 705–728. <https://doi.org/10.1111/bre.12491>.

Wibberley, C. A. J., Pettit, J. P., Rives, T., 2007. The mechanics of fault distribution and localization in high-porosity sands, Provence, France. Geological Society, London, Special Publications 289, 19–46. <https://doi.org/10.1144/SP289.3>.

Wilkins, S. J., Davies, R. K., Naruk, S.J., 2019. Subsurface Observations of Deformation Bands and Their impact on Hydrocarbon Production Within the Holstein field, Gulf Of Mexico, USA. Geological Society, London, Special Publications 496, 223–252. <https://doi.org/10.1144/SP496-2018-139>.

Wilson, P. I. R., Wilson, R. W., Sanderson, D. J., Jarvis, I., McCaffrey, K. J. W., 2021. Analysis of deformation bands associated with the Trachyte Mesa intrusion, Henry Mountains, Utah: implications for reservoir connectivity and fluid flow around sill intrusions. *Solid Earth* 12, 95–117. <https://doi.org/10.5194/se-12-95-2021>.

# *Capítulo. 5*

## *Conclusões*

## 5. Conclusões e Sugestões para Trabalhos Futuros

Acerca dos resultados apresentados é possível realizar algumas conclusões a respeito da arquitetura do segmento estudado da Falha Malta na BRP e distribuição de estruturas ou intensidade de deformação (BD/m) e permeabilidades nos arenitos cretáceos no *hangingwall* desta falha. Na área de estudo, a Zona de Falha Malta é composta por três elementos arquiteturais, denominados núcleo de falha, zonas de dano e protólito. De modo que, nós identificamos que as zonas de dano no *footwall* são compostas por milonitos fraturados do embasamento cristalino Pré-cambriano. O núcleo desta falha, de ~ 12–20 m, compreende gouge, cataclasitos e brechas. E o *hangingwall* é composto predominantemente por BD (E-W, paralela ao plano da falha principal), e em menor quantidade falhas de pequenos rejeitos e comprimento, sintéticas e antitéticas a falha principal. No que se refere a delimitação de subdomínios para as zonas de dano no *hangingwall* da zona de falha estudada, foi possível identificar a partir da frequência acumulada de BD com a distância do núcleo da falha a presença de duas zonas de dano (interna e externa) e uma zona transicional, compreendidas entre o núcleo da falha principal e o protólito, cujas espessuras foram de 12m, ~80m e ~108 m, respectivamente.

Em adição, foi possível observar que as intensidades de deformação (fácies de falha) se distribuem de formas distintas ao longo dos contornos dos diferentes subdomínios das zonas de dano, onde as fácies mais deformadas ( $H_{BD}$  e  $M_{BD}$ ) se concentram predominantemente ao longo das zonas de dano interna e externa, próximas ao núcleo da falha, enquanto as fácies menos deformadas ( $L_{BD}$  e  $N_{BD}$ ) distribuem-se principalmente ao longo da zona transicional e do protólito. As falhas de pequeno rejeito e comprimento presentes nas zonas de dano, além de serem identificadas a partir de pequenas flutuações na curva de frequência acumulada de BD, ou padrão polimodal no gráfico de barras, foram identificadas nesse estudo associadas aos

contatos laterais de fácies de falha do tipo  $H_{BD}$ – $L_{BD}$ , o que tornou possível a identificação dessas facilmente a partir do modelo de fácies de falha do afloramento. As zonas de dano interna e externa, transicional e protólito concentram intensidades de deformação diferentes, que conseqüentemente levaram a permeabilidades distintas tanto para as BD quanto para o espaço entre BD nessas zonas. Desse modo, foi possível observar nas zonas de dano da Falha Malta uma relação crescente de ambas as permeabilidades da zona mais deformada (zona de dano interna) para a menos deformada (protólito). No entanto, a zona de dano interna evidenciou grande similaridade dos valores das permeabilidades das BD e dos espaços entre bandas, que podem estar associados a uma cataclase do próprio arenito presente nessa zona, que apresenta uma textura bem diferenciada dos demais. Similarmente as zonas, as fácies de falha também mostram uma tendência crescente das permeabilidades das BD e entre BD da fácies  $H_{BD}$  para a  $N_{BD}$ .

Finalmente, as BD mostraram-se como os elementos de menor permeabilidade comparadas a permeabilidade entre bandas, em uma mesma fácies de falha ou zonas/subdomínios. No entanto, tanto as BD quanto o espaço entre bandas de BD apresentaram reduções de até três ordens de magnitude nas zonas e fácies mais deformadas. Assim, nós concluímos que caracterizar as permeabilidades no espaço interbanda é tão importante quanto as das próprias BD para a quantificação da permeabilidade efetiva ao longo das zonas de dano de uma falha, visto o forte impacto da deformação em ambas as permeabilidades. No entanto, essas relações podem ser complexas, visto que essas se mostraram muito variáveis ao longo da zona de falha estudada, tal que, as frequências das BD no *hangingwall* da falha principal seguem um decaimento logarítmico com a distância do núcleo da falha, enquanto as permeabilidades das BD e do espaço entre BD aumentam de forma exponencial com a distância desse.

Para além da temática levantada e respondida com esta dissertação, são sugeridos os seguintes estudos complementares: (1) Estudo sistemático do espaçamento das BD a fim de determinar qual o padrão de distribuição das BD na zona de falha estudada (larga escala, repetição de clusters, repetição de núcleos etc.); e assim responder qual a relação desse padrão de distribuição de BD com a distribuição das propriedades petrofísicas? Uma lacuna científica sugerida para essa abordagem é: como é possível modelar de forma mais eficiente e com maior representatividade essas distribuições a fim de compreender o fluxo de fluidos nessas zonas? (2) Estudo da porosidade, usando seções delgadas e geração de modelos dessa propriedade; (3) Estudo petrográfico a partir de seções delgadas da zona de dano interna, a fim de responder se a textura distinta desse arenito é proveniente da deformação atuante (cataclase individual de grãos) ou sua origem é puramente sedimentar; (4) Delimitação das zonas de dano no *footwall* da zona de falha estudada, fazendo o uso de dados de *scanlines* levantados no embasamento cristalino; (5) Simulação de fluxo de fluidos integrada ao estudo de disposição de poços internamente as zonas de dano; visando responder se a disposição dos poços de injeção e produção em zonas de falhas com padrão de distribuição de BD em larga-escala, com *minor faults*, influencia o fator de recuperação e como influenciam.

**Referencias**

Alaei, B., Torabi, A., 2017. Seismic imaging of fault damaged zone and its scaling relation with displacement. *Interpretation* 5, SP83–SP93. <http://dx.doi.org/10.1190/INT-2016-0230.1>.

Alikarami, R., Torabi, A., Kolyukhin, D., Skurtveit, E., 2013. *International Journal of Rock Mechanics & Mining Sciences* 63, 27–38. <http://dx.doi.org/10.1016/j.ijrmms.2013.06.002>.

Antonellini, M., Aydin, A., 1994. Effect of Faulting on Fluid Flow in Porous Sandstones: Petrophysical Properties. *AAPG Bulletin* 78, 355–377.

Araujo, R. E. B., Bezerra, F. H. R., Nogueira, F. C. C., Balsamo, F., Carvalho, B. R. B. M., Souza, J. A. B., Sanglard, J. C. D., de Castro, D. L., Melo, A. C. C., 2018. Basement control on fault formation and deformation band damage zone evolution in the Rio do Peixe Basin, Brazil. *Tectonophysics* 745, 117–131. <https://doi.org/10.1016/j.tecto.2018.08.011>.

Awdal, A., Suramairy, R., Singh, K., Fabre, G., Alsop, G. I., 2020. Deformation bands and their impact on fluid flow: Insights from geometrical modelling and multi-scale flow simulations in sandstones. *Journal of Structural Geology* 141, 104215. <https://doi.org/10.1016/j.jsg.2020.104215>.

Ballas, G., Fossen, H., Soliva, R., 2015. Factors controlling permeability of cataclastic deformation bands and faults in porous sandstone reservoirs. *Journal of Structural Geology* 76, 1–21. <http://dx.doi.org/10.1016/j.jsg.2015.03.013>.

Balsamo, F., Storti, F., 2010. Grain size and permeability evolution of soft-sediment extensional sub-seismic and seismic fault zones in high-porosity sediments from the Croton basin, southern Apennines, Italy. *Marine and Petroleum Geology* 27, 822–837. <http://dx.doi.org/10.1016/j.marpetgeo.2009.10.016>

Balsamo, F., Storti, F., Grocke., D. R., 2012. Fault-related fluid flow history in shallow marine sediments from carbonate concretions, Croton basin, south Italy. *Journal of the Geological Society, London* 169, 613–626. <http://dx.doi.org/10.1144/0016-76492011-109>.

Balsamo, F., Clemenzi, L., Storti, F., Solum, J., Taberner, C., 2019. Tectonic control on vein attributes and deformation intensity in fault damage zones affecting Natih platform carbonates, Jabal Qusaybah, North Oman. *Journal of Structural Geology* 122, 38–57. <https://doi.org/10.1016/j.jsg.2019.02.009>.



- Barão, L. M., Trzaskos, B., Angulo, R. J., Souza, M. C., Daufenbach, H. F., Santos, F. A., Vasconcellos, E. M. G., 2020. Deformational structures developed in volcanic sequences as a product of tectonic adjustments in the South Atlantic Ocean. *Journal of South American* 104, 102812. <https://doi.org/10.1016/j.jsames.2020.102812>.
- Berg, S. S., Skar, T., 2005. Controls on damage zone asymmetry of a normal fault zone: outcrop analyses of a segment of the Moab fault, SE Utah. *Journal of Structural Geology* 27, 1803–1822. <http://dx.doi.org/10.1016/j.jsg.2005.04.012>.
- Bistacchi, A., Mittempergher, S., Martinelli, M., Storti, F., 2020. On a new robust workflow for the statistical and spatial analysis of fracture data collected with scanlines (or the importance of stationarity). *Solid Earth*, 2535–2547. <https://doi.org/10.5194/se-11-2535-2020>.
- Botter, C., Cardozo, N., Lecomte, I., Rotevatn, A., Paton, G., 2016. The impact of faults and fluid flow on seismic images of a relay ramp over production time. *Petroleum Geoscience* 23, 17–28. <https://doi.org/10.1144/petgeo2016-027>.
- Botter, C., Cardozo, N., Qu, D., Tveranger, J., Kolyukhin, D., 2017. Seismic characterization of fault facies models. *Interpretation* 5, 1–18. <http://dx.doi.org/10.1190/INT-2016-0226.1>.
- Botter, C., Champion, A., 2019. Seismic Fault Damage Zone Characterisation for Reservoir Modelling Using Advanced Attribute Analysis. Fifth International Conference on Fault and Top Seals, Palermo, Italy. <https://doi.org/10.3997/2214-4609.201902317>.
- Botter, C., Champion, A., 2019. Seismic Fault Damage Zone Characterisation for Reservoir Modelling Using Advanced Attribute Analysis. Fifth International Conference on Fault and Top Seals, Palermo, Italy. <https://doi.org/10.3997/2214-4609.201902317>.
- Braathen, A., Tveranger, J., Fossen, H., Skar, T., Cardozo, N., Semshaug, S.E., Bastesen, E., Sverdrup, E., 2009. Fault facies and its application to sandstone reservoirs. *AAPG Bulletin* 93, 891–917. <http://dx.doi.org/10.1306/03230908116>.
- Brito Neves, B. B., Santos, E. J., & Van Schmus, W. R., 2000. Tectonic history of the Borborema Province, Northeast Brazil. U.G. In Cordani, A. Thomaz Filho, & D. A. Campos (Eds.), *Tectonic Evolution of South America*. Rio de Janeiro, 31STIGC, 151–182

- Caine, J. S., Evans, J. P., Forster, C. B., 1996. Fault zone architecture and permeability structure. *Geology* 24, 1025–1028. [https://doi.org/10.1130/0091-7613\(1996\)024<1025:FZAAPS>2.3.CO;2](https://doi.org/10.1130/0091-7613(1996)024<1025:FZAAPS>2.3.CO;2).
- Cardwell, W. T., Parsons, R. I., 1945. Average permeability of heterogeneous sands. *Transactions of the American Institute of Mining Engineers* 160, 34–42.
- Carvalho, I. S., Mendes, J. C., Costa, T., 2013. The role of fracturing and mineralogical alteration of basement gneiss in the oil exudation in the Sousa Basin (Lower Cretaceous), Northeastern Brazil. *Journal of South American Earth Sciences* 47, 47–54. <https://doi.org/10.1016/j.jsames.2013.06.001>.
- Cavailhes, T., Rotevatn, A., 2018. Deformation bands in volcanoclastic rocks – Insights from the Shihtiping tuffs, Coastal Range of Taiwan. *Journal of Structural Geology* 113, 155–175. <https://doi.org/10.1016/j.jsg.2018.06.004>.
- Celestino, M. A. L., Miranda, T. S., Mariano, G., Lima, M. A., Carvalho, B. R. B. M., Falcão, T. C., Topan, J. G., Barbosa, J. A., Gomes, I. F., 2020. Fault damage zones width: Implications for the tectonic evolution of the northern border of the Araripe Basin, Brazil, NE Brazil. *Journal of Structural Geology* 138, 104116. <https://doi.org/10.1016/j.jsg.2020.104116>.
- Chesnaux, R., Allen, D. M., Jenni, S., 2009. Regional fracture network permeability using outcrop scale measurements. *Engineering Geology* 108 (2009), 259–271. <https://doi.org/10.1016/j.enggeo.2009.06.024>.
- Childs, C., Manzocchi, T., Walsh, J. J., Bonson, C. G., Nicol, A., Schöpfer, M. P. J., 2009. A geometric model of fault zone and fault rock thickness variations. *Journal of Structural Geology* 31, 117–127. <https://doi.org/10.1016/j.jsg.2008.08.009>.
- Choi, J. H., Edwards, P., Ko, K., Kim, Y. S., 2016. Definition and classification of fault damage zones: A review and a new methodological approach. *Earth-Science Reviews* 152, 70–87. <http://dx.doi.org/10.1016/j.earscirev.2015.11.006>.
- Clark, R.M., Cox, S.J., 1996. A modern regression approach to determining fault displacement–length scaling relationships. *Journal of Structural Geology* 18 (2/3), 147–152. [https://doi.org/10.1016/S0191-8141\(96\)80040-X](https://doi.org/10.1016/S0191-8141(96)80040-X).

- de Castro, D. L., Oliveira, D. C., Castelo Branco, R. M. G., 2007. On the tectonics of the Neocomian Rio do Peixe rift basin, NE Brazil: lessons from gravity, magnetic and radiometric data. *Journal of South American Earth Sciences* 24, 184–202. <https://doi.org/10.1016/j.jsames.2007.04.001>.
- de Souza, D.H.S., Nogueira, F.C.C., Vasconcelos, D.L., Torabi, A., Souza, J.A.B., Nicchio, M.A., Pérez, Y.A.R., Balsamo, F., 2021. Growth of cataclastic bands into a fault zone: a multiscale process by microcrack coalescence in sandstones of Rio do Peixe Basin, NE Brazil. *J. Struct. Geol.* 146, 104315. <https://doi.org/10.1016/j.jsg.2021.104315>.
- Debenham, N., Farrell, N. J. C., Holford, S. P., King, R. C., Healy, D., 2019. Spatial distribution of micrometre-scale porosity and permeability across the damage zone of a reverse-reactivated normal fault in a tight sandstone: Insights from the Otway Basin, SE Australia. *Basin Research* 31, 640–658. <https://doi.org/10.1111/bre.12345>.
- Del Sole, L., Antonellini, M., Calafato, A., 2020. Characterization of sub-seismic resolution structural diagenetic heterogeneities in porous sandstones: Combining ground-penetrating radar profiles with geomechanical and petrophysical in situ measurements (Northern Apennines, Italy). *Marine and Petroleum Geology* 117, 104375. <https://doi.org/10.1016/j.marpetgeo.2020.104375>.
- Evans, J.P., 1990. Thickness–displacement relationships for fault zones. *Journal of Structural Geology* 12, 1061–1065. [https://doi.org/10.1016/0191-8141\(88\)90020-X](https://doi.org/10.1016/0191-8141(88)90020-X).
- Fachri, M., Tveranger, J., Cardozo, N., Pettersen, O., 2011. The impact of fault envelop structure on fluid flow: A screening study using fault facies. *AAPG Bulletin* 95, 619–648. <http://dx.doi.org/10.1306/09131009132>.
- Fachri, M., Tveranger, J., Braathen, A., Schueller, S., 2013a. Sensitivity of fluid flow to deformation-band damage zone heterogeneities: A study using fault facies and truncated Gaussian simulation. *Journal of Structural Geology* 52, 60–79. <http://dx.doi.org/10.1016/j.jsg.2013.04.005>.
- Fachri, M., Rotevatn, A., Tveranger, J., 2013b. Fluid flow in relay zones revisited: Towards an improved representation of small-scale structural heterogeneities in flow models. *Marine and Petroleum Geology* 46, 144–164. <http://dx.doi.org/10.1016/j.marpetgeo.2013.05.016>.

- Fachri, M., Tveranger, J., Braathen, A., Roe, P., 2016. Volumetric faults in field-sized reservoir simulation models: A first case study. *AAPG Bulletin* 100, 795–817. <http://dx.doi.org/10.1306/02011614118>.
- Farrel, N. J. C., Healy, D., Taylor, C. W., 2014. Anisotropy of permeability in faulted porous sandstones. *Journal of Structural Geology* 63, 50–67. <http://dx.doi.org/10.1016/j.jsg.2014.02.008>.
- Faulkner, D. R., Jackson, C. A. L., Lunn, R. J., Schlische, R. W., Shipton, Z. K., Wibberley, C. A. J., Withjack, M. O., 2010. A review of recent developments concerning the structure, mechanics and fluid flow properties of fault zones. *Journal of Structural Geology* 32, 1557–1575. <https://doi.org/10.1016/j.jsg.2010.06.009>.
- Fossen, H., Schultz, R. A., Shipton, Z. K., Karen, M., 2007. Deformation bands in sandstone: a review. *Journal of Geological Society (London)* 164, 755–769. <https://doi.org/10.1144/0016-76492006-036>.
- Fossen, H., Soliva, R., Ballas, G., Trzaskos, B., Cavalcante, C., Schultz, R. A., 2017. A review of deformation bands in reservoir sandstones: geometries, mechanisms and distribution. *Journal of Geological Society (London)* 459, 9–33. <https://doi.org/10.1144/SP459.4>.
- Françolin, J. B. L., Cobbold, P. R., Szatmari, P., 1994. Faulting in the Early Cretaceous Rio do Peixe basin (NE Brazil) and its significance for the opening of the Atlantic. *Journal of Structural Geology* 16, 647–661. [https://doi.org/10.1016/0191-8141\(94\)90116-3](https://doi.org/10.1016/0191-8141(94)90116-3)
- Harding, A., Strebelle, S., Levy, M., Thorne, J., Xie, D., Leigh, S., Preece, R., 2005. Reservoir Facies Modelling: New Advances in MPS. In: Leuang Thong O., Deutsch C.V. (eds) *Geostatistics Banff 2004. Quantitative Geology and Geostatistics*, 14. Springer, Dordrecht. [https://doi.org/10.1007/978-1-4020-3610-1\\_57](https://doi.org/10.1007/978-1-4020-3610-1_57)
- Iacopini, D. Butler, R.W.H., Purves, S., McArdle, N., De Freslon, N., 2016. Exploring the seismic expression of fault zones in 3D seismic volumes. *Journal of Structural Geology* 89, 54–73. <http://dx.doi.org/10.1016/j.jsg.2016.05.005>
- Jackson, C. A. L., and A. Rotevatn, 2013, 3D seismic analysis of the structure and evolution of a salt-influenced normal fault zone: A test of competing fault growth models: *Journal of Structural Geology* 54, 215–234, <https://doi.org/10.1016/j.jsg.2013.06.012>.

- Liao, Z., Chen, W., Chen, X., Zhou, Y., Hao, F., 2020a. Multiscale fracture and damage zone characterization in a tight sandstone reservoir, Sichuan Basin, China. *Interpretation* 8, 1–11. <http://dx.doi.org/10.1190/INT-2019-0107.1>.
- Liao, Z., Hu, L., Huang, X., Carpenter, B. M., Marfurt, K. J., Vasileva, S., Zhou, Y., 2020b. Characterizing damage zones of normal faults using seismic variance in the Wangxuzhuang oilfield, China. *Interpretation* 8, 1–8. <http://dx.doi.org/10.1190/INT-2020-0004.1>.
- Ma, D. B., Wu, G. H., Scarselli, N., Luo, X. S., Han, J. F., Chen, Z. Y., 2019. Seismic damage zone and width-throw scaling along the strike-slip faults in the Ordovician carbonates in the Tarim Basin. *Petroleum Science* 16, 752–762. <https://doi.org/10.1007/s12182-019-0352-4>.
- Maciel, I. B., Dettori, A., Balsamo, F., Bezerra, F. H. R., Vieira, M. M., Nogueira, F. C. C., Salvioli-Mariani, E., Sousa, J. A. B., 2018. Structural Control on Clay Mineral Authigenesis in Faulted Arkosic Sandstone of the Rio do Peixe Basin, Brazil. *Minerals* 8, 1–17. <https://doi.org/10.3390/min8090408>.
- Maerten, L., Gillespie, P., Daniel, J. M., 2006. Three-dimensional geomechanical modelling for constraint of subseismic fault simulation. *AAPG Bulletin* 90, 1337–1358. <https://doi.org/10.1306/03130605148>.
- Manzocchi, T., Walsh, J. J., Nell, P., Yielding, G., 1999. Fault transmissibility multipliers for flow simulation models. *Petroleum Geoscience* 5, 53–63. <https://doi.org/10.1144/petgeo.5.1.53>.
- Martinelli, M., Bistacchi, A., Mittempergher, S., Bonneau, F., Balsamo, F., Caumon, G., Meda, M., 2020. Damage zone characterization combining scan-line and scan-area analysis on a km-scale Digital Outcrop Model: The Qala Fault (Gozo). *Journal of Structural Geology* 140, 104144. <https://doi.org/10.1016/j.jsg.2020.104144>.
- Matos, R. M. D., 1992. The northeastern Brazilian Rift System. *Tectonics* 11, 766–791. <https://doi.org/10.1029/91TC03092>.
- Medeiros, V. C., Amaral, C. A., Rocha, D. E. G. A., Santos, R. B., 2005. Programa Geologia 800 do Brasil - PGB. Sousa. Folha SB.24-Z-A. Estados da Paraíba, Rio Grande do Norte e Ceará. Mapa Geológico. Recife: CPRM, 2005, 1 mapa, color., 66cm x 108cm. Escala 1:250.000.

- Medeiros, W.E., do Nascimento, A.F., Silva, F.C. A., Destro, N., Demétrio, J.G.A., 2010. Evidence of hydraulic connectivity across deformation bands from field pumping tests: Two examples from Tucano Basin, NE Brazil. *Journal of Structural Geology* 32, 1783-1791. <https://doi.org/10.1016/j.jsg.2009.08.019>
- Micarelli, L., Moretti, I., Daniel, J. M., 2003. Structural properties of rift-related normal faults: the case study of the Gulf of Corinth, Greece. *Journal of Geodynamics* 36, 275–303. [https://doi.org/10.1016/S0264-3707\(03\)00051-6](https://doi.org/10.1016/S0264-3707(03)00051-6).
- Nicchio, M. A., Nogueira, F. C. C., Balsamo, F., Souza, J. A. B., Carvalho, B. R. B. M., Bezerra, F. H. R., 2017. Development of cataclastic foliation in deformation bands in feldspar-rich conglomerates of the Rio do Peixe Basin, NE Brazil. *Journal of Structural Geology* 107, 132–141. <https://doi.org/10.1016/j.jsg.2017.12.013>.
- Nogueira, F. C. C., Marques, F. O., Bezerra, F. H. R., Fuck, R., 2015. Cretaceous intracontinental rifting and post-rift inversion in NE Brazil: Insights from the Rio do Peixe Basin. *Tectonophysics* 644-645, 92–107. <http://dx.doi.org/10.1016/j.tecto.2014.12.016>
- Nogueira, F. C. C., Nicchio, M. A., Balsamo, F., Souza, J. A. B., Silva, I. V. L., Bezerra, F. H. R., Vasconcelos, D. L., Carvalho, B. R. B. M., 2021. The influence of the cataclastic matrix on the petrophysical properties of deformation bands in arkosic sandstones. *Marine and Petroleum Geology* 134, 104825. <https://doi.org/10.1016/j.marpetgeo.2020.104825>.
- Odling, N.E., Harris, S.D., Knipe, R.J., 2004. Permeability scaling properties of fault damage zones in siliclastic rocks. *Journal of structural Geology* 26, 1727–1747. <http://dx.doi.org/10.1016/j.jsg.2004.02.005>.
- Oliveira, L.S.B., Nogueira, F.C.C., Vasconcelos, D.L., Balsamo, F., Bezerra, F.H.R., Perez, Y.A.R., 2022. Mechanical stratigraphy influences deformation band pattern in arkosic sandstones, Rio do Peixe Basin, Brazil. *Journal of Structural Geology* 155, 104510. <https://doi.org/10.1016/j.jsg.2022.104510>.
- Pizzati, M., Balsamo, F., Storti, F., 2020. Displacement-dependent microstructural and petrophysical properties of deformation bands and gouges in poorly lithified sandstone deformed at shallow burial depth (Crotone Basin, Italy). *Journal of Structural Geology* 137, 104069. <https://doi.org/10.1016/j.jsg.2020.104069>.

- Pontes, C. C. C., Nogueira, F. C. C., Bezerra, F. H. R., Balsamo, F., Miranda, T.S., Nicchio, M. A., Souza, J. A. B., Carvalho, B. R. B. M., 2019. Petrophysical properties of deformation bands in high porous sandstones across fault zones in the Rio do Peixe Basin, Brazil. *International Journal of Rock Mechanics and Mining Sciences* 114, 153–163. <https://doi.org/10.1016/j.ijrmms.2018.12.009>.
- Pyrzcz, M. J., Catuneanu, O., Deutsch, C. V., 2005. Stochastic surface-based modeling of turbidite lobes. *AAPG Bulletin* 89, 177–191. <https://doi.org/10.1306/09220403112>.
- Qu, D., Røe, P., Tveranger, J., 2015. A method for generating volumetric fault zone grids for pillar gridded reservoir models. *Computers & Geosciences* 81, 28–37. <http://dx.doi.org/10.1016/j.cageo.2015.04.009>.
- Qu, D., Tveranger, J., 2016. Incorporation of deformation band fault damage zones in reservoir models. *AAPG Bulletin* 100, 423–443. <https://doi.org/10.1306/12111514166>
- Qu, D., Tveranger, J., Fachri, M., 2017. Influence of deformation-band fault damage zone on reservoir performance. *Interpretation* 5, 41–56. <http://dx.doi.org/10.1190/INT-2016-0229>.
- Ramos, G.V., Vasconcelos, D.L., Marques, F.O., de Castro D. L., Nogueira, F.C.C., Bezerra, F.H.B., Perez, Y.A.R., Souza, J.A.B., Medeiros, V.C., 2022. Relations between inherited basement fabric and fault nucleation in a continental setting: The Rio do Peixe Basin, NE Brazil. *Marine and Petroleum Geology* 139, 105635. <https://doi.org/10.1016/j.marpetgeo.2022.105635>.
- Rapozo, B. F., Córdoba, V.C., Antunes, A.F., 2021. Tectono-stratigraphic evolution of a cretaceous intracontinental rift: Example from Rio do Peixe Basin, north-eastern Brazil. *Marine and Petroleum Geology* 126, 104899. <https://doi.org/10.1016/j.marpetgeo.2021.104899>.
- Romano, C. R., Zahasky, C., Garing, C., Minto, J. M., Benson, S. M., Shipton, Z. K., Lunn, R. J., 2020. Subcore Scale Fluid Flow Behavior in a Sandstone With Cataclastic Deformation Bands. *Water Resources Research American Geophysical Union (AGU)* 56, 10–20. <http://dx.doi.org/10.1029/2019wr026715>.
- Rotevatn, A., Tveranger, J., Howell, J. A., Fossen, H., 2009. Dynamic investigation of the effect of a relay ramp on simulated fluid flow: geocellular modelling of the Delicate Arch Ramp, Utah. *Petroleum Geoscience* 15, 45–58. <https://doi.org/10.1144/1354-079309-779>.

- Rotevatn, A., Fossen, H., 2011. Simulating the effect of subseismic fault tails and process zones in a siliciclastic reservoir analog: Implications for aquifer support and trap definition. *Marine and Petroleum Geology* 28, 1648–1662. <https://doi.org/10.1016/j.marpetgeo.2011.07.005>.
- Rotevatn, A., Thorsheim, E., Bastesen, E., Fossmark, H. S. S., Torabi, A., Saelen, G., 2016. Sequential growth of deformation bands in carbonate grainstones in the hangingwall of an active growth fault: Implications for deformation mechanisms in different tectonic regimes. *Journal of Structural Geology* 90, 27–47. <https://doi.org/10.1016/j.jsg.2016.07.003>.
- Schueller, S., Braathen, A., Fossen, H., Tveranger, J., 2013. Spatial distribution of deformation bands in damage zones of extensional faults in porous sandstones: Statistical analysis of field data. *Journal of Structural Geology* 52, 148–162. <http://dx.doi.org/10.1016/j.jsg.2013.03.013>.
- Schultz, R.A., Siddharthan, R., 2005. A general framework for the occurrence and faulting of deformation bands in porous granular rocks. *Tectonophysics* 411, 1–18. <https://doi.org/10.1016/j.tecto.2005.07.008>.
- Sénant, J., Popoff, M., 1991. Early Cretaceous extension in northeast Brazil related to the South Atlantic opening. *Tectonophysics* 198, 35–46. [https://doi.org/10.1016/0040-1951\(91\)90129-G](https://doi.org/10.1016/0040-1951(91)90129-G).
- Shipton, Z.K., Evans, J. P., Robeson, K. R., Forster, C. B., Snelgrove, S., 2002. Structural heterogeneity and permeability in faulted eolian sandstone: Implications for subsurface modeling of faults. *AAPG Bulletin* 86, 863–883
- Shipton, Z. K., Evans, J. P., Thompson, L.B., 2005. The Geometry and Thickness of Deformation-band Fault Core and its Influence on Sealing Characteristics of Deformation-band Fault Zones. *AAPG Memoir* 85, 181–195. <https://doi.org/10.1306/1033723M853135>.
- Shipton, Z. K., Soden, A. M., Kirkpatrick, J. D., Bright, A. M., Lunn, R. J., 2006. How thick is a fault? Fault displacement-thickness scaling revisited. In Abercrombie, R. (Eds) *Earthquakes: Radiated Energy and the Physics of Faulting*, 193-198.
- Silva, J.G.F., 2014. Análise estratigráfica de subsuperfície do Devoniano Inferior da Bacia do Rio do Peixe, Nordeste do Brasil. Msc. Dissertation. Universidade Federal do Rio Grande do Norte, Natal, 1–189.



- Silva, J. G. F., Córdoba, V. C., Caldas, L. H. C., 2014. Proposta de novas unidades litoestratigráficas para o Devoniano da Bacia do Rio do Peixe, Nordeste do Brasil. *Brazilian Journal of Geology* 44, 561–578. <https://doi.org/10.5327/Z23174889201400040004>.
- Silva, M.E., Nogueira, F.C.C., Perez, Y.A.R., Vasconcelos D.L., Stohler R.C., Sanglard J.C.D., Balsamo, F., Bezerra, F.H.R., Carvalho, B.R.B.M., Souza, J.A.B., 2022. Permeability modeling of a basin-bounding fault damage zone in the Rio do Peixe Basin, Brazil. *Marine and Petroleum Geology* 135, 105409. <https://doi.org/10.1016/j.marpetgeo.2021.105409>.
- Soliva, R., Ballas, G., Fossen, H., Philip, S., 2016. Tectonic regime controls clustering of deformation bands in porous sandstone. *Geology* 44, 423–426. <https://doi.org/10.1130/G37585.1>.
- Sorkhabi, R., Hasegawa, S., 2005. Fault Zone Architecture and Permeability Distribution in the Neogene Clastics of Northern Sarawak (Miri Airport Road Outcrop), Malaysia. *AAPG Memoir* 85, 139–151. <https://doi.org/10.1306/1033721M853128>.
- Syversveen, A. R., Skorstad, A., Soleng, H. H., Røe, P., Tveranger, J., 2006. Facies modelling in fault zones. *Proceedings of the 10th European Conference on the Mathematics of Oil Recovery*.
- Tondi, E., Antonellini, M., Aydin, A., Marchegiani, L., Cello, G., 2006. The role of deformation bands, stylolites and sheared stylolites in fault development in carbonate grainstones of Majella Mountain, Italy. *Journal of Structural Geology* 28 (3), 376–391. <https://doi.org/10.1016/j.jsg.2005.12.001>.
- Torabi, A., Fossen, H., 2009. Spatial variation of microstructure and petrophysical properties along deformation bands in reservoir sandstones. *AAPG Bulletin* 93, 919–938. <https://doi.org/10.1306/03270908161>.
- Torabi, A., Berg, S. S., 2011. Scaling of fault attributes: A review. *Marine and Petroleum Geology* 28, 1444–1460. <https://doi.org/10.1016/j.marpetgeo.2011.04.003>.
- Torabi, A., Fossen, H., Braathen, A., 2013. Insight into petrophysical properties of deformed sandstone reservoirs. *AAPG Bulletin* 97, 619–637. <https://doi.org/10.1306/10031212040>.
- Torabi, A., Gabrielsen, R. H., Fossen, H., Ringrose, P., Skurtveit, E., Ando, E., Marinelli, F., Viggiani, G., Dal Point, S., Braathen, A., Hovland, A., Bésuelle, P., Alikarami, R., Zalmstra, PPGEPM – UFCG

- H., Sokoutis, D., 2015. Strain localization in sandstone and its implications for CO<sub>2</sub> storage. *First break* 33, 81–92.
- Torabi, A., Johannessen, M. U., Ellingsen, T. S. S., 2019. Fault core Thickness: Insights from siliciclastic and Carbonate Rocks. *Geofluids* 2019, 1–24. <https://doi.org/10.1155/2019/2918673>.
- Torabi, A., Ellingsen, T. S. S., Johannessen, M. U., Alaei, B., Rotevatn, A., Chiarella, D., 2020. Fault zone architecture and its scaling laws: where does the damage zone start and stop? *Geological Society, London, Special Publications*, 496, 99–124. <https://doi.org/10.1144/SP496-2018-151>.
- Torabi, A., Balsamo, F., Nogueira, F.C.C., Vasconcelos, D.L., Silva, A.E., Bezerra, F.H.R., Souza, J.A.B., 2021. Variation of thickness, internal structure and petrophysical properties in a deformation band fault zone in siliciclastic rocks. *Marine and Petroleum Geology* 133, 105409. <https://doi.org/10.1016/j.marpetgeo.2021.105409>.
- Tveranger, J., Braathen, A., Skar, T., 2004. Incorporation of fault zones as volumes in reservoir models. *Bolletino di Geofisica Teoretica et Applicata* 45, 316–318.
- Tveranger, J., Braathen, A., Skar, T., Skauge, A., 2005. Centre for Integrated Petroleum Research: Research activities with emphasis on fluid flow in fault zones. *Norwegian Journal of Geology* 85, 179–187.
- Vasconcelos, D., Marques, F. O., Nogueira, F. C. C., Perez, Y. A. R., Bezerra, F. H. R., Stohler, R. C., Souza, J. A. B., 2021. Tectonic inversion assessed by integration of geological and geophysical data: The intracontinental Rio do Peixe Basin, NE Brazil. *Basin Research* 2020, 1–24. <https://doi.org/10.1111/bre.12491>.
- Wibberley, C. A. J., Pettit, J. P., Rives, T., 2007. The mechanics of fault distribution and localization in high-porosity sands, Provence, France. *Geological Society, London, Special Publications* 289, 19–46. <https://doi.org/10.1144/SP289.3>.
- Wilson, P.I.R., Wilson, R.W., Sanderson, D.J., Jarvis, I., McCaffrey, K.J.W., 2021. Analysis of deformation bands associated with the Trachyte Mesa intrusion, Henry Mountains, Utah: implications for reservoir connectivity and fluid flow around sill intrusions. *Solid Earth* 12, 95–117. <https://doi.org/10.5194/se-12-95-2021>.